

UC Berkeley

UC Berkeley Electronic Theses and Dissertations

Title

Electrical and Optical Enhancement in Internally Nanopatterned Organic Light-Emitting Diodes

Permalink

<https://escholarship.org/uc/item/19f58436>

Author

Fina, Michael Dane

Publication Date

2012

Peer reviewed|Thesis/dissertation

Electrical and Optical Enhancement in
Internally Nanopatterned Organic Light-Emitting Diodes

By

Michael Dane Fina

A dissertation submitted in partial satisfaction of the

requirements for the degree of

Doctor of Philosophy

in

Engineering-Mechanical Engineering

in the

Graduate Division

of the

University of California, Berkeley

Committee in charge:

Professor Samuel Mao, Co-Chair

Professor Ralph Greif, Co-Chair

Professor Costas Grigoropoulos

Professor Vivek Subramanian

Fall 2012

Electrical and Optical Enhancement in
Internally Nanopatterned Organic Light-Emitting Diodes

© 2012

by Michael Dane Fina

Abstract

Electrical and Optical Enhancement in Internally Nanopatterned Organic Light-Emitting Diodes

by

Michael Dane Fina

Doctor of Philosophy in Engineering-Mechanical Engineering

University of California, Berkeley

Professor Samuel Mao, Co-Chair

Professor Ralph Greif, Co-Chair

Organic light-emitting diodes (OLEDs) have made tremendous technological progress in the past two decades and have emerged as a top competitor for next generation light-emitting displays and lighting. State-of-the-art OLEDs have been reported in literature to approach, and even surpass, white fluorescent tube efficiency. However, despite rapid technological progress, efficiency metrics must be improved to compete with traditional inorganic light-emitting diode (LED) technology. Organic materials possess specialized traits that permit manipulations to the light-emitting cavity. Overall, as demonstrated within, these modifications can be used to improve electrical and optical device efficiencies. *This work is focused at analyzing the effects that nanopatterned geometric modifications to the organic active layers play on device efficiency.*

In general, OLED efficiency is complicated by the complex, coupled processes which contribute to spontaneous dipole emission. A composite of three sub-systems (electrical, exciton and optical) ultimately dictate the OLED device efficiency. OLED electrical operation is believed to take place via a low-mobility-modified Schottky injection process. In the injection-limited regime, geometric effects are expected to modify the local electric field leading to device current enhancement. It is shown that the patterning effect can be used to enhance charge carrier parity, thereby enhancing overall recombination. Current density and luminance characteristics are shown to be improved by OLED nanopatterning from both the model developed within and experimental techniques.

Next, the optical enhancement effects produced by the nanopatterned array are considered. Finite-difference time-domain (FDTD) simulations are used to determine positional, spectral optical enhancement for the nanopatterned device. The results show beneficial effects to the device performance. The optical enhancements are related to the reduction in internal radiative quenching (improved internal quantum efficiency) and improvement in light extraction (improved outcoupling efficiency). Furthermore, the electrical model is used to construct a positional radiative efficiency map that when combined with the optical enhancement reveals the overall external quantum efficiency enhancement.

Dedication

To Mom and Dad – for your inspiration and support, and a fond childhood

To Nick – my brother and best friend

Table of Contents

Chapter 1. Introduction	1
1.1 Introduction to OLED technology	1
1.2 Historical Developments in Organic Electroluminescence	1
1.3 OLED applications	3
1.3.1 Solid-State Lighting.....	5
1.3.2 Microelectronic Displays	5
1.4 Scope of work – Efficiency influences of patterning OLEDs	6
1.4.1 Electrical enhancement from nanopatterned organic layer.....	7
1.4.2 Optical enhancement from nanopatterned organic layer	7
1.5 Dissertation outline.....	8
Chapter 2. Organic Electronic Materials	9
2.1 Introduction	9
2.2 Classifications of organic materials.....	9
2.3 Molecular bonding.....	10
2.4 Morphology.....	11
2.5 Processing	12
2.6 Localization effects	13
2.7 Mobility	13
2.8 Band or Hopping transport?	14
2.9 Excitons: Energy Transfer and Optoelectronic Processes	15
2.10 Conclusion.....	17
Chapter 3. Theory of OLED Electrical Operation	18
3.1 Introduction	18
3.2 Charge Transport Models	19
3.2.1 Monte Carlo Simulation	19
3.2.2 Semiconductor Equations	20
3.2.3 Master Equation	23
3.3 Carrier Injection Mechanism	25
3.3.1 Barrier Formation	25
3.3.1.1 Interfacial dipole	26
3.3.1.2 Image potential.....	28
3.3.2 Thermionic Injection.....	28
3.3.2.1 Richardson theory.....	28

3.3.2.2	Schottky theory	29
3.3.2.3	Los Alamos Group Model	31
3.3.2.4	Scott-Malliaras theory	31
3.3.3	Tunneling injection	33
3.3.4	Interface broadening model	34
3.4	Current Limiting Cases	34
3.4.1	Bulk Limit Regime	36
3.4.1.1	Ohmic Regime	36
3.4.1.2	Space-Charge Limit	37
3.4.1.3	Trap-Charge Limit	38
3.4.1.4	Trap-Free Space-Charge Limit	39
3.4.2	Injection Limit	40
3.5	Conclusion	41

Chapter 4. Analysis of one-dimensional space-charge-limited effects in a single-layer organic light-emitting diode **42**

4.1	Introduction	42
4.2	One-dimensional numerical solution	42
4.2.1	Solution procedure	44
4.2.2	Finite Difference Formulation	46
4.2.3	Potential System Numerics	47
4.2.4	Carrier Concentration System Numerics	48
4.2.4.1	Spatial discretization – Scharfetter-Gummel	48
4.2.4.2	Temporal discretization – Backward Euler	49
4.2.4.3	Non-linear solution techniques	49
4.2.4.4	Computing the Numerical Solution	50
4.3	NPB device numerical solution	50
4.4	IL/SCL cross-over for SM model	52
4.5	Conclusion	52

Chapter 5. Approximating the Electrical Enhancement Effects in a Nanopatterned, Injection-Limited, Single-Layer Organic Light-Emitting Diode **53**

5.1	Introduction	53
5.2	Background	53
5.3	SLOLED Current Theory	54
5.3.1	SLOLED current analysis	54
5.3.2	OLED current models	59

5.3.3	Requirements for injection limited treatment.....	60
5.3.4	Poisson Equation under injection limited conditions	61
5.3.5	Carrier-decoupled injection mechanism.....	63
5.3.6	Drift-diffusion equations.....	64
5.3.7	Determination of electric field streamlines	64
5.3.8	Cross-streamline diffusion analysis.....	65
5.3.9	Formulation of streamline analysis.....	66
5.4	Results and Discussion	69
5.4.1	Injection current enhancement	69
5.4.2	Total current enhancement	70
5.4.3	Current injection balance	71
5.4.4	Carrier confinement	74
5.4.5	Recombination efficiency.....	75
5.4.6	Influence of effective thickness reduction.....	76
5.5	Comparison with experiments.....	77
5.6	Geometrically-optimized enhancement from model.....	78
5.7	Conclusions	84

Chapter 6. Analysis of the Emission Enhancement Effects in a Nanopatterned, Single-Layer Organic Light-Emitting Diode **85**

6.1	Introduction	85
6.2	Device Emission Metrics	85
6.2.1	Internal Quantum Efficiency	86
6.2.2	Classical Light Extraction Efficiency.....	88
6.3	Maxwell Equations.....	89
6.4	FDTD Simulation Setup	91
6.5	FDTD Results	94
6.5.1	Planar OLED	94
6.5.2	Dipole Emission Enhancement from Nanopatterning	96
6.5.3	Recombination-Weighted External Quantum Efficiency Enhancement.....	100
6.5.3.1	Recombination rate weighting from electrical model.....	100
6.5.3.2	Optical Enhancement.....	102
6.6	Conclusions	108

Chapter 7. Conclusions and Future Work **109**

7.1	Conclusions	109
7.2	Future Work.....	109

References	110
Appendix A. Metal-Organic Injection Equations	117
A.1. Richardson-Schottky Theory	117
A.2. Simmons Theory	117
A.3. Emtage-O’Dwyer Theory.....	118
A.4. Scott-Malliaras Theory.....	118
Appendix B. Semiconductor Equations - Numerical Solution	120
B.1. Decoupled Quasi-linear Poisson	120
B.2. Continuity equations.....	124
B.2.1. Decoupled Drift-Diffusion Equations	125
B.2.2. Boundary conditions on electron system	127
Appendix C. Experimental Setup	128
C.1. Mechanical System	128
C.2. Device Fabrication Procedure.....	130
C.2.1. Pattern Process Layout.....	130
C.2.2. Patterning ITO	131
C.2.3. Cleaning Substrates	132
C.2.4. Patterning Aluminum	132
C.3. Thermal Evaporation Deposition	132
C.4. Device Characterization	133

List of Figures

- Figure 1.1: Landmark organic light-emitting devices. At left, the first highly-efficient small molecule organic light-emitting diode. This device utilized an organic bilayer to confine charges at the heterojunction [25]. More recent devices use NPB or TPD diamine molecules. At right, the first solution-processed polymer light-emitting diode [26]...... 3
- Figure 1.2: Commercialized OLED devices: OLED TVs, (A) Sony XEL-1 and (B) LG 15EL9500; AMOLED mobile phones, (C) Samsung Galaxy S and (D) Google Nexus One; digital camera, Kodak LS633; car stereo, Pioneer DEH-9200R. 6
- Figure 1.3: An example colormap demonstrating the electric field enhancement occurring from device structural modification. This example is explained in more detail in Chapter 5..... 7
- Figure 1.4: An illustration showing the power extraction modification resulting from internally patterned cathode interface. This example is explained in more detail in Chapter 6..... 8
- Figure 2.1: Prototypical organic light-emitting materials. At left, anthracene, a crystalline organic material used in early literature; at middle, poly(p-phenylene vinylene) (PPV), a conducting polymer used in early polymer light-emitting diodes; at right, tris(8-hydroxyquinoline)aluminum (Alq₃), a small molecule organic used in early small molecule OLEDs. 9
- Figure 2.2: Comparison of bonding in inorganic and organic materials. At left, Si is tetrahedrally bound (picture above is a 2-d planar simplification to 3-d structure) to three adjacent Si atoms; at right, anthracene bonding includes intra-molecular covalent bonding and inter-molecular dipole-dipole bonding. The intramolecular bonds include σ -bonds (localized) and π -bonds (delocalized, contribute to electron transport) and intermolecular bonds which are localized due to weak interaction forces. Transport of holes is analogous. 11
- Figure 2.3: Schematic of lab-grade deposition processes used in this work. At left, thermal evaporation via sublimation from crucible; at right, spin-coating deposition from solution. 13
- Figure 2.4: Band versus hopping type electron transport. Classically, in inorganic semiconductors, carrier transport occurs through extended state transport. In organic materials, carriers become localized and hopping transport results [65]. The figure shows distinction between multiple trap and release and hopping transport. 15

Figure 2.5:	Semiconductor excitonic binding types in lattice space. At left, Frenkel exciton (common in organic semiconductors). At middle, Charge Transfer exciton (common in organic semiconductors). At right, Wannier-Mott excitons (common in inorganic semiconductors). After [65,70].	16
Figure 2.6:	Exciton transfer processes. At left, Förster exciton transfer, when exciton transfer occurs via dipole-dipole resonance. This process occurs for singlet-singlet excitons. At right, Dexter transfer, short-range exciton tunneling. $M1^*$ is the excited donor molecule and $M2$ is ground state acceptor molecule. Superscript * denotes an excited state.	16
Figure 2.7:	Jablonski diagram. Showing electronic processes in organic materials related to host-guest materials. Two systems exist singlet and triplet manifolds, from [152].	17
Figure 3.1:	Energy band diagram of OLED emission mechanism under applied field. The following processes culminate in sensible light emission: (1) carrier injection; (2) carrier transport; (3) carrier accumulation at heterojunction; (4) carrier recombination / exciton formation; (5) exciton diffusion; (6) exciton radiative decay / photon internal emission; and (7) photon exiting device (external). Processes 1-4 are related to the electrical system [24,65,66,77,89]. Processes 4-6 are related to the exciton system [23,75]. Processes 6-7 are related to the photon system [31,78,79]. Acronyms used in diagram: HTL, hole transport layer; ETL, electron transport layer.	18
Figure 3.2:	Image depicting electron occupation and transport in a statistical framework. At left, electron hopping in presence of electric field. At right, energy levels within Gaussian density of states with occupied states near the electron quasi-Fermi potential level, F_n . Adapted from [67].	20
Figure 3.3:	Common injection mechanisms. Diagrams from left to right: Fermi-Dirac (F-D) distribution function describing the thermally excited electron population. Thermionic injection occurs when electrons are thermally excited over the injection barrier. Field injection occurs when charges tunnel through the injection barrier. Thermionic-field injection occurs when electrons are thermally excited but not enough to surmount the injection barrier and subsequently tunnel through a narrower tunneling barrier.	25
Figure 3.4:	Energy levels at a metal-organic semiconductor interface abiding by the Mott-Schottky limit. Energy levels: E_{vac} , vacuum level; E_{LUMO} , organic LUMO energy level; E_{HOMO} , organic HOMO energy level; E_F , metal Fermi energy level. Energy differences: Φ_{Bn} , metal-organic electron injection barrier; Φ_{Bp} , metal-organic hole injection barrier; ϕ_M , metal work function (metal-vacuum); χ , organic electron affinity (LUMO-vacuum); I_p , organic ionization potential (HOMO-vacuum); E_G , organic band gap (LUMO-HOMO).	26

Figure 3.5: Metal-organic (M-O) band diagrams for electron injection. A) Formation of an M-O barrier abiding by Mott-Schottky limit; barrier height is $\Phi_{B,MS}$. B) Formation of an M-O including an interface dipole; barrier height is $\Phi_{B,ID}$ 27

Figure 3.6: At left, an energy diagram showing the injection potential barrier formed by the image Coulombic reaction. At right, the formation of an electric dipole between an injected electron and its image at a metal-organic interface..... 28

Figure 3.7: Total potential, $V(x)$, within the semiconductor including components of Schottky barrier lowering (SBL), image force (IF) and injection barrier (Equation 3.25). Modified from [75,66,134]. 30

Figure 3.8: Progression of thermionic injection models for use in inorganic semiconductors. At left, thermionic injection from metal to vacuum (discharge tube); at middle, thermionic injection into conduction band of inorganic semiconductor (Mott-Schottky limit); at right, thermionic injection into conduction band of inorganic semiconductor including Schottky Barrier Lowering effect (dashed line). 31

Figure 3.9: Common injection interpretation for activated electrons. At left, electron (e^-) population showing fraction of activated electrons. At middle, injection into low mobility materials, interface recombination reduces aggregate number of activated electrons being injected into bulk (bulk injection). At right, nearly all activated electrons enter the bulk. Adapted from [161]. 32

Figure 3.10: Carrier injection for (A) injection-limited contact and (B) ohmic contact. In (A), the barrier height, $\Phi_{B,e}$ and produces a Schottky contact; in (B), the $\Phi_{B,e}$ is small and the large carrier injection leads to carrier accumulation which in term leads to electric field redistribution. 35

Figure 3.11: Current-Voltage (IV) relationships for single-carrier TCL and IL conditions. At left, injection limited (IL) regime. At right, trap-charge limited regime (TCL), which goes trends through the following regimes as voltage increases: ohmic, space-charge limited (SCL), trap-charge limited (TCL) and trap-free space-charge limited (TFSCl). Modified from [66]..... 36

Figure 4.1: In A), program flow diagram showing solution technique for solving the semiconductor equations. In B), the anode applied voltage (relative to ground cathode voltage) as a function of time allowing the system to periodically find a steady-state solution, which is useful for outputting intermediate data for a JV sweep. 45

Figure 4.2: Energy band diagrams of (A) common band diagram description of the energy levels in common HTL, NPB, (B) example initial condition band diagram for the NPB material SLOLED device and (C) the band diagram as the applied voltage bends the bands forcing carrier injection..... 46

Figure 4.3:	Finite difference method mesh. At left, a wire mesh divides a geometry up into discrete points. At right, the 5-point star (for 2d FD) used for basic Laplacian evaluation.	47
Figure 4.4:	Results for an example single-layer device in the injection limited (IL) regime. The device is ITO/NPB(100nm)/Al. In A, device electric field; in B, electron and hole carrier concentrations; in C, recombination rate; in D, JV curve.	51
Figure 4.5:	Results for an example single-layer device that is considered in the space-charge limited (SCL) regime according to criterion in Ref. 114. The device is ITO/PEDOT:PSS/NPB(100nm)/LiF(0.5 nm)/Al. In top left, device electric field; in top right, electron and hole carrier concentrations; in bottom left, recombination rate; in bottom right, JV curve versus Mott-Gurney SCL limit, J_{MG} (Equation 3.43).	51
Figure 4.6:	Transition from IL to SCL regime as a function of injection barrier height. The device is: ITO/MEH-PPV(120nm)/Al (same as in [114], for comparison), where the hole barrier height is varied according to the inset values. At left, JV curves compared to Mott-Gurney current. At right, the electric field profiles. Non-uniform profiles are caused by SCL effects.....	52
Figure 5.1:	Nanoimprint pressing process realizing cathode structuring.....	53
Figure 5.2:	Energy diagram with superposed current map (magnitude of arrows) indicating the expected injection and leakage currents within an SLOLED of structure: ITO/NPB/Al for a one-dimensional device. Injection currents: $I_{p,an}$ and $I_{n,cath}$; leakage currents: $I_{p,cath}$ and $I_{n,an}$	55
Figure 5.3:	(a) Current profile within an SLOLED including visual representations of carrier currents, total carrier currents, total current, recombination current and unconfined current. (b) The influence of carrier balance efficiency, η_{bal} and confinement efficiency, η_{cnf} on recombination efficiency, η_{rec} . To facilitate understanding efficiency terms, the three efficiency terms are shown as a ratio of their graphically represented current equivalents.....	58
Figure 5.4:	Minimum repetitive unit for nanocolumn array at cathode. Representation of the system of equations describing electric potential in the organic layer including domain and boundary conditions.....	61
Figure 5.5:	A map showing the electric field within the organic material after imprinting a column into the medium. In (A), electric field magnitude compared to baseline device; in (B), surface electric field enhancement along top of the imprinted column.	62

- Figure 5.6: Streamline formulation utilized throughout analysis section. l is the streamline width, E is the streamline electric field, i is the streamline index and j is a discrete element along the streamline. e is an element located in stream i and is the j^{th} element along the streamline starting at the cathode..... 65
- Figure 5.7: Average carrier current enhancement factors due to the incorporation of nanoscale column structures at the cathode interface. At top, the anode holes current enhancement factor; at bottom, the cathode electrons current enhancement factor. The inserted dots represent the optimized conditions used in forthcoming analysis. 70
- Figure 5.8: (Bottom) Colormap of streamline total current enhancement factor, $F_{I_{tot},i}(= I_{tot,i}/I_{tot,0})$. Following from the dominant hole carrier injection current and the largest electric field enhancement occurring at the left side of the anode surface, the current is improved by the largest amount in the left-most streamlines. (Top) Anode-organic interface profile of the total current enhancement factor with superposed streamline colormap. 71
- Figure 5.9: (Bottom) Colormap showing the shift in effective barrier height, $\Delta\Phi_{B,i}(= \Phi_{B,eff,cath} - \Phi_{B,eff,an})$ [eV]. The effects are most pronounced on the interior and exterior corners of the geometry, where the barrier shift leads to excess concentrations of electrons and holes along the streamline, respectively. (Top) Anode-organic interface profile of the effective barrier height shift with superposed streamline colormap. 73
- Figure 5.10: (Bottom) Colormap showing pathway current balance enhancement factor, $F_{bal,i}$. Due to the effective barrier height shift in the left-most current pathways, as seen in Figure 5.9, the improvement in electron injection leads to substantial enhancements in current injection balance. (Top) Anode-organic interface profile of the current injection balance factor with superposed streamline colormap. . 74
- Figure 5.11: (Bottom) Colormap of the streamline confinement enhancement factor, $F_{cnf,i}(= \eta_{cnf,i}/\eta_{cnf,0})$. Carrier confinement is improved in regions having low ratios of pathway current density to electric field. In such regions, where carrier velocity is slow, carriers are allowed more opportunity to find counter-carriers, thus promoting recombination. (Top) Anode-organic interface profile of the confinement enhancement factor with superposed streamline colormap. 75
- Figure 5.12: Colormap of streamline overall recombination efficiency enhancement factor, $F_{rec,i}(= \eta_{rec,i}/\eta_{rec,0})$. Recombination efficiency, as defined through Equation 5.12, is related to the product of the current balance efficiency and the confinement efficiency. Therefore, the regions demonstrating the largest enhancement in pathway recombination efficiency are near the interior corner due to the enhancement in current balance over these streamlines. (Top) Anode-organic interface profile of the confinement enhancement factor with superposed streamline colormap. 76

Figure 5.13:	Comparison of numerical model and experimental (from [143]) current enhancement results of nanopatterned PLED with structure: Al/MEH-PPV/PEDOT:PSS/ITO.....	77
Figure 5.14:	Comparison of numerical model and experimental (from [143]) luminance enhancement results of nanopatterned PLED with structure: Al/MEH-PPV/PEDOT:PSS/ITO.....	78
Figure 5.15:	Schematic showing dimensions of the nanoimprint press process applied to cathode, producing nanocolumn impressions at the cathode-organic interface.	79
Figure 5.16:	Barrier height shifts, $\Delta\Phi_{B,i}$, for the orders of magnitude patterning dimension. The half-pitch dimensions are 10, 50, 100, 500, 1000 nm, respectively.....	80
Figure 5.17:	Balance current enhancement factor, $F_{bal,i}$ over the nm- μ m length scales. The half-pitch dimensions are 10, 50, 100, 500, 1000 nm, respectively.....	80
Figure 5.18:	Confinement enhancement factor, $F_{cnf,i}$ over the nm- μ m length scales. The half-pitch dimensions are 10, 50, 100, 500, 1000 nm, respectively.	81
Figure 5.19:	Overall current enhancement factor, $F_{tot,i}$ the nm- μ m length scales. The half-pitch dimensions are 10, 50, 100, 500, 1000 nm, respectively.	81
Figure 5.20:	Overall recombination enhancement factor, $F_{rec,i}$ the nm- μ m length scales. The half-pitch dimensions are 10, 50, 100, 500, 1000 nm, respectively.....	82
Figure 5.21:	Enhancement factors for (A) balance, (B) confinement, (C) total current against original thickness T_{org} , (D) total current against T_{col} -reduced thickness and (E) total recombination. The enhancement factors universally show absolute maxima occurring at smallest half pitch. And, except for confinement, monotonically increase over all patterning geometries towards smaller half pitch.	83
Figure 6.1:	Photopic response curve, $V(\lambda)$. This function expresses the normalized perceived light intensity spectrum by the human eye. Data values from [157,158].....	86
Figure 6.2:	Picture of dipole emitter and coupling to waveguide modes and surface-plasmon polariton mode.	88
Figure 6.3:	Ray tracing of Lambertian emission in an OLED. Classical thin-film optics dictates roughly 20% of emitted light escapes a planar OLED architecture.	89
Figure 6.4:	Optical constants for ITO [169], NPB [170] and Al [171].	92
Figure 6.5:	Penetration depth of Al, $\delta_{p,Al}$ computed from data in [171]. This data validates the optically thick approximation for the Al cathode layer for the 50nm Al layer.	92

Figure 6.6:	Description of the physical OLED system under investigation using the FDTD solver. A dipole antenna is placed in the organic active layers to resemble the spontaneous emission of light. During the simulation, information regarding the energy of light is extracted as the “Transmission Data”. Using far-field transformation techniques, the far-field data can be extrapolated from the ITO-glass interface to the air-glass interface to acquire knowledge about the light energy that is emitted from the device.	94
Figure 6.7:	On top, X-dipole spectral, positional EQE for planar OLED. On bottom, Z-dipole spectral, positional EQE for a planar OLED.	95
Figure 6.8:	Dipole-averaged spectral, positional EQE for a planar OLED.	96
Figure 6.9:	Z-dipole external quantum efficiency. At top, Z-dipole EQE when including internal nanopatterning; at bottom, Z-dipole EQE for the planar device. The insets show the dipole location within the OLED environment.	97
Figure 6.10:	X-dipole external quantum efficiency. At top, X-dipole EQE when including internal nanopatterning; at bottom, X-dipole EQE for the planar device. The insets show the dipole location within the OLED environment.	98
Figure 6.11:	Y-dipole external quantum efficiency. At top, Y-dipole EQE when including internal nanopatterning; at bottom, Y-dipole EQE for the planar device. The insets show the dipole location within the OLED environment.	99
Figure 6.12:	Incoherent dipole (dipole-averaged) external quantum efficiency. At top, the incoherent dipole EQE when including internal nanopatterning; at bottom, incoherent dipole EQE for the planar device. The insets show the dipole location within the OLED environment.	100
Figure 6.13:	Normalized recombination map transformed from streamline grid to a rectangular grid. At left, a finely resolved rectangular grid mapping. At right, a logametric depiction of the same normalized recombination map at left.	102
Figure 6.14:	Z-Dipole external quantum efficiency (EQE) position map.	103
Figure 6.15:	X-Dipole external quantum efficiency (EQE) position map.	103
Figure 6.16:	Y-Dipole external quantum efficiency (EQE) position map.	104
Figure 6.17:	Isotropic external quantum efficiency (EQE) position map.	105
Figure 6.18:	Normalized external quantum efficiency maps transformed to a rectangular grid. From top to bottom, EQE at wavelneghts 475, 525 and 600nm. At left, a finely resolved rectangular grid mapping. At right, a logametric depiction of the same normalized recombination map at left.	106
Figure 6.19:	Overall spectral optical enhancement, $F_{opt,\lambda}$ (Equation 6.18).	107

Figure C.1:	Depiction of glove box deposition setup.	129
Figure C.2:	Process layout #1. Top: Numbered procedure for making OLED devices. Bottom: Connection schematic for OLED.	130
Figure C.3:	Process layout #2. Top: Numbered procedure for making OLED devices. Bottom: Connection schematic for process layout.....	131
Figure C.4:	Automated deposition setup. Workstation is connected via serial port to the quartz crystal monitor (QCM) and deposition power supply (PF). The instruments then control deposition power supply and record the deposition rate from the QCM.	133
Figure C.5:	Automated device characterization setup for L-J-V measurement and spectrometry of luminance. Programmatic integration of sourcemeter (SM), luminance gun (LG) and spectrometer (spec). A stage can be moved to test different devices on each slide.	134

List of Tables

Table 1.1:	Emissive display technologies.....	4
Table 4.1:	Summary of equations solved in this chapter	42
Table 6.1:	Maxwell Equations in both integral and differential forms [159].	89
Table B.1:	Summary of linearized Poisson equation implementation	123
Table B.2:	Summary of linearized Poisson equation implementation	124
Table B.3:	Summary of electron drift-diffusion equation.....	127

Acknowledgments

Above all, I would like to thank my family: Nick, Val and Joel for their open ears, laughter, patience, guidance and unconditional support over the years that I have been away from home.

To the many friends that I met at Cal over the years, you kept a smile on my face through an important period in my life. And, you gave me something to look forward to even through the challenging stages of my research.

I would like to thank my college ice hockey buddies from the University of Illinois and Cal Ice Hockey teams. What a great bunch of guys. We will, undoubtedly, be life-long friends.

To Tim Suen, Steve Barcelo, I would like to thank the both of you for the many intellectually stimulating conversations we had throughout the years, especially as the topic of our conversations changed from heat transfer to solid-state physics and semiconductor physics. I felt much of what I learned in graduate school came from our periodic lunchtime discussions.

To Professor Mao, my advisor, thank you for your guidance and support. Your calming attitude and positive outlook were very much appreciated. Also, thank you for giving me the freedom to pursue my own research interests. Without your help this research wouldn't have been possible.

To Professor Greif, thank you for your advice over the years; I always left our conversations with a big smile on my face. It was a privilege me to work with such an accomplished researcher and caring teacher. And, also thank you for showing such enthusiasm in helping me prepare this manuscript.

To Susan Lauer, thank you for always taking a minute out of your to stop by and say a few thoughtful words.

To Deang and Dongdong, thanks for your assistance teaching me the finer points of making devices. The meticulous methods you taught me have given me a new outlook on designing test setups.

To my committee members, Professor Grigoropoulos and Professor Subramanian, thank you for taking valuable time out of your busy schedules to go over my dissertation and in helping me advance through the stages of the doctoral process.

And, of course, to the many graduate students, post-docs and visiting researchers in our research group that have lent a helping hand or exchanged research ideas. I wish you best luck in all your future endeavors. A list includes: Ting Zhang, Deang Liu, Dongdong Wang, Tim Suen, Steve Barcelo, Coleman Kronawitter, Kenny Armijo, Russell Carrington, Heather Chiamori, Matt Rogers, Tony Ho, Vascillia Zorba, Xiaojun Zhang, Derrick Speaks, Travis Owens, Erin Canfield and Matt Beres.

Chapter 1. Introduction

1.1 Introduction to OLED technology

Organic electronics have emerged as contenders for an array of low cost electronic devices including organic light-emitting diodes (OLEDs), organic photovoltaics (OPVs) and organic thin-film transistors (OTFTs). The unique physical properties of organic materials are compatible with a variety of low cost, high throughput processes. Concomitantly, low-temperature deposition presents the opportunity to enable extremely thin, flexible devices. Further, owing to the limitless potential combinations of organic materials, tailored optoelectronic properties are afforded through organic chemistry. Unfortunately, organic materials possess the major disadvantage that their technologies are limited by the immaturity of their fields. The organic light-emitting diode (OLED) has become the flagship electronic device of organic electronics and, at present, is being commercialized in a variety of emissive display markets.

OLEDs are thin-film optoelectronic devices which harness the optoelectronic properties of organic semiconductors to control light emission. That is, OLEDs directly convert electrical energy into visible radiation. Champion OLED devices boast comparable efficiencies to industry-leading light-emitting technologies. There is, however, still substantial room for further improvement in OLED efficiency through introduction of specialized electronic and optical layers, understanding device characteristics and development of hybrid devices. This work will focus on understanding the role that structured surfaces have on a number of critical OLED efficiency metrics.

Moreover, the goals of this chapter are three-fold: (I) to provide a concise historical account of landmark papers which have culminated into the highly efficient OLEDs that are produced today; (II) to motivate device efficiency enhancements in OLEDs and provide an informal overview of two technologically relevant applications of OLEDs (solid-state lighting and microelectronics displays); and (III) to define the scope of this work and detail an outline for this document.

1.2 Historical Developments in Organic Electroluminescence

Light-emitting diodes (LEDs) have a rich history stretching back over a century. The first demonstration of electroluminescence dates back to 1907, when Round discovered light emission from SiC, or carborundum, using an antiquated cat's-whisker detector [1-3]. Round published only a brief note about his discovery. In that communication, Round suggests that the light emission had not occurred by carrier heating and, thus, his discovery represented a cold-cathode light-emission mechanism [3]. Years later, in the 1920s, SiC light emission was independently demonstrated by Lossev (referred to as Lossev effect, or DC electroluminescence) and further experimentation followed [2-5]. Lossev's work marked the first detailed study into the LED mechanism; moreover, through experimentation, he correctly concluded that the SiC light emission process had occurred through an inverted photo-electric effect [3,5].

In the mid-1930s, Destriau discovered improved luminance using naturally occurring ZnS phosphors, a II-VI group compound semiconductor, embedded within a dielectric medium operating in AC mode (referred to as Destriau effect, or AC electroluminescence) [3,6-8]. In 1955, Bernanose successfully demonstrated light emission from the Destriau effect using

organic compounds embedded in dry cellulose films [9,10]. During the late 1950s, thin-film LEDs (ZnS:Mn) were first shown to markedly increase luminance [11].

The 1950s also ushered in the era of synthetic III-V compound semiconductors for optoelectronics applications [2,12,13]. Aided by the improved theoretical understanding of electroluminescence, particularly, the bi-polar nature of semiconductors, the Lossev effect became the preferred current-driving method for high efficiency light-emitting applications [7,14]. A widespread investigation of p-n junction III-V materials for LEDs ensued. By the early 1960s, the first demonstration of spectral narrowing, or lasing action, was demonstrated in GaAsP while immersed in liquid helium [13]. The first commercialized LED (red, GaAsP) was produced by in the early 1960s by GE [2].

The early 1960s marked the first reports of the Lossev effect from organic crystals [16,17]. These works utilized relatively thick (thickness: μm -mm) crystals of anthracene (a much-studied luminescent aromatic hydrocarbon) for light emission deposited by molecular beam epitaxy (MBE).

The Destriau effect was first demonstrated in a polymer in 1967 [18]. During the 1970s, conductive polymers were introduced and furthered interest in organic electronics [19,20,48]. In 1973, a complex of tetrathiofulvalene (TTF) and tetracyanoquinonedimethane (TCNQ) demonstrated metallic conductivity [19,20]. The first commercially successful application of a solid-state organic, electronic material followed in the field of xerography [21]. Both small molecules, such as the phthalocynines and polymers, such as poly(vinyl carbazole) (or PVK) became highly studied [46]. In this field, the benefits of organic materials over industry-leading amorphous selenium included environmental friendliness, good electronic absorption properties and low-cost materials and deposition processes.

Following the commercial success of organic photoconducting materials, the first successful demonstration of a light-emitting PVK polymer EL device came in 1983 [47]. Device experimentation focused on thin-film device structures. Since drift current is related to electric field and electric field scales inversely with thickness, thin-film structures were capable of dramatically reducing device turn-on voltage. However, efficiency limitations persisted in the single-layer device structures due to the asymmetry inherent in material-dependent injection barriers and carrier mobilities within the device. Today, it is known that the asymmetries of the single-layer OLED render it difficult to control the location of the carrier recombination zone away from one of the electrodes in thin-film OLEDs. (Although a resurgent interest in literature associated with single-layer devices has occurred due to the simplicity of their processing [49-52].) Many studies have since shown that carrier recombination within close proximity to the metal-organic surface rapidly quenches excitons, or electron-hole pairs [22-24]. This phenomenon is related to the surface-plasmon coupling which occurs when a dipole emitter is placed in the near-field of a flat metal (energy absorbing) reflector, leading to an intensified radiation decay route [53,54].

Then, in 1987, Tang introduced the first highly efficient, heterojunction OLED (~1% external quantum efficiency) [25]. The organic-organic heterojunction (see Figure 1.1) established an energy-level mismatch at the material interface thereby confining charge carriers and significantly reducing exciton quenching at the electrodes. The electron transport layer used in this device was tris(8-hydroxyquinoline)Aluminum, or Alq₃, a green light-emitter. Alq₃, to this day, remains a popular lab-grade material for characterizing OLED device performance

enhancement. In fact, the baseline devices considered in this paper follow a similar material structure to those in the Tang paper.

Contemporaneously to Tang's work, research was being conducted by a collaboration of researchers to create an electroluminescent device based on the thermal conversion of a spin-coated precursor polymer [26]. This work featured a soluble route to the conductive polymer, PPV (see Figure 1.1). The success of this work captivated display experts with hopes of introducing an all-solution-processed, flexible polymer light-emitting devices (PLED); even though, this device had a much reduced quantum efficiency than the Tang work.

Following these works, researchers furthered OLED technology with ground-breaking work in organic chemistry and device physics. Today, more than 10,000 published journal articles exist on the topic. In the 20-plus years since the seminal works in small molecule organic light emitting diodes (SMOLED or OLED) and solution-processed polymer light-emitting diodes (PLED), a number of breakthroughs have occurred. A brief list of important innovations and reviews covering the topics of the improvement include singlet-triplet conversion [27,28], light outcoupling [29-32], efficient use of exciton structure [30], current injection layers [33] and chemical doping [34,35].

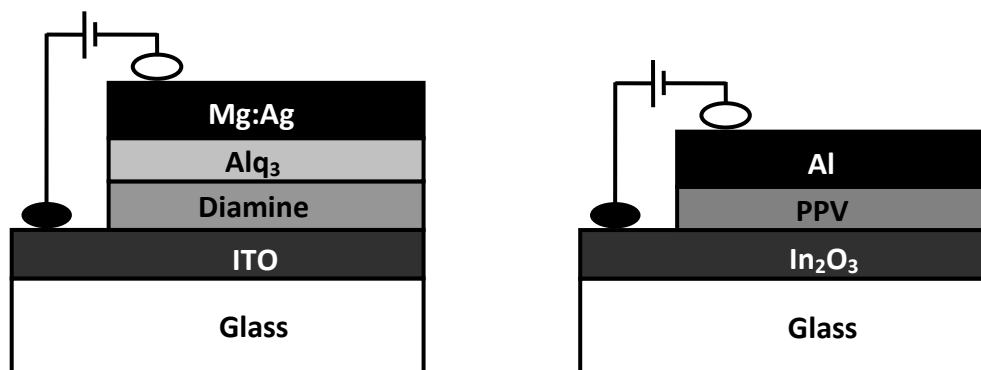
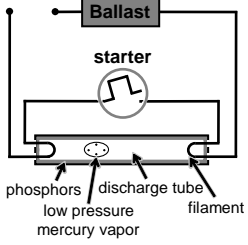
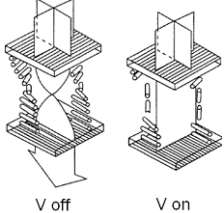
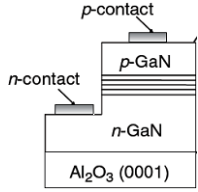
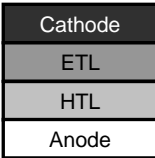
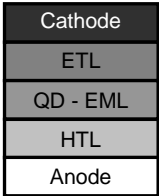


Figure 1.1: Landmark organic light-emitting devices. At left, the first highly-efficient small molecule organic light-emitting diode. This device utilized an organic bilayer to confine charges at the heterojunction [25]. More recent devices use NPB or TPD diamine molecules. At right, the first solution-processed polymer light-emitting diode [26].

1.3 OLED applications

OLEDs are a relatively recent addition to the pallet of light-emitting devices but have already begun to be commercialized in specialty display markets. This section will provide motivation for further commercialization of highly efficient solid-state light-emitting devices by citing technical documents and commercially successful products. The schematic in Table 1.1 compares several of the competing solid-state light-emitting technologies.

Table 1.1: Emissive display technologies

Technology	Fluorescent Tube 	LCD 	LED 	OLED 	QD-LED 
Operating principle	Discharge tube with low pressure Mercury vapor and a phosphor coating	Applied voltage induces liquid crystal rotation; anisotropic permittivity modulates light through optical filter	Applied voltage drives electrons and holes into an inorganic medium; excitations radiatively decay emitting light	Applied voltage drives electrons and holes into an organic medium; excitations radiatively decay emitting light	Applied voltage drives electrons and holes into a quantum dot medium which captures charges; decays emitting light
Advantages	Established industry standard for lighting; good efficiency	Established industry standard for displays; physics well understood; efficiency depends on backlight	Highest reported efficiency (GaN); uses standard deposition processes (MOCVD); device easily integrable; high device yield	Very efficient; materials may be tailored; not very susceptible to defects, processing; solution processing	Great optical properties; versatile, easily additive to LED processes; solution deposited
Disadvantages	Non-conformable; requires a ballast to control current; mercury, hazardous disposal	Require backlights; Polarization filter uses 50% luminance; ms response times	Require high purity, low defect material; typically use quantum wells (many layers); require vacuum deposition steps; use phosphors for downcoupling	Lacking CRI of quantum dots; require indium for triplet emission; research required	Low mobility; rather thick; more research required; materials tend to be toxic (uses Cd)

1.3.1 Solid-State Lighting

Solid-state lighting (SSL) is the solid-state electronic counterpart to vapor-based light bulbs used in both residential and commercial settings (e.g., incandescent bulbs and fluorescent bulbs). Solid-state electronic devices have a number of advantages to their vapor-phase equivalents. The principal motivation for SSL is that it has the ability to produce higher efficiency devices with better color rendering index (CRI) than fluorescent bulbs. Common examples where SSL is expected to garner industry favor include office lighting and other large-area displays such as billboards.

Highly efficient SSL is a cornerstone of the United States - Department of Energy's (USDOE) roadmap to the United States' energy independence [36]. Efficiency improvements in the commercial and residential lighting sectors have the potential to considerably reduce energy consumption. The consequent reductions to the United States' energy requirements can serve to reduce its dependence on both domestic and foreign energy sources. The amount of energy used for general lighting is staggering, estimated to be roughly 10% of the United States' annual energy consumption [36]. According to USDOE [36], "A nation-wide move toward solid-state lighting for general illumination could save a total of 32.5 quads of primary energy between 2012 and 2027." Current estimates place the United States annual energy consumption at roughly 100 quads (one quad is one quadrillion British thermal units or around 10^{18} Joules) [36,37]. This potential for substantial energy savings has spurred efforts to rapidly mature SSL technology through USDOE R&D grant opportunities. Additionally, future governmental incentives may also play an important role in successfully implementing this technology to homes and office buildings. Two distinct flavors of light-emission devices are currently being considered for SSL applications: LEDs [38] and OLEDs [39]. A third technology is quantum-dot LEDs (QD-LEDs) which can be used with both LEDs and OLEDs to improve color saturation. The differences between LEDs and OLEDs will become more apparent throughout the device physics background part of this report, appearing in [Chapter 2](#).

1.3.2 Microelectronic Displays

Another touted application of OLEDs is for future generations of microelectronic displays, which include mobile telephones and high-end televisions (TVs) [41]. These two industries can be characterized as rapidly growing, highly profitable marketplaces. Technical reports composed by several sources expect rapid growth and penetration of OLEDs into the microelectronics industry; the extrapolated figures expect market growth to \$10 billion per year by 2020 [42] and \$20 billion per year by 2016 [43]. In contrast to SSL, which has been heavily government funded, the sponsors of microelectronics technologies are corporations who have vested stakes in the displays industry. It is interesting to note that many of the companies holding the proprietary rights to OLED materials and manufacturing technologies are the same companies who are industrial leaders in previous light-emitting technologies, e.g. LCD and LED-backlit LCD (market players include LG and Samsung). Since OLED microelectronic applications are commercialized through private corporations, much of the R&D for these technologies is performed by these companies.

OLEDs have recently been commercialized into full-color displays in mobile telephones (see [Figure 1.2](#)). The *Samsung Galaxy S* and *Google Nexus One* are current generation mobile phones which have both recently incorporated active-matrix OLED (AMOLED) displays. The

short average user lifetime of mobile phones and the size of the display size has allowed for integration into devices. On the other hand, the introduction of OLEDs into the television arena has been more sluggish and has not yet proved to be commercially viable (e.g. *Sony XEL-1* and *LG 15EL9500*). The high prices of such televisions have proved too expensive to presently achieve commercial success. High costs may be overcome in the near future as the economies of scale for mass production of OLEDs take effect.



Figure 1.2: Commercialized OLED devices: OLED TVs, (A) Sony XEL-1 and (B) LG 15EL9500; AMOLED mobile phones, (C) Samsung Galaxy S and (D) Google Nexus One; digital camera, Kodak LS633; car stereo, Pioneer DEH-9200R.

1.4 Scope of work – Efficiency influences of patterning OLEDs

While OLEDs have achieved commercial success, efficiency may be improved through incorporation of nanostructured materials. In contrast to inorganic LEDs, which require highly crystalline materials (and also lattice-matched substrates), organic materials may be deposited with less restrictions on crystallinity and are “soft” materials, allowing for compressive indentation. In practice, this affords the opportunity for nanoimprint lithography to modify the cavity of the OLED device. This work will focus on the previously unstudied electrical effects resulting from incorporation of modified layers. The optical effects are additionally considered, offering a complete picture of the efficiency effects due to nanopatterned OLEDs.

1.4.1 Electrical enhancement from nanopatterned organic layer

In [Figure 1.3](#), it is shown that geometric modification of the structure of an organic medium leads to asymmetrical current enhancement effects. Geometric modification can be produced using nanoimprint patterning. This process can be used to balance charge injection while simultaneously enhancing current efficiency. Simulations are conducted introducing a novel, carrier decoupled, injection limited framework to assess the potential for improved current flow in OLED devices as a result of nanostructuring. Moreover, the model will be validated against a complete numerical simulation of the semiconductor equations.

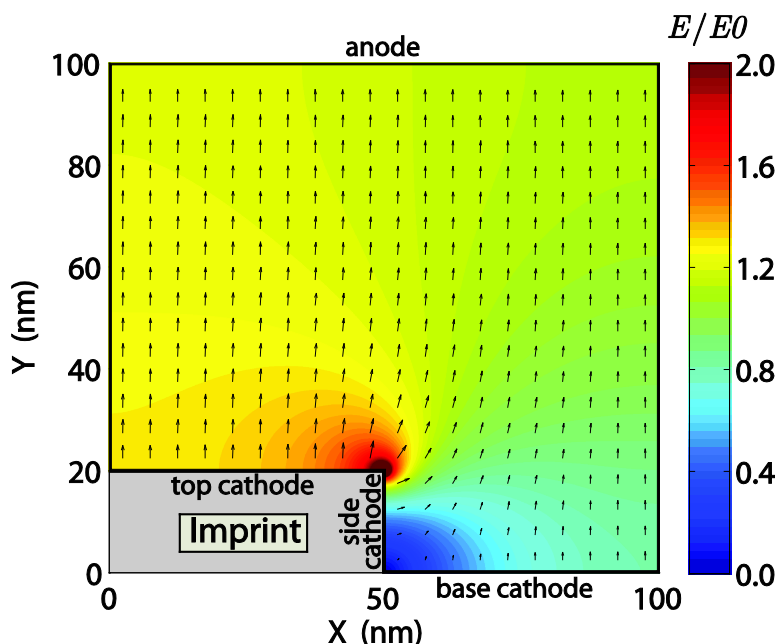


Figure 1.3: An example colormap demonstrating the electric field enhancement occurring from device structural modification. This example is explained in more detail in [Chapter 5](#).

1.4.2 Optical enhancement from nanopatterned organic layer

Light extraction in OLEDs is regarded as a major obstacle to OLED device improvement. As demonstrated in [Figure 1.4](#), the incorporation of nanostructured optical materials can be used to modify the light extraction from an OLED optical cavity. First-order approximations of light extraction are that for planar OLEDs <20% of emitted light leaves the device as visible radiation. According to the 2009 US DOE SSL Manufacturing Roadmap [36], "Support for manufacturing implementation of these techniques [out-coupling enhancement structures] should be given high priority. The fraction of created light that escapes from the device should be increased to 50% by 2012 and 70% by 2015. Low-cost fabrication techniques that are scalable to large area substrates and are consistent with average cycle times given above need to be found." This work focuses on using scalable processing to enhance light output. The optical effects from the cavity and material modifications are examined using commercial finite-difference time-domain

(FDTD) software.

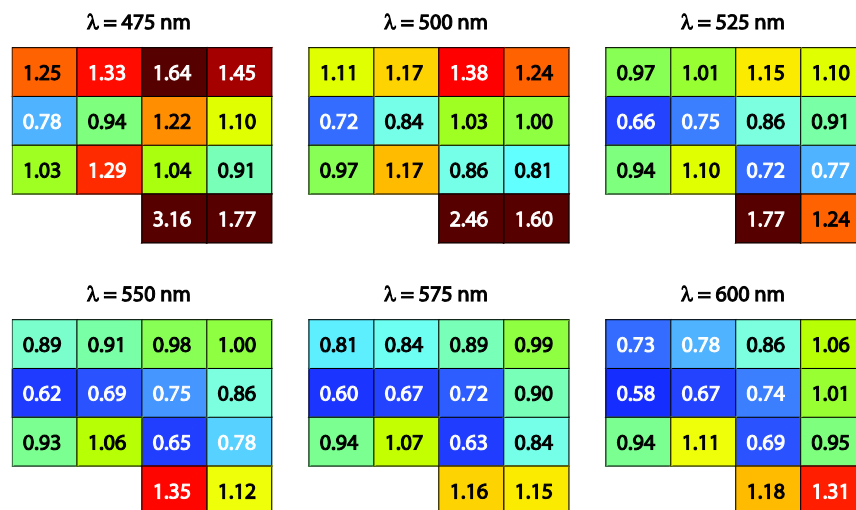


Figure 1.4: An illustration showing the power extraction modification resulting from internally patterned cathode interface. This example is explained in more detail in [Chapter 6](#).

1.5 Dissertation outline

This section will briefly outline this dissertation. The next two chapters are introductory in nature. [Chapter 2](#) encompasses introductory treatment of organic semiconducting materials for optoelectronic processes. [Chapter 3](#) introduces the device physics of OLED devices, which includes the theory of charge injection and transport and gives insight into the theory of current regimes in OLED devices. [Chapter 4](#) introduces conventional numerical procedure for solving the space-charge-limited single-layer OLED using the Scott-Malliaras injection mechanism. [Chapter 5](#) introduces a semi-analytical approximation for the nanopatterned, injection limited, single-layer OLED electrical enhancement and includes a detailed analysis of the enhancement effects. The model is compared to experiments. [Chapter 6](#) uses the results from the previous two chapters to approximate the optical effects arising from the optical environment for the specific geometries and optical materials included. Finally, [Chapter 7](#) discusses potential directions for future OLED research and summarizes the results of this work.

Chapter 2. Organic Electronic Materials

2.1 Introduction

Classical semiconductors consist of group IV or III-V inorganic materials such as Si, GaAs and Ge and utilize a crystalline morphology [55,56]. Silicon is the most widely studied semiconducting material and is responsible for the commercial success of MOSFET microprocessor industry. Even though there is growing interest in thin-film technology, Si remains the current industry leader in solar cell technology. The semiconductor industry has worked in synergy with advances in photolithography to uphold Moore's Law [57], which has led to high fidelity semiconductor processing at nanoscale feature sizes. Organic and polymeric materials represent a more recent class of semiconductors with fundamentally different properties than inorganic materials. Further, organic and polymeric materials enable novel processing techniques which are not accessible to inorganic materials [58]. The versatility of organic materials lend well to a host of novel applications [59]. This chapter will discuss the material properties of this classification of materials and serve to differentiate organic materials from inorganic materials.

2.2 Classifications of organic materials

There are three distinguishable forms of organic semiconducting materials; these include crystalline organics, e.g. anthracene (a polyacene); small molecule organics, e.g. Alq₃; and polymers, e.g. PPV. Figure 2.1 shows the chemical structure of these materials.

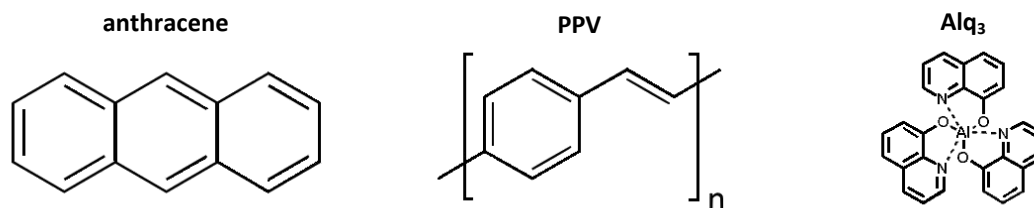


Figure 2.1: Prototypical organic light-emitting materials. At left, anthracene, a crystalline organic material used in early literature; at middle, poly(p-phenylene vinylene) (PPV), a conducting polymer used in early polymer light-emitting diodes; at right, tris(8-hydroxyquinoline)aluminum (Alq₃), a small molecule organic used in early small molecule OLEDs.

Each of these classes has unique properties and applications for which they are preferred. Polyacenes are researched for their use in OFETs (organic field-effect transistors) and OTFTs (organic thin-film transistors), where the carrier mobility is the critical metric [59]. Interestingly, polymers are researched for low cost, lower performance OFET and OTFT applications. All three material classes have superior optoelectronic properties which are advantageous for both photovoltaic and light-emitting applications. Polymer photovoltaic cells have become an area of intense research, with lab-grade peak efficiencies of ~8% [60]. OLED efficiencies lag behind LED efficiencies but have foreseeable advantages to inorganic technologies. In OLED applications, crystalline organics have fallen out of interest as viable OLED materials due to additional processing restrictions required for achieving crystalline morphology. The primary focus of this

work will be on the small molecule class of materials. Moreover, unless otherwise mentioned, the term *organic* refers to small molecule materials. The principal features which separate these material classes are bonding and crystallinity. These topics will be discussed in more depth in the coming sections.

2.3 Molecular bonding

Organic materials experience a different physical environment than inorganic materials; conceptually, this accounts for many of the differences in material properties [61,62]. Inorganic materials are bound by strong covalent bonds, resulting in bond strengths of 2-4eV [63]. Organic materials, on the other hand, possess two different types of bonding energies, intramolecular and intermolecular. In fact, all organic materials share this as a common bonding paradigm. They are internally bound by conjugated carbon bond architectures. And, they exhibit weak intermolecular bonding. Moreover, even though there are a limitless number of organic and polymers materials, a surprising number of material properties may be attributed to their bonding characteristics [61-64]. Figure 2.2 shows a comparison of bonding and carrier transport in organic and inorganic materials.

Intermolecular bonding in organic materials is the result of relatively weak intermolecular interactions (roughly 0.1-0.3eV) occurring through hydrogen bonds, dipole-dipole bonds or functional groups which passivate otherwise dangling carbon bonds [63-67]). The weak intermolecular bond strengths in organics lead to substantially reduced bandwidth for carrier transport [66]. Thus, the overall result of weak bonding is large charge localization effects. An important consequence of localized charges is large polarization energy. Strong polarization effects are brought about from reduced carrier screening and, thus, low material permittivity is observed in organics when compared to inorganic materials [63]. Moreover, the consequences of weak bonding and strong polarization have further implications extending to electronic transport and to the degree of charge localization, which will be discussed later in this chapter.

Organic materials are internally bound via strong, covalent σ -bonding and have π -conjugated backbones [10,63,65,66]. An example of π -conjugation can be seen in the chemical bonding of anthracene in Figure 2.1. The carbon molecular orbitals hybridize, or convert from atomic orbitals to bonding orbitals, to form sp^2 bonds. The lower energy σ -bonds create the scaffolding which shapes the rigid geometry of the molecule. Higher energy π -bonds, formed by $2p_z$ orbitals, become relatively delocalized throughout the molecule due to the overlapping wave functions between the $2p_z$ orbitals (i.e., resonant configurations of the electron structure) [63-67]. Therefore, strong intramolecular bonding leads to delocalized intramolecular electronic transport. Resulting from the electronic configuration of the bonding and anti-bonding structures, the highest occupied molecular orbital (HOMO, or π) and the lowest unoccupied molecular orbital (LUMO, or π^*) produce an energy gap [10]. The $\pi - \pi^*$ (optical gap) transition for a bound electron-hole pair, or exciton, usually occurs in the visible region of the electromagnetic spectrum (wavelength between 400nm and 700nm; energy roughly between 2 and 3 eV) [10]. These transition energies are conducive to optoelectronic processes [65,66,68,69]. Another favorable optoelectronic property of organic materials is the strong exciton binding energy ($E_{bind} \sim 0.3eV$) required to dissociate an electron-hole pair. Large exciton binding energy arises from the amount of energy required to separate the correlated carriers which are trapped in each other's potential well, a further result of strong material

polarization and localized wave function effects. In OLEDs, the strong exciton binding energy reduces the probability of thermal exciton dissociation [64] and, in effect, reduces radiation quenching routes which are very detrimental to LED efficiency. Owing to the vast number of organic and polymeric materials, organic materials may be chosen to ideally suit a particular optoelectronic application. The abundance of chemical compounds available to organic materials permits tailored optoelectronic properties and is in contrast with crystalline, inorganic materials used for inorganic light-emitting diodes where a limited assortment of direct band gap light emission materials exists (and all material compositions may not be stoichiometrically favored).

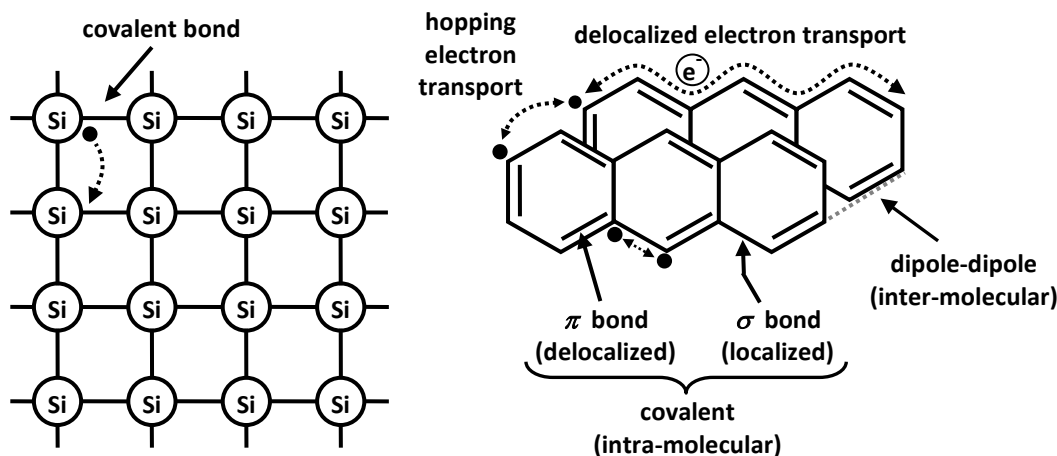


Figure 2.2: Comparison of bonding in inorganic and organic materials. At left, Si is tetrahedrally bound (picture above is a 2-d planar simplification to 3-d structure) to three adjacent Si atoms; at right, anthracene bonding includes intra-molecular covalent bonding and inter-molecular dipole-dipole bonding. The intramolecular bonds include σ -bonds (localized) and π -bonds (delocalized, contribute to electron transport) and intermolecular bonds which are localized due to weak interaction forces. Transport of holes is analogous.

2.4 Morphology

Morphology plays a critical role in the electrical properties and electronic processes occurring in a material. According to Bloch wave theory, the periodic nature of the crystal lattice produces an electronic regularity, or symmetry, which significantly reduces scattering events during carrier motion, such a reduction in scattering events serves to greatly improve carrier mobility [70]. In inorganic materials, the periodic spacing of the lattice controls the material's electronic properties including the electronic band gap. Despite the overwhelming favor for crystallinity in inorganic materials, differences in material properties, device dimensions and the potential for low-cost processing in organic materials suggest that an amorphous (or perhaps more accurately, nanocrystalline; henceforth referred to as *non-crystalline*) morphology may be particularly well suited for OLED application. In particular to OLEDs, non-crystalline morphology serves several advantages. Beyond the ability for low-cost,

high-throughput deposition, a processing advantage of non-crystalline morphologies is the lack of restrictions on substrate material onto which the organic film is grown. (Mismatched substrates have proven to be problematic to industry-leading crystalline GaN light-emitting diodes because the resulting surface dislocations increase excitation decay routes.) In OLEDs, there has been work showing that polycrystalline grain boundaries may lead to increased excitation quenching sites compared to the non-crystalline morphology [23]. Further, non-crystalline materials possess excellent deposition properties including the ability to form ultra-thin, conformable and planar layers. As discussed above, the primary detriment of the non-crystalline morphology leads to reduced carrier mobility. This does not prove to be a major problem from an efficiency standpoint.

2.5 Processing

The weak intermolecular bonding found in organic materials has a direct relation to the energy required to break bonds for material deposition and processing. For example, the glass transition temperature of commonplace organic materials, NPD and NPB are ~60-100°C [61]. Deposition of common bulk inorganic materials ranges from roughly 330°C (lead) to roughly 3500 °C (tungsten, tantalum) [71]. Moreover, the ability to take advantage of rapid deposition processes for depositing non-crystalline materials improves throughput. These two ideas are central to the processing advantages of organic materials over inorganic materials and reveal part of the scientific interest and fascination with organic electronics. Further, it is expected that the simple processing of organic materials can remove expensive photolithographic processes in lieu of a host of novel deposition processes (e.g., transfer processing, inkjet, gravure and flexographic printing material processes [58,62,72]). These processes are available to weakly bonded materials and represent a future pathway to low-cost semiconducting materials utilizing high-throughput processes to achieve integrated devices. The marketplaces these devices are expected to succeed in are those which do not require the level of quality materials needed in the microprocessor industry. Indeed, the low deposition temperatures used in OLED technology are also compatible with flexible, plastic substrates which may open up opportunities for flexible electronic applications [62,73]. Figure 2.3 depicts the two primary deposition processes utilized in this work to deposit organic and specialized optical materials. These methods are thermal evaporation and spin coating. Thermal evaporation is a scalable industry standard deposition process for depositing controlled organic materials using single material (neat) and co-evaporation techniques. In this work we do not consider co-evaporation. Spin coating is a non-scalable, lab-grade deposition process that can be used to deposit a wide variety of solution processable materials. However, on a commercial scale, spin coating processes may be replaced by inkjet printing or other previously mentioned roll-to-roll process.

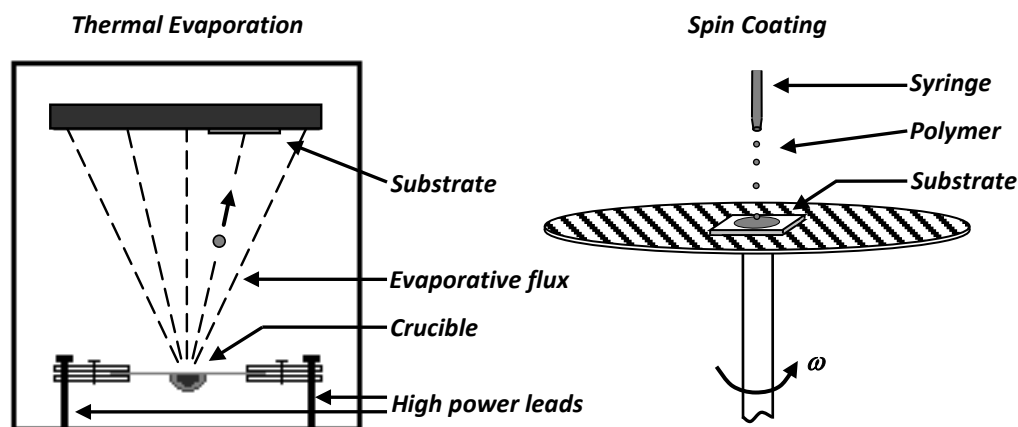


Figure 2.3: Schematic of lab-grade deposition processes used in this work. At left, thermal evaporation via sublimation from crucible; at right, spin-coating deposition from solution.

2.6 Localization effects

The mechanism for electronic transport in organic materials is a frequent topic of discussion. The topic receives much attention because of influence of the transport mechanism on device operation (and, ultimately, device efficiency). To proceed we must again begin with consideration of the bonding and morphology of these materials. As a result of the weak intermolecular forces present, there is a narrow electronic bandwidth (~ 100 meV). The non-crystalline morphology leads to strong energetic and positional disorder. Under such conditions, the charge transport mechanism is controlled by a hopping-type process [63-67]. In particular, a phonon-assisted hopping mechanism prevails. The large polarization energy must be overcome to enable charge transport. Thus charge transport occurs via energy band localized states occurring in the tail of a Gaussian DOS. The Gaussian DOS arises from the large polarization energy within the material and the random distances between molecules within the organic material [63-67]. Anderson Localization begins to occur as the disorder is increased in organic materials, extended states near the band edge begin to localize as the disorder exceeds the bandwidth [91]. Sources of disorder include positional and polarization disorder as well as dipole disorder. Ultimately, the mean free path of carrier motion is on the order of the molecular spacing and the hopping transport formalism is commonly used. Furthermore, the transport mechanism is vastly different from traditional semiconductor technologies. A variety of formalisms have been employed over the years to explain how charges are transferred through a disordered medium. Several of these mechanisms will be described in Section 3.2.

2.7 Mobility

Organic materials have exceptional optoelectronic properties. However, these specialized properties in non-crystalline organics materials come at the cost of reduced carrier mobilities. It should also be noted that the mobility in organic materials is typically orders of magnitude lower than inorganic materials (e.g. GaAs room temperature electron mobility is roughly 8500 cm²/V – s [55]). Organic materials typically possess a field-dependent mobility on the

order of 10^{-6} to $10^{-3} \text{ cm}^2/\text{V} - \text{s}$ for holes with one to two orders of magnitude lower mobilities for electron carriers [61]. Carrier mobility is crucial for device switching speed. But in light-emission devices the switching speed need not be much faster than perceptible by the human eye (order of tens-of-milliseconds). And, indeed, the switching speed of organic materials is much faster than the switching speed of liquid crystal displays (LCDs). LCDs switching speed revolves around the time which the liquid crystals are capable of realigning due to an applied electric field (which invokes physical rotation due to the anisotropic dielectric constant). The LCD switching parameter is then related to the visco-elastic transient time scale of the liquid crystal molecules, which is slower than the typical carrier velocities in organic materials. Thus the low mobility does not place any further limitations on the switching speed for OLED operation. Low mobility also leads to resistive materials; however, the molecularly doped layers (through co-evaporation) has led to very high mobilities in organic materials by adjusting the quasi-Fermi level of the material beyond the HOMO(LUMO) level using a donor(acceptor) molecule [34].

Another interesting feature of such low mobility, high band gap materials is that they would classically be considered as insulators due to low intrinsic carrier concentration. High carrier concentrations are established through injection at the contacts. In fact it is the high field operating condition of OLEDs that is required to achieve operating voltages nearing the emission quantum voltage ($\Delta V = hc/q\lambda$). That is, high electric fields ($\sim 10^6 \text{ V/cm}$) are required for optimal carrier injection and transport. In order to achieve these electric fields near the emission quantum voltage, the overall device thickness must be on the order of 100nm [10]. As will be discussed later in Chapter 6, there are near-field optical cavity issues which arise due to the resulting thin-film OLED architecture.

2.8 Band or Hopping transport?

The modeling of current flow in organic devices has a storied history. It was long ago recognized that delocalized, free electron assumptions applicable for traditional (inorganic, crystalline semiconductors) is not immediately satisfied in these materials [63-66]. It would appear though that the characteristics of the carrier transport in crystalline materials can be well-approximated by the band model [63-66]. With the similar mobility dependence on temperature suggesting that the similar phonon limited (high temperature) and impurity limited (low temperature) regimes exist. However, this result is not followed for non-crystalline organic materials. In fact, the mobility is enhanced at high temperatures, suggesting that phonons assist transport [63-66]. Of course, due to the lack of initial understanding of the physics of organic materials, preliminary transport theories followed treatments similar to amorphous silicon, i.e. the multiple trap and release (MTR) formalism which assumes trapping intermittent, extended state transport. However, it was realized that the level of localization in these materials, severely limits extended state transport and favors a hopping-type transport mechanism, whereby transport between localized states occurs.

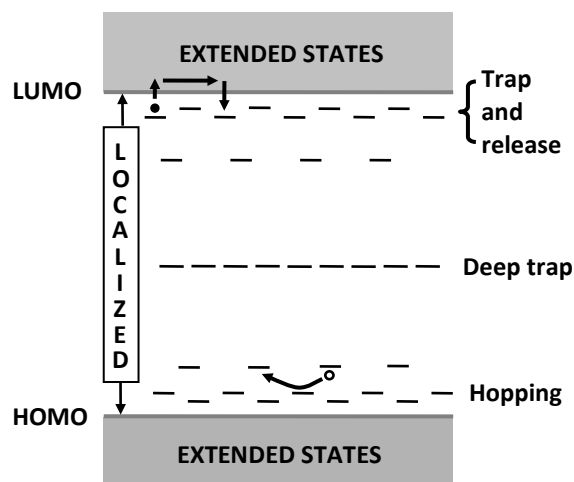


Figure 2.4: Band versus hopping type electron transport. Classically, in inorganic semiconductors, carrier transport occurs through extended state transport. In organic materials, carriers become localized and hopping transport results [65]. The figure shows distinction between multiple trap and release and hopping transport.

2.9 Excitons: Energy Transfer and Optoelectronic Processes

Until now much of the discussion has focused on charge carriers. The essence of LEDs and OLEDs is to produce and harness the useful light generated from spontaneous dipole radiative decay. Excitons (or bound electron-hole pairs), thus, serve as an intermediate in the emission mechanism. This section will discuss the properties and processes of excitons in organic materials.

The types of excitons which exist in organic materials are very different from those in inorganic materials. Inorganic materials, which have delocalized carriers, have wave functions which can stretch several nanometers and therefore an exciton may weakly bind carriers over a relatively large distance. This type of exciton is referred to as a *Wannier-Mott exciton* [65]. The types of excitons occurring in organic materials have very localized wave functions and thus the excitons exhibit tight bonding at very short distances. The excitons in organic materials fall into two categories, Frankel and charge transfer excitons. *Frenkel excitons* occur when an electron and a hole are situated on the same molecule and have much larger exciton energies than the Wannier-Mott excitons in inorganic materials. *Charge transfer excitons* are formed when the carriers reside on a neighboring molecule. Charge-transfer exciton formation is more likely in molecular crystals [74]. These results can be shown below in [Figure 2.5](#).

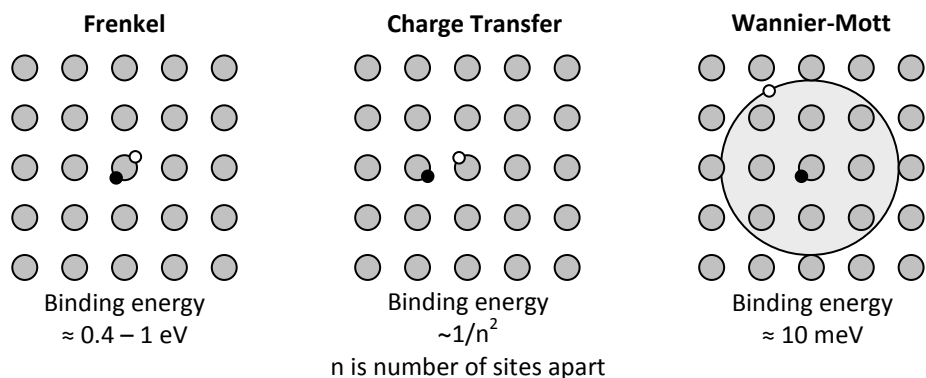


Figure 2.5: Semiconductor excitonic binding types in lattice space. At left, Frenkel exciton (common in organic semiconductors). At middle, Charge Transfer exciton (common in organic semiconductors). At right, Wannier-Mott excitons (common in inorganic semiconductors). After [65,70].

After excitons are formed, excitons require time to decay. The decay process is statistical and is dependent on the spin of the exciton and surrounding material environment. During this period of time, excitons are transported around within the material. The transport mechanism occurs via three well-known mechanisms. *Trivial exciton transfer* occurs when a photon is emitted and then, subsequently, is reabsorbed by another molecule. This process leads to a red-shifted exciton and requires an overlap of the emission and absorption spectra of the emitting and absorbing molecule. *Förster exciton transfer* is a second transfer mechanism (occurring up to several nanometers [65]). In this process, a singlet exciton may be transported through a material by inducing a dipole-dipole interaction between two molecular states. The selectivity of this process is related to the emission-absorption overlap and the effectiveness of the interaction falls off as $1/R^6$, where R is the distance between the donor-acceptor pair (nm). *Dexter exciton transfer* is a tunneling effect (occurring up to several ångströms [65]) which does not have a singlet selection rule; thus, triplet transfer may additionally occur through this process. See Figure 2.6 for a pictorial description of these energy transfer processes.

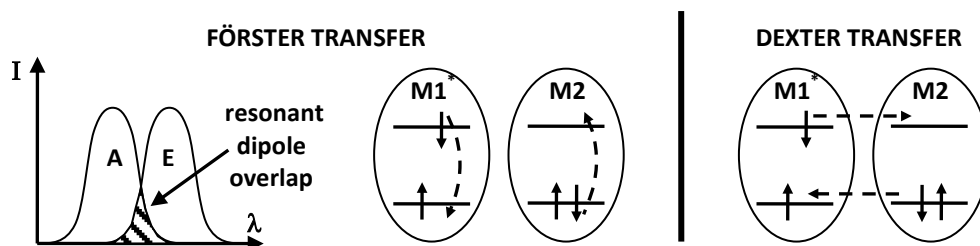


Figure 2.6: Exciton transfer processes. At left, Förster exciton transfer, when exciton transfer occurs via dipole-dipole resonance. This process occurs for singlet-singlet excitons. At right, Dexter transfer, short-range exciton tunneling. $M1^*$ is the excited donor molecule and $M2$ is ground state acceptor molecule. Superscript * denotes an excited state.

According to spin statistics, two quantum mechanically distinguishable manifolds of excitons are produced. One-fourth (25%) of the total excitons will form fluorescent, singlet excitons which have a radiative decay time on the order of nanoseconds ($\sim 10^{-9}$ s) [65,75]. The remaining three-fourths (75%) of excitons formed are the triplet variety and are, therefore, quantum-mechanically forbidden from emitting light, with radiative decay times on the order of microseconds to seconds ($\sim 10^{-6}$ -1 s) to emit phosphorescent light [65,75]. Unfortunately, long-lasting triplet excitons without specialized confinement or phosphorescent conversion will non-radiatively decay, or becoming quenched at the metal-organic surface [75]. Processes which undergo non-radiative decay emit phonons, which in effect raise the thermal energy of the material. Figure 2.7 shows a Jablonski diagram, which features the possible mechanisms and timescales of excitonic processes.

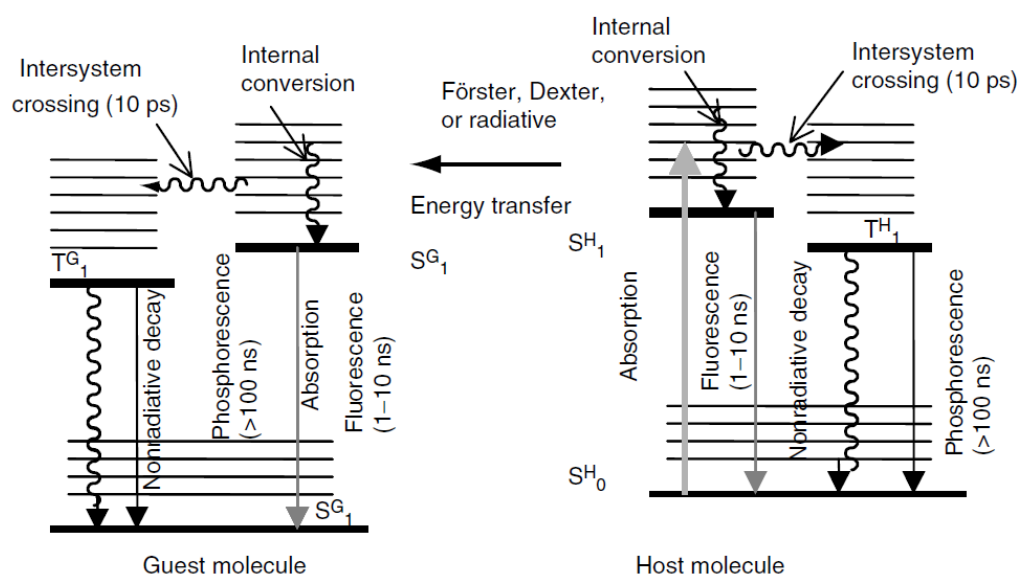


Figure 2.7: Jablonski diagram. Showing electronic processes in organic materials related to host-guest materials. Two systems exist singlet and triplet manifolds, from [152].

2.10 Conclusion

This section described several basic differences between organic electronic materials and their inorganic counterparts and explained important optoelectronic processes in organic materials. While generalities were made in this chapter about organic materials, a caveat must be issued. Organic materials may be strongly influenced by the functional groups which can be used to modify them [61]. As mentioned above simplified deposition, mechanical flexibility and material tailoring provides strong incentive for further inclusion of organic electronic materials into future electronic devices. It is from these fundamental differences that organic electronics are expected to complement inorganic semiconducting devices in fields where the ability for novel devices such as flexibility and ultra-thin, simply fabricated layers are required.

Chapter 3. Theory of OLED Electrical Operation

3.1 Introduction

The theoretical concepts and models of electrical device operation in organic materials and OLEDs will be introduced within this chapter. In OLEDs, the electrical system accounts for the first of three processes leading to light emission. Briefly, the electrical system involves carrier injection, transport and recombination of electrons and holes, which equivalently corresponds to the generation of excitons. The excitons participate in energy transfer and conversion processes. In cases where radiative, quantum-mechanically-favored exciton decay pathways occur, spontaneous dipole emission produces photon emission. Light outcoupling may then occur but depends on the optical environment. An energy band diagram of the steps culminating in light emission is depicted in Figure 3.1.

This chapter will begin with discussion of common transport models and simulations. Next, physical descriptions of the current injection mechanisms will be introduced including discussion on metal-organic barrier formation. Finally, a description of the coupling between carrier transport and injection is introduced, which lead to the description of the space-charge-limited current regime. Furthermore, the concepts introduced here provide a useful preliminary to the OLED-specific continuum model which is considered in more detail in the following chapters to evaluate the effects of the nanostructured OLED electrical system.

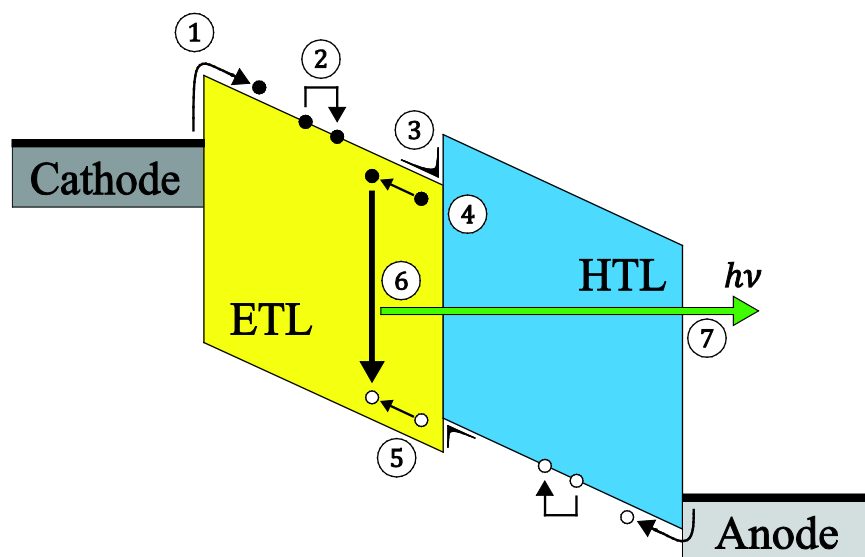


Figure 3.1: Energy band diagram of OLED emission mechanism under applied field. The following processes culminate in sensible light emission: (1) carrier injection; (2) carrier transport; (3) carrier accumulation at heterojunction; (4) carrier recombination / exciton formation; (5) exciton diffusion; (6) exciton radiative decay / photon internal emission; and (7) photon exiting device (external). Processes 1-4 are related to the electrical system [24,65,66,77,89]. Processes 4-6 are related to the exciton system [23,75]. Processes 6-7 are related to the photon system [31,78,79]. Acronyms used in diagram: HTL, hole transport layer; ETL, electron transport layer.

3.2 Charge Transport Models

Two types of analysis are used to describe carrier transport in OLED devices. The distinguishing factor between the types of analysis is the level of statistical incorporation within the numerical evaluation. Below, a common implementation of the statistical Monte Carlo simulation is discussed [76]. In addition, two types of continuum-based models will be introduced; these include the Master equation model [81] and the classical semiconductor equations (also known as the drift-diffusion equations) [82,83].

To elucidate the difference between statistical simulations and continuum models: fully statistical models such as Monte Carlo methods have access to the most fundamental aspects of charge transport such as density of states (DOS) and definition of the charge transfer mechanism; whereas, continuum models lump key transport properties into theoretically derived or experimentally determined effective mobility. In literature, continuum models have incorporated effective carrier mobilities determined from a number of experimental techniques including time-of-flight measurements (TOF) [84], time-resolved electroluminescence (TREL) [85], admittance spectroscopy (AS) [86], dark-injection space-charge-limited current (DISCLC) and field-effect mobility [87] (transistor architecture useful for OFET, OTFT configurations). In addition, it is common to empirically generalize the field and temperature dependence of mobility through the Poole-Frankel mechanism (introduced later in Equations 3.3-3.4) [80], which bear a physical similarity to intermolecular carrier tunneling. To summarize, continuum-type models are frequently used for device-level studies; whereas, statistical simulations are more apt at fundamental transport studies.

3.2.1 Monte Carlo Simulation

The objective of numerical simulation is to better understand the transport mechanisms over a broad range of conditions including the electronic structure and temperature. Utilizing direct statistical incorporation into the transport equations, Monte Carlo simulations offer unrivaled freedom in defining the charge transport mechanism. An article by Bässler [80] outlines many of the methods and concepts used in Monte Carlo simulations. This study compares predicted mobilities of common organic photoconductors with TOF mobilities. Within Bässler's this work, a fixed number of charges are introduced at an electrode and allowed to drift through an organic medium abiding by the simulation-defined rules of charge transport. A Gaussian Disorder Model (GDM) is used to describe the DOS within the disordered, organic semiconducting medium. Mathematically, the GDM's DOS, ρ , is expressed by the following relationship:

$$\rho(\epsilon) = (2\pi\sigma^2)^{-1/2} \exp\left(-\frac{\epsilon^2}{2\sigma^2}\right) \quad 3.1$$

where ϵ is the energy relative to the center of the density of states, and σ is related to the energetic disorder of the material. Transport between occupied states occurs through energetically favored hops between localized states (see Figure 3.2). The commonplace Miller-Abrahams theory is applied to predict the frequency at which transport occurs between states of varying energy levels and relative hopping distance, ν_{ij} , as follows:

$$v_{ij} = v_0 \exp(-2\gamma\Delta R_{ij}) \begin{cases} \exp\left(-\frac{\epsilon_j - \epsilon_i}{k_B T}\right), & \epsilon_j > \epsilon_i \\ 1, & \epsilon_j < \epsilon_i \end{cases} \quad 3.2$$

where v_0 is the hopping attempt rate, $\epsilon_{i(j)}$ is the local absolute energy levels of the respective occupied and unoccupied energy states, ΔR_{ij} is the hopping distance, γ is the inverse localization radius (physically related to the wave function overlap integral) [90]. Figure 3.2 graphically depicts the transport process from within the GDM manifold under an applied electric field. The numerical procedure is initiated with a number of charges at a starting contact. Under an applied electric field, the charges are then propelled through the organic medium according to hopping rates (and the corresponding probabilities) specified by the model. Current is then registered as the carriers reach the counter-electrode. The numerical results were then compared to experimental TOF results, which allowed comparison with the numerical model. The results succeeded in explaining important aspects of the anomalous dispersive theory of transient photocurrent developed by Scher-Montroll [88]. Monte Carlo works also led to a better physical understanding of the agreement between field-effect mobility and the Poole-Frankel mechanism [65,66,80,89,90]. However, in practice, the Monte Carlo simulation method requires large and time-consuming simulations to produce confident statistical simulations. In addition, this simulation does not permit coupling to the injection mechanism. Furthermore, the Monte Carlo results lend better to bulk transport studies than device studies. As such, this method is not further considered in this work.

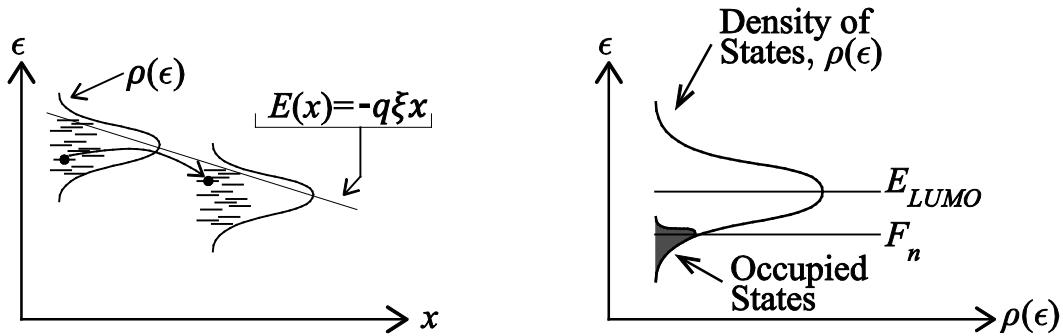


Figure 3.2: Image depicting electron occupation and transport in a statistical framework. At left, electron hopping in presence of electric field. At right, energy levels within Gaussian density of states with occupied states near the electron quasi-Fermi potential level, F_n . Adapted from [67].

3.2.2 Semiconductor Equations

An essential objective for OLED device models is the ability to predict the carrier injection rates and carrier current densities within the device. Continuum models also yield predictions to many pertinent internal device parameters such as carrier concentrations, recombination rate and electric field. However, before using applying the semiconductor equations several considerations regarding equation-set validity should be mentioned. In the past decades,

Moore's Law has been upheld, and as minimum device feature size of a number of devices have been reduced into the ballistic transport regime (few scattering events occurs over device traversal), the validity of these equations must be reevaluated. For example, for state-of-the-art MOSFET (metal-oxide-semiconductor field-effect transistor) devices, which have minimum feature sizes currently at the 22nm node, the semiconductor equations are no longer valid, in favor of quantum transport treatments [93]. In OLEDs, a typical device thickness is roughly 100nm and is composed of several individual organic layers. However, organic materials exhibit strong electronic localization and, therefore, have mean free path on the order of molecular spacing [65,66]. Under such conditions, where a number of scattering events occur during carrier transit, the use of the semiconductor equations for OLED transport is asserted. Another important consideration is that the semiconductor equations were originally developed for extended state, crystalline inorganic materials; however, in many cases, using an experimental mobility has shown to yield good results [76]. That is, as stated previously, a number of experimental techniques have been used to determine mobility over a range of conditions. It is then common to empirically fit the mobility over a broader range of conditions using the Poole-Frankel mechanism, which is mathematically described below:

$$\mu_n(E) = \mu_0 \exp\left(-\frac{\Delta}{kT}\right) \exp(\gamma\sqrt{E}) \quad 3.3$$

$$\gamma = \beta \left(\frac{1}{kT} - \frac{1}{kT_0} \right) \quad 3.4$$

where μ_n is the electron Poole-Frankel mobility, μ_0 is the temperature independent electron mobility, Δ is an activation energy, β and T_0 are empirical terms used to set the electric field functional dependence of γ [94,95,96]. The semiconductor equations consist of the drift-diffusion equations coupled with the Poisson equation.

The Poisson equation is one of Maxwell's equations and is a cornerstone of electromagnetic (E&M) theory [97,98]. It is an expression of how the electric potential in a dielectric medium is directly affected by space charge and the permittivity of the material (a measure of the ability of a material to polarize or, also, a measure of the material's resistance to formation of an electric field) and is written as:

$$\nabla^2 \phi = -\nabla \cdot \mathbf{E} = -\frac{q}{\varepsilon} (p - n + N_A^- - N_D^+ + p_t - n_t) \quad 3.5$$

where ϕ is scalar potential, \mathbf{E} is the vector electric field, q is electron charge, ε is permittivity, $n(p)$ is the electron(hole) carrier concentrations, $n_t(p_t)$ is the concentration of filled electron(hole) trap states and $N_D^+(N_A^-)$ is the ionized donor(acceptor) concentration. As described in the above equation, the vector electric field is equivalent to the negative gradient of the electric potential. Thus, the net carrier concentration, or space charge, is in intimate coupling with the electric field. The implications of this coupling lead to current limits of the semiconductor equations and will be further discussed in [Section 3.4.1](#).

In many OLED structures, which utilize an undoped heterojunction, the donor and acceptor

carrier concentrations may be neglected in Equation 3.5 above. Further, the trap concentrations in the above equation correspond to extrinsic trapping (e.g., O^{2-} trapping states in Alq_3 [99,100]) within the organic material. In literature, deposition in inert environments and use of zone refinement for material purification can greatly minimize trapping states [99]. Under such conditions, where both donors/acceptors and trapping centers can be neglected, the Poisson equation may be reduced to the following equation:

$$\nabla^2\phi = -\nabla \cdot \mathbf{E} = -\frac{q}{\varepsilon}(p - n) \quad 3.6$$

Next, the drift-diffusion equations are considered. These equations arise from higher-order moment of the Boltzmann transport equation. This framework utilizes a phase-space formulation (a generalized transport description including position and momentum coordinates) of the constituent charge transfer processes including carrier scattering [93,101]. The Boltzmann transport equation represents a general description of particle motion, which produces an integro-differential equation yielding the position-time relationship of particle motion dependent on acceleration forces and instantaneous particle position. Several simplifications including the relaxation-time approximation are made to reduce the complexity of the equations down to a set of coupled partial differential equation (see Appendix A for further information on the development of the continuum semiconductor equations). Also the Fermi-Dirac statistics are replaced with Maxwell-Boltzmann statistics since undoped organic semiconductors are non-degenerate [55,56,93]. The namesake, drift-diffusion equations, refers to the two separate, phenomenological mechanisms contributing to transport. The drift mechanism is the Coulombic response of the carrier to the local electric field and the surrounding physical medium (effective carrier mobility) [93,101]. The diffusion mechanism is the carrier response to the local carrier concentration gradient brought about by thermal excitement and, again, the surrounding physical medium (effective carrier mobility) [55,56]. The drift-diffusion equations, which describe the carrier transport in the organic medium, are presented below:

$$\mathbf{J}_n = \mathbf{J}_{n,drift} + \mathbf{J}_{n,diff} = q\mu_n n\mathbf{E} + kT\mu_n \nabla n \quad 3.7$$

$$\mathbf{J}_p = \mathbf{J}_{p,drift} + \mathbf{J}_{p,diff} = q\mu_p p\mathbf{E} - kT\mu_p \nabla p \quad 3.8$$

where $\mathbf{J}_n(\mathbf{J}_p)$ represents the vector, total electron(hole) current density and the additional subscript *drift(diff)* refers to the drift(diffusion) current contribution. Additionally, $\mu_n(\mu_p)$ is the electron(hole) mobility, k is the Boltzmann constant and T is temperature.

Next, through incorporation of the drift-diffusion equations in a continuum treatment the transient carrier continuity equations may be found [93,101], as shown below:

$$\frac{\partial n}{\partial t} - \frac{1}{q} \nabla \cdot \mathbf{J}_n = G - R \quad 3.9$$

$$\frac{\partial p}{\partial t} + \frac{1}{q} \nabla \cdot \mathbf{J}_p = G - R \quad 3.10$$

where G is the carrier generation and R is carrier recombination. In OLED devices, the carrier generation term, G , is assumed to be negligible since few carriers are thermally generated in large band gap organic materials. The mechanism which controls the recombination rate term, R , occurs via a free-charge-carrier Langevin process [89]. That is, in low mobility materials, the recombination process is rate limited by charges finding each other. Recombination then occurs in cases where counter-charges enter a collision cross-section determined by the thermal-energy-reduced potential well formed by the counter-charge Coulombic attraction. Further, when in-transit counter-charges enter spatial proximity where the escape energy exceeds the recombination attraction energy, recombination is statistically favored to occur. Overall, the macroscopic phenomenon is described as diffusion limited which is proportionality to electron and hole carrier concentrations and the maximum carrier mobility [102]. The recombination rate is then expressed below:

$$R = \frac{q}{\varepsilon} \mu_{max} np \quad 3.11$$

where μ_{max} is the maximum of the two charge carrier mobilities.

Finally, the semiconductor equations possess the ability to couple the carrier injection mechanism and thus present a self-consistent set of equations that may be solved to determine the physical parameters of the device operation.

3.2.3 Master Equation

An attempt to regain injection and transport mechanism control was made in the work of Tutis et. al. [81]. Arguing that many of the features of transport in organic materials are not compatible with the classical continuum model, a model based on the Master equation was developed. In addition, this model allows grid point discretization at molecular spacing distances which reinforce the discrete potential environment felt by individual molecules. The governing equations are similar in representation to those of the semiconductor equations.

The related Poisson equation describes the site energy environment at point x as an expansion of the potential influences from the grid points, x_m , as follows [81]:

$$\bar{E}_{HOMO}(x) = E_0 + E_{IF} + \sum_m E(x_m, x) \quad 3.12$$

where $\bar{E}_{HOMO}(x)$ is the HOMO energy level at the site, E_0 is the zero-energy level, E_{IF} is the image force energy, and $E(x_m, x)$ is the polarization contribution of nearby molecules at point x_m . Furthermore, Equation 3.12 represents the local energy at site x .

The transport equations apply similar implementations of rules as Monte Carlo simulations. The basic equations are common to the continuum formulations, and are shown below [81]:

$$\frac{dn_i}{dt} = \left(\frac{dn_i}{dt}\right)_{inj} + \left(\frac{dn_i}{dt}\right)_{hop} + \left(\frac{dn_i}{dt}\right)_{rec} \quad 3.13$$

$$\frac{dp_i}{dt} = \left(\frac{dp_i}{dt}\right)_{inj} + \left(\frac{dp_i}{dt}\right)_{hop} + \left(\frac{dp_i}{dt}\right)_{rec} \quad 3.14$$

where the carrier time derivatives are separated into the three mechanisms of injection, transport (localized hopping) and recombination. Again, in essence, the carrier time rates are effectively discretized forms of semiconductor mechanism components. Also, as will be seen shortly, the mathematical form of Equations 3.13-3.14 follows similar construction as the continuum-based drift-diffusion framework. A major difference compared with other numerical models is that the objective of the Master equation is to determine occupancy factor. The carrier occupancy factor, f_i , for either carrier can then be found from the Master equation, which is written below [81,90]:

$$\frac{\partial}{\partial t} f_i(t) = - \sum_{j \neq i} v_{ji} f_i(t) [1 - f_i(t)] + \sum_{j \neq i} v_{ij} f_j(t) [1 - f_i(t)] - \lambda_i f_i(t) \quad 3.15$$

where the v_{ij} is the Miller-Abrahams site-to-site hopping rate for the carrier and λ_i is the carrier decay rate for the excitation. Steady-state results may be found as the transient terms decay. In many cases, the terms in Equation 3.15 can be simplified and/or linearized to assist numerical evaluation [90]. Further, the electron occupancy factor, $f_{n,i}$, may be used to determine quasi-Fermi level following Fermi-Dirac statistics and is shown as follows:

$$f_{n,i} = \frac{1}{1 + \exp\left(\frac{E_{LUMO,i} - F_{n,i}}{kT}\right)} \quad 3.16$$

where $E_{LUMO,i}$ is and $F_{n,i}$ is the electron quasi-Fermi level and the local HOMO/LUMO energy band is determined from Equation 3.12 [55,56]. In cases where the non-degeneracy assumption is made, the following relation may be used:

$$f_{n,i} \approx \exp\left(-\frac{E_{LUMO,i} - F_{n,i}}{kT}\right) \quad 3.17$$

As with the semiconductor equations, this numerical technique permits physical coupling to the injection mechanism and, therefore, is more useful to the device level than the previously discussed Bässler simulation. In particular, with knowledge of the Fermi level of the metal and knowledge of the occupancy of the organic in contact with the metal, an equilibrium condition may be found [81].

The Master Equation has attracted recent interest within organic materials due to its ability to incorporate partially continuum-derived and statistical (non-linear and non-local) methods to treat device transport considerations. In this method, regions of space are discretized to

approximate charge density evolution at a particular molecular site with time. The set up allows large amounts of flexibility including the ability to formulate charge transport in terms of Coulombic interaction of in the sites neighboring charges. Another beneficial feature is the ability to more accurately model the image potential that arises from injected charges at an interface. Moreover, the broad flexibility of this method has proven useful in a number of interesting studies [103]. However, as remarked by Yampolskii, *et. al.* [104]: “...this model involves a range of artifacts such as tunneling factors, effective attempt frequency, *etc.* In spite of good agreement with experiments, this numerical tool is very complicated.” Furthermore, this technique will not be considered due to the number of factors which may lead to a variety of conflicting results.

3.3 Carrier Injection Mechanism

Semi-classically, two distinct injection mechanisms were considered. These mechanisms were thermionic injection [105] and tunneling (field) injection [106] (Figure 3.3). From a physical perspective, the most important feature of the injection process is the occupancy of states at the neighboring metal-organic (M-O) interface, which leads to the formation of an injection barrier. Therefore, the discussion of physics barrier formation is discussed. Common M-O injection models are then discussed which incorporate physical features of the injection mechanism.

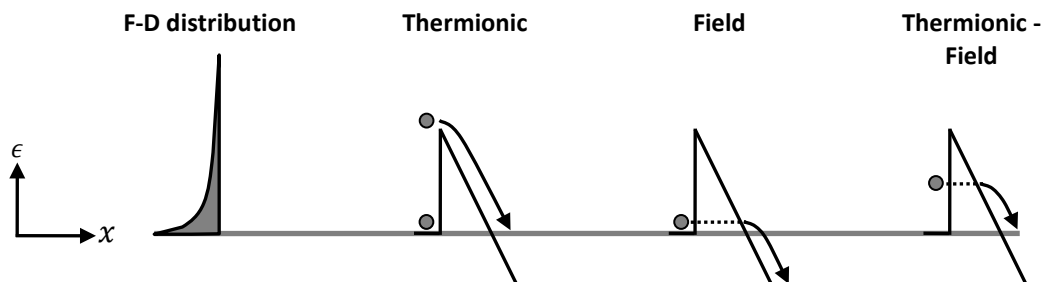


Figure 3.3: Common injection mechanisms. Diagrams from left to right: Fermi-Dirac (F-D) distribution function describing the thermally excited electron population. Thermionic injection occurs when electrons are thermally excited over the injection barrier. Field injection occurs when charges tunnel through the injection barrier. Thermionic-field injection occurs when electrons are thermally excited but not enough to surmount the injection barrier and subsequently tunnel through a narrower tunneling barrier.

3.3.1 Barrier Formation

In many cases, inorganic semiconductor-metal surfaces are pinned due to the presence of high densities of interface states. Band bending within the inorganic semiconductor then occurs in order to produce charge neutrality within the semiconducting layer (in essence a mobile carrier depletion region is formed which enforces charge neutrality) [56]. On the other hand, organic materials have the potential to form clean interfaces, and, thereby experience different interface formation than inorganic material interfaces (e.g., Au/CuPC [107]). However, in a

more general sense, other issues tend to control surface electronic structure. An early review by Ishii suggested a number potential causes for this effect including surface charge transfer, surface roughness (polarization related), surface chemical reaction, interfacial states and surface dipole [108]. This finding has led to a variety of theories regarding the theory metal-organic barrier. Though a large number of important studies exist, this is still a developing field [107-112]. A number of commonly described physical properties of the metal-organic interface are described in the following sections.

3.3.1.1 Interfacial dipole

To a first order approximation, the injection barrier height at a common metal-organic semiconductor is equal to the energetic difference between Fermi energy level of the metal and the appropriate injecting semiconductor energy level into which the injecting charge is injected. This condition is referred to as the Mott-Schottky limit (Figure 3.4, Figure 3.5). The electron(hole) barrier height $\Phi_{Bn}(\Phi_{Bp})$ may then be determined from the following individual electronic properties of the metal and organic materials, as follows:

$$\Phi_{Bn} = \phi_M - \chi \quad 3.18$$

$$\Phi_{Bp} = I_p - \phi_M \quad 3.19$$

where ϕ_M is the work function of the metal, χ is the electron affinity of the adjacent organic layer and I_p is the ionization potential of the adjacent organic layer (see Figure 3.4).

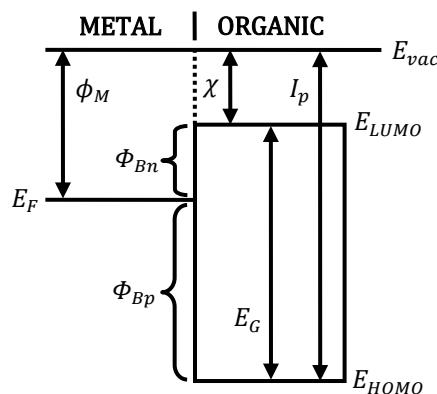


Figure 3.4: Energy levels at a metal-organic semiconductor interface abiding by the Mott-Schottky limit. Energy levels: E_{vac} , vacuum level; E_{LUMO} , organic LUMO energy level; E_{HOMO} , organic HOMO energy level; E_F , metal Fermi energy level. Energy differences: Φ_{Bn} , metal-organic electron injection barrier; Φ_{Bp} , metal-organic hole injection barrier; ϕ_M , metal work function (metal-vacuum); χ , organic electron affinity (LUMO-vacuum); I_p , organic ionization potential (HOMO-vacuum); E_G , organic band gap (LUMO-HOMO).

Early work on metal-organic interface barrier height adjustment focused on utilizing ultraviolet photoemission spectroscopy (UPS) to probe the HOMO DOS and thereby reveal how

the barrier height at a metal-organic interface shifts as monolayers of organic thin film are deposited. In practice, these experiments are accomplished through use of molecular beam epitaxy (MBE). With the use of photoemission spectroscopy and Kelvin probe techniques, the highest occupied molecular orbital (HOMO) level can be mapped. Through inverse photoelectron spectroscopy or use of the optical band gap, the lowest occupied molecular orbital (LUMO) may be attained [107-112].

Using these two methods it has been shown that the measured value of the barrier height in fact differs substantially from the expected bulk value. In recent years many experiments from research groups around the world have shown through experimentation (most notably, photoelectron spectroscopy) that bulk interface formation is oversimplified. The common interpretation is that an interface dipole is caused by differences in the bulk-level alignment occurring at the metal-organic interface (Figure 3.5). The interface-dipole-augmented equations are:

$$\Phi_{Bn} = \phi_M - \chi + \Delta \quad 3.20$$

$$\Phi_{Bp} = I_p - \phi_M - \Delta \quad 3.21$$

where Δ is the interfacial dipole height. The dipole size depends on the strength of the surface reaction. A number of review articles have focused on understanding what factors and parameters affect the magnitude of the interfacial dipole [107-112]. The interface dipole interpretation is widely accepted; however, the mechanism(s) behind interface barrier formation are not yet fully understood.

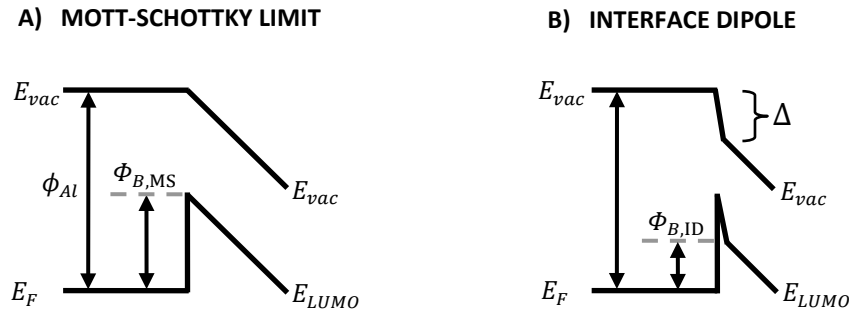


Figure 3.5: Metal-organic (M-O) band diagrams for electron injection. A) Formation of an M-O barrier abiding by Mott-Schottky limit; barrier height is $\Phi_{B,MS}$. B) Formation of an M-O including an interface dipole; barrier height is $\Phi_{B,ID}$.

Finally, it should be further remarked that in device current models it is typical that the barrier heights are typically taken as either bulk level values or from methods indicated above such as UPS. However, a warning should be issued when using measured barrier heights as they tend to vary widely depending on preparation, processing and materials, amongst other factors. In closing, the injection barrier is a crucial parameter which strongly influences device performance. In closing, the injection barrier height is a crucial parameter which strongly

influences device performance. The barrier height parameter will again be discussed in the context of the current limiting cases later in this chapter.

3.3.1.2 Image potential

An image charge is formed as a result of the injection of an electron or hole into the organic layer. Due to the ability of metal to rapidly form electric fields after ejection of an electron or hole from the metal surface, a Coulombic force-at-a-distance acts to return the ejected charge to the metal surface (Figure 3.6); this process is referred to as interface recombination. The interface dipole effect modifies the energy level structure of the organic semiconductor at the interface, as a result of the potential energy reduction due to the image effect, as shown below in Figure 3.6. The variation in potential energy, V_{im} , resulting from the injected charge into the organic material is expressed below:

$$V_{im} = -\frac{q}{4\pi\epsilon x} \quad 3.22$$

where x is the distance from the interface.

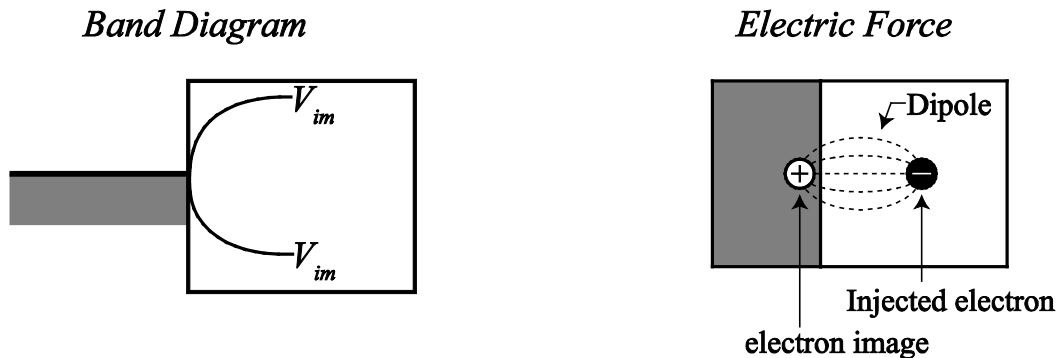


Figure 3.6: At left, an energy diagram showing the injection potential barrier formed by the image Coulombic reaction. At right, the formation of an electric dipole between an injected electron and its image at a metal-organic interface.

3.3.2 Thermionic Injection

Thermionic injection results from thermal smearing of carrier population at both metal-organic interfaces. Due to the existence of thermally excited states (thermal energy $\sim kT$), and according to Fermi-Dirac statistics, a fraction of charges are expected to surmount the potential barrier and be injected into the adjacent medium (Figure 3.3) [70]. This section will briefly discuss the historical developments of this mechanism with application for metal-organic (M-O) injecting contacts.

3.3.2.1 Richardson theory

Historically, thermionic injection theory was of practical importance for emission of

electrons into nearly free space under the application of a heated metallic electrode and was of interest for a variety of applications, for example filaments used in incandescent light bulbs. This theory was originally developed by Richardson in the early 1900s [105]. Due to the relation to thermal smearing and the Fermi-Dirac surface carrier populations, the injection level is based on the height of the injection barrier and the temperature of the injecting electrode. The thermionic injection current density, J_R , is expressed as:

$$J_R = A^* T^2 \exp\left(-\frac{\Phi_B}{kT}\right) \quad 3.23$$

where, A^* is Richardson's constant and T is temperature. The energy barrier, Φ_B , is the energy required for an electron to escape from the metal's surface to vacuum space. In metals, this property is referred to as the metal's work function, ϕ_M .

3.3.2.2 Schottky theory

As semiconductor technology rose to prominence, arguments were made which modified Richardson theory for compatibility with metal-semiconductor rectifying junctions [113]. In particular, the theory was applied for the reverse-biased metal-(n-type) semiconductor junction. The primary difference which exists between injection into free space and into a semiconductor is the energy-level restrictions on the injected carrier. When an electron is injected into free space, it may take on a continuous range of energies; however, when an electron enters a semiconductor, it must take on specific energy levels confined to localized positions. As such, arguments were made which render the delocalized treatment of carriers within high mobility inorganic crystals applicable [55]. In effect the barrier height term in Equation 3.23 is replaced by appropriate injection barrier, for example for the electron case, between the Fermi level of the metal and the electron affinity (for the Mott-Schottky barrier case) (see Figure 3.8).

In addition, due to the small length scales employed in semiconductor devices, the presence of a constant electric field, E , throughout the device modifies the potential environment throughout the semiconductor device by:

$$V_E(x) = qEx \quad 3.24$$

where V_E expresses the electric field contribution to the potential within the device and x is, again, the distance from the planar electrode-semiconductor interface. From an energy diagram perspective, this is the well-known band bending that occurs from application of an electric field over a device (Figure 3.1, Figure 3.7). The overall potential, V_{tot} , is then described by the following expression:

$$V_{tot} = -q\Phi_B - qE_s x - \frac{q^2}{16\pi\epsilon x} \quad 3.25$$

where the right-hand-side terms, respectively, are related to the injection barrier height term, the Schottky barrier lowering term and the image potential (Figure 3.7). Moreover, it can then

be shown from Equation 3.25 that the energy barrier minimum is lowered in the presence of a surface electric field, E_s . The barrier lowering is referred to as Schottky barrier lowering, $\Delta\Phi$, and can be shown to have the following expression:

$$\Delta\Phi_B = \sqrt{\frac{q E_s}{4 \pi \epsilon}} \quad 3.26$$

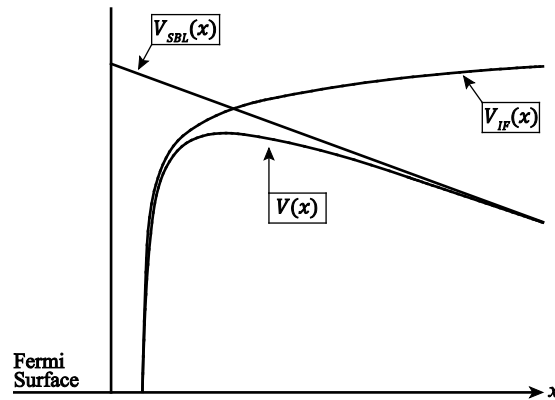


Figure 3.7: Total potential, $V(x)$, within the semiconductor including components of Schottky barrier lowering (SBL), image force (IF) and injection barrier (Equation 3.25). Modified from [75,66,134].

The substitution of the SBL term (Equation 3.26) into the Richardson thermionic injection equation (Equation 3.23) is the Richardson-Schottky (RS) thermionic injection equation and is presented below:

$$J_{RS} = A^* T^2 \exp\left(-\frac{\Phi_B - \Delta\Phi_B}{kT}\right) \quad 3.27$$

The succession of thermionic injection mechanisms, which are explained above are shown below in Figure 3.8.

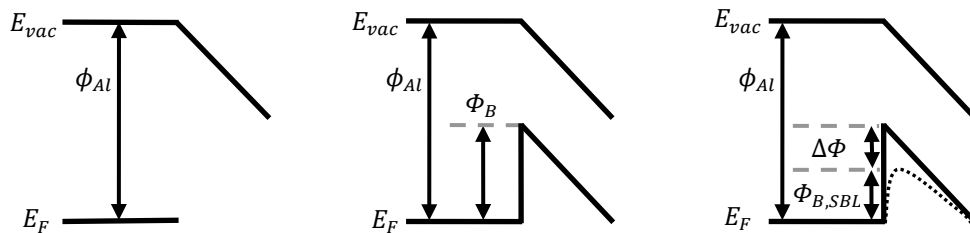


Figure 3.8: Progression of thermionic injection models for use in inorganic semiconductors. At left, thermionic injection from metal to vacuum (discharge tube); at middle, thermionic injection into conduction band of inorganic semiconductor (Mott-Schottky limit); at right, thermionic injection into conduction band of inorganic semiconductor including Schottky Barrier Lowering effect (dashed line).

3.3.2.3 Los Alamos Group Model

The Schottky model introduced above does not account for charges which are injected into the M-O interfacial region but then fail to be successfully injected into the semiconductor bulk. That is until now we have only considered the gross number of injected charges, whereas the net charge injection is the true value we seek to determine. In OLEDs, the vast majority of charge carriers that are injected from the electrode do not incur scattering events and ultimately succumb to the influence of the surface image force surface leading to interface recombination. A commonly used and cited model in literature is the effective recombination velocity model, originally used by Davids, et. al. [114]. This model led to the first comprehensive OLED electrical system model. In this work, Davids [114] proposed the magnitude of the phenomenological surface recombination current, J_{ir} , shown below:

$$J_{ir} = \frac{A^* T^2}{n_0} n_{surf} \quad 3.28$$

where n_0 is the intrinsic carrier concentration of the particular organic semiconductor and n_{surf} is the surface carrier concentration of the injected species (this remains coupled to the carrier concentration equation system). In this work, a self-consistent solution of the semiconductor equations was implemented for a series of single-layer PLEDs and provided an initial numerical framework for a full OLED continuum current model. In essence, the interfacial recombination velocity makes the argument that the number of charges which recombine at the surface is related to the number of charges present at the injecting surface.

3.3.2.4 Scott-Malliaras theory

Highlighting the lack of a physical rationale for Equation 3.28, particularly the lack of freely propagating charges in LUMO/HOMO levels within organic materials, Scott and Malliaras [115] revisited a more general injection treatment for low mobility carriers formulated in the 1970s [116] (more information in Appendix A.2). Accordingly, this theory makes the argument that, for low mobility injecting materials where many of the injected charges return to the injecting electrode, a diffusion-controlled surface recombination (or Langevin) process results. This condition is justified for the M-O interface because typical mean free paths of carrier hopping

are on the order of the molecular spacing resulting in strong carrier localization. Interestingly, the effective injection proportionality closely resembles that of Schottky-type injection with the exception that additional factors of the surface electric field and carrier mobility must now be included. The net injection current density given by the Scott-Malliaras (SM) injection theory, J_{SM} , may be evaluated through the following set of equations [115]:

$$J_{SM} = 4\psi^2 N q \mu E_S \exp\left(-\frac{\Phi_{B,0}}{kT}\right) \exp(f^{1/2}) \quad 3.29$$

$$\psi(f) = f^{-1} + f^{-1/2} - f^{-1}(1 + 2\sqrt{f})^{1/2} \quad 3.30$$

$$f = \frac{qE_S r_c}{k_B T} \quad 3.31$$

$$r_c = \frac{q^2}{4\pi\epsilon kT} \quad 3.32$$

where E_S is the surface electric field, r_c is the Coulomb radius of the image pair (this value represents the radius at which the charge carrier separation is statistically favored through thermal means). f is a non-dimensional, reduced electric field. Another important result from this mode is that the surface carrier concentration, n_s , may be found to be:

$$n_s = 4\psi^2 N_0 \exp(-\Phi_B) \exp f^{1/2} \quad 3.33$$

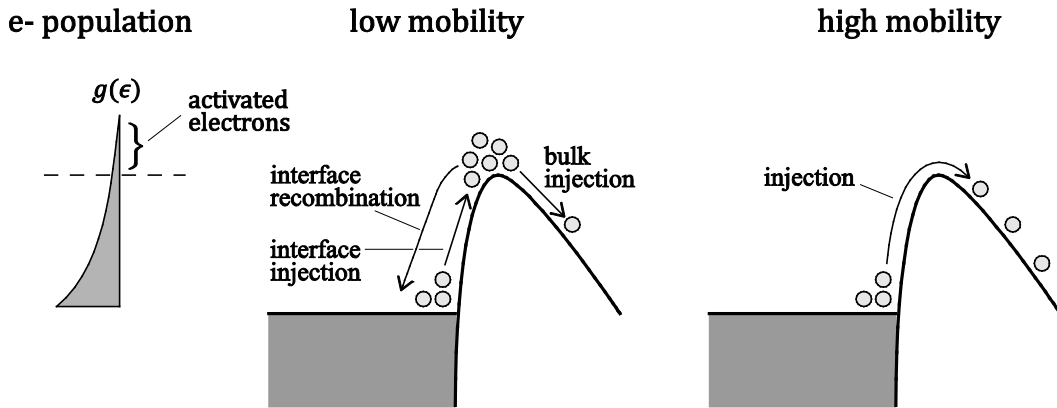


Figure 3.9: Common injection interpretation for activated electrons. At left, electron (e-) population showing fraction of activated electrons. At middle, injection into low mobility materials, interface recombination reduces aggregate number of activated electrons being injected into bulk (bulk injection). At right, nearly all activated electrons enter the bulk. Adapted from [161].

The SM current model bears a strong resemblance to the Langevin bimolecular recombination form used for carrier recombination (formation of excitons) in OLEDs. In both mechanisms diffusive mechanisms are considered to mediate carrier motion. This occurs in regions where high carrier densities exist. The Coulombic attraction of carrier pairs dictates the energy environment of the carrier. When charges approach a counter-charge within the Coulomb radius they, on average, recombine. It may, therefore, be concluded that the SM injection model is a field-enhanced diffusion mechanism. Finally, it is concluded, that the Scott-Malliaras mechanism is the most appropriate thermionic injection for metal-organic interfaces and will be included in the current calculation component of this work.

3.3.3 Tunneling injection

Early literature focused on considering tunneling injection as the primary injection mechanism [129,130,132]. Parker et. al. [131] showed good comparison between electron- and hole- only devices based on bulk energy level values. In recent years, however, many authors have debated the contribution of tunneling injection. An important consideration when determining the applicability of tunneling is the magnitude of the electric field present at the interface. Tunneling injection becomes increasingly important at higher electric fields (typically >1 MV/cm). In fact, early devices possessed considerably lower current efficiency than modern devices and required higher driving fields. Early work suggested that as the tunneling distance approached 1nm, or as fields begin to exceed about 1.2 MV/cm (assuming for organics, $\epsilon_{rel} = 3$), the tunneling injection current begins to exceed thermionic injection current. However, at lower applied fields, field injection effect is expected to be less than or on the same order as the thermionic injection component and, hence, may be ignored. The field injection theory has more recently fallen out of favor following the Monte Carlo simulations of Barth and others [133-136] whose detailed study concluded that any similarity between field injection theory and experiment "... must be considered accidental." Baldo and colleagues [137,138] argued that tunneling can also be neglected due to its inconsistent barrier heights over a variety of temperature conditions. This follows the assumption that tunneling should have no temperature dependence. Further, in the context of this work, the field effect will be neglected for the reasons stated above; that is, the field dependence on injection does not dominate current injection until higher electric fields are present. Such fields are not expected to be present in our lab-grade devices and as such field injection will not be further considered. The modified FN tunneling equations are displayed below for convenience. Many variants of this equation for different barrier types have been investigated in the literature (see [139] for examples). In the event the tunneling current, J_{tun} , is deemed non-negligible, the tunneling current may be found from the following equations:

$$J_{tun} = \frac{CE_s}{\Phi_B} \exp\left(-\frac{B\Phi_B^{3/2}}{E}\right) \quad 3.34$$

$$C = \frac{2.2q^3}{8\pi h} \quad 3.35$$

$$B = \frac{8\pi\sqrt{2m^*}}{2.96hq} \quad 3.36$$

where B and C are dimensional constants, E is the surface electric field, Φ_B is the barrier height, h is Planck's constant and m^* is the effective mass of the injected charge carrier in the semiconducting medium.

Original depictions of the injection mechanism showed that at high electric field a tunneling mechanism can be well shown to approximate the injection current relationship. In that period it was widely assumed that the Schottky-Richardson equation can be used to well approximate the injection mechanism. Further analysis through the use of Monte Carlo simulations by Arkhipov and others in a multiple author study tended to find that the tunneling injection model used previously fit only by accident.

3.3.4 Interface broadening model

Baldo and colleagues have written several articles on the energetic broadening of surface states forming an interfacial pocket which governs injection rate [137,138]. Within this work it is argued that the interface broadening effect leads to the high-field power law observed in operational devices, which have previously been identified as trap-charge-limited (TCL) current in literature [100]. Further, the work states that previous works assuming should be reconsidered to be injection limited (IL) subject to the energetic broadening model [138]. The interface broadening model is validated with single-carrier experimental devices having a variety of different injecting materials and focuses specifically on the archetypical electron-transporting/emitting material, Alq3. This is a frequently used, lab-grade small molecule in the fact that it has a large permanent dipole moment. The dipole moment contributes to the energetic disorder of the material and effectively increases the width of the Gaussian DOS of the LUMO level which electrons are injected to at the cathode. The work concludes that both RS thermionic (Equation 3.27) and FN field injection (Equations 3.34-3.36) models fail to express barrier height dependence at low temperatures and, therefore, are not equipped to approximate current injection over a wide range of operating conditions. A very detailed treatment and substantial evidence to the effect of the interface broadening theory and elaborates on the conditions where traditionally considered injection mechanisms fail [137,138]. These works, unfortunately, does not address the ability of the SM injection theory to predict the appropriate dependence (Equations 3.29-3.32). However, the results of this work require empirical curve fits and do not appear to permit the potential for excessively rough surfaces considered in this work. It would appear very likely that the arguments of this work on the energetic disorder may be modeled as a modified barrier height and are nominally constant provided the devices are maintained within a reasonable constant temperature environment. Finally, this model will not be incorporated in the physical treatment.

3.4 Current Limiting Cases

Numerical techniques for solving the multi-dimensional semiconductor equations for MOSFET applications have existed and been improved over many decades [117-118]. A number of papers have extended the numerical solution techniques to the OLED-specific semiconductor equations [114,119,120]. However, solutions to the set of equations for multi-dimensional OLEDs have not been attempted beyond planar models using Master equation and Monte Carlo

methods [103,104]. In fact, the essence of the following two chapters is to extend the treatments of the multi-dimensional semiconductor equations to the injection limited and space-charge limited regimes. A major difference in the device physics of OLEDs is related to their low intrinsic carrier concentrations, which complicates the boundary conditions of the carrier concentration systems. This situation inhibits simple solution, specifically in cases where injection doping is not utilized. Further, this requires the system of equations to self-consistently resolve the Poisson equation's strong coupling to the carrier equations. Due to the complexity of full-blown solution techniques, the ohmic injection assumption is commonly made in literature to simplify the current regime analysis. In such cases, experimental curve fits are made to determine the mobility following the SCL current relations. In short, simplified limits of the current equations are frequently cited. However, in general, this treatment leads to a poor understanding of the overall physics behind the equations, which perhaps explains the lengthy debate in literature over whether devices are injection or space-charge limited. The discussion on whether the device current is OLEDs is controlled by the contact (injection limited) or the bulk (space-charge limited) has been a central consideration of literature. Individual consideration should be given to each device. The important factors, which influence the device current flow, include device preparation, the material(s) and deposition process(es) (e.g., neat films versus co-evaporation or molecular doping) and the device structure of the OLED.

As depicted in Figure 3.10, the height of the injection barrier is the main factor which controls the ability of the device to produce (quasi-)ohmic injection. Recall that according to the SM injection mechanism, the injection current (Equation 3.29) and the surface carrier concentration (Equation 3.33) both scale with the exponential of the barrier height. Thus, the barrier height governs the ability of metal-organic interfaces to supply sufficient charges to the bulk to produce electric field redistribution as space-charge limited current (SCL). A more detailed discussion of the effects of the injection barrier on the semiconductor equations will be discussed in the next section.

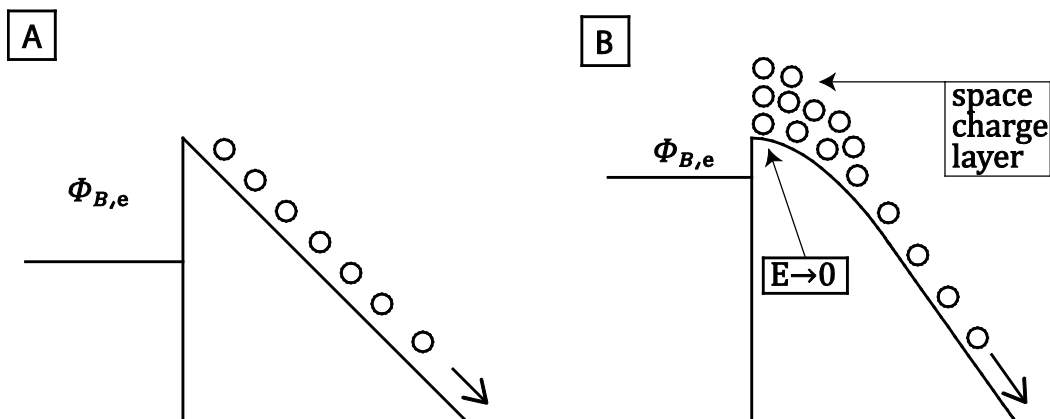


Figure 3.10: Carrier injection for (A) injection-limited contact and (B) ohmic contact. In (A), the barrier height, $\Phi_{B,e}$ and produces a Schottky contact; in (B), the $\Phi_{B,e}$ is small and the large carrier injection leads to carrier accumulation which in term leads to electric field redistribution.

As a result of the injection barrier, a number of current regimes exist. A classical text and a number of literature sources highlight and explain the common $J - V$ trends in OLED devices (Figure 3.11) [66,77]. The rationale and precursory quantitative theory behind the transitions will be explained in the following sections.

3.4.1 Bulk Limit Regime

Over the range of applied voltage for a single-layer device encountering ohmic injection at at least one contact, the bulk limited regime itself transitions through a number of different regimes depending on the electronic structure of the organic layer (Figure 3.11). A number of references explain this regime [66,77].

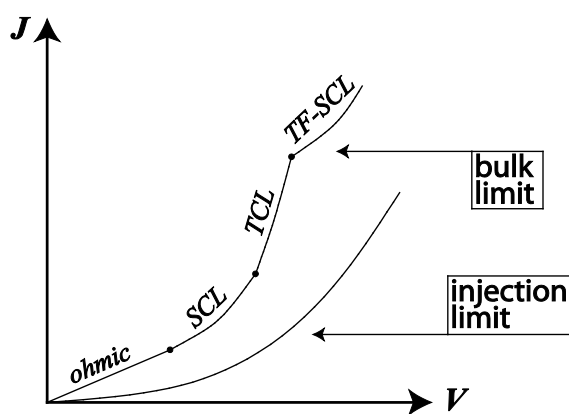


Figure 3.11: Current-Voltage (IV) relationships for single-carrier TCL and IL conditions. At left, injection limited (IL) regime. At right, trap-charge limited regime (TCL), which goes trends through the following regimes as voltage increases: ohmic, space-charge limited (SCL), trap-charge limited (TCL) and trap-free space-charge limited (TF-SCL). Modified from [66].

3.4.1.1 Ohmic Regime

In Figure 3.10, it is shown that the requirement for reaching the space-charge limited current regime is that the injection is ohmic. In other words, the amount of charges injected to the M-O interfacial region is sufficient to supply the bulk with as many charges as can be supported; therefore, the ability to transport the charges becomes the current limiting factor. In the low applied field limit, the bulk is capable of transporting the charges through the bulk. This regime is specific to the case where the number of charges is less than the intrinsic charges from an equivalent capacitor, with intrinsic capacitance, C_0 , of the organic layer:

$$C_0 = \frac{\epsilon}{L} \quad 3.37$$

where, ϵ , is the permittivity of the specific organic layer ($= \epsilon_{rel} \cdot \epsilon_0$). The number of transported charges may then be computed again from an equivalent capacitor charge, Q_0 ,

model as follows:

$$Q_0 = C_0V \quad 3.38$$

where V is the applied voltage over the capacitor. In this regime, the bulk is capable of sustaining current flow and the current is said to be in the ohmic regime. When assuming constant mobility, drift current model, the current resulting density, J_{ohmic} , is linear and is related to the following equation:

$$J_{ohmic} = q\mu n_i E \quad 3.39$$

where V is applied voltage and L is organic layer thickness. Ultimately, as the voltage is ramped, and the number of charges injected begins to exceed the intrinsic charge concentration in the organic bulk, the bulk limits current flow.

3.4.1.2 Space-Charge Limit

The physical understanding of space-charge effects in vacuum tubes dates back to the early-1900s [105]. Treatment of the space-charge effects in dielectric materials traces back to 1940 [121]. This theory was furthered and adapted throughout the years following its initial formulation to include discrete and continuous trapping effects [77,122,123,124]. Space-charge limited (SCL) current theory is a complication arising from the coupling effects of semiconductor charge injection (Equations 3.29-3.32), charge transport (Equations 3.9-3.10) and charge neutralization (Equation 3.6). This condition is specific to low mobility materials with high carrier injection levels. In the following example consider two electrodes separated by a distance, L , with only single carrier flow and a strong injection level at one electrode. The SCL current results from the necessity for injected charge carriers to be neutralized, via recombination, within or extracted from a material within a time scale on the order of the dielectric relaxation time, τ_d , from their injection [77,66,123,125]. The material dielectric relaxation time is shown below:

$$\tau_{d,n(p)} = \frac{\sigma_{n(p)}}{\varepsilon} \quad 3.40$$

where $\sigma_{n(p)}$ is the electron(hole) conductivity of the carrier causing the SCL effect. The following relation can be used to determine, e.g., the electron conductivity:

$$\sigma_n = q\mu_n n \quad 3.41$$

where, above, the electron conductivity is considered. The hole conductivity may be determined in an analogous fashion. Additionally, the drift mechanism, which is the primary charge conduction mechanism under large electric fields has an electron(hole) drift time scale, $t_{drift,n(p)}$, shown below:

$$t_{drift,n} = \frac{L^2}{\mu_n V} \quad 3.42$$

where L is the material thickness and V is the applied voltage over the slab. The drift time represents the amount of time that it takes a carrier species to drift to across the material slab after injection. To restate, it is the dynamic coupling effect of the charge neutralization and the drift current mechanism that prompts space-charge accumulation and electric-field redistribution within the material. The criterion for space-charge limited current are two-fold including (i) that the carrier drift time is reduced to below the dielectric time and (ii) that a sufficiently high level of carrier injection exists [125]. It follows from these conditions that a high density of excess charges are not recombined by the time they have reached the counter-electrode. Furthermore, the inefficient removal of charges from the material leads to space-charge accumulation. Large space-charge regions produce electric field screening effects, through coupling to the Poisson equation, and thus the electric field is redistributed.

Moreover, SCL theory predicts a hard limit on the current density of a material exhibiting single-carrier current. This leads to the classical Mott-Gurney current limit [121], which is expressed below:

$$J_{MG} = \frac{9}{8} \epsilon \mu \frac{V^2}{L^3} \quad 3.43$$

where J_{MG} is the Mott-Gurney space-charge limited current, μ is the mobility of the single-injected carrier, V is the applied voltage and L is the organic layer thickness for a planar device. It should be noted that this theory is analogous to Child-Langmuir equation for vacuum space [77].

3.4.1.3 Trap-Charge Limit

Trap-charge limited (TCL) current theory is a special condition of the SCL current theory. In fact, for a localized set of trap states, TCL current regions are bounded by SCL regions (Figure 3.11). That is, SCL current occurs at applied voltages lower than the TCL region and TF-SCL (trap-free SCL) current occurs at applied voltages higher than the TCL region. Unfortunately, the $J - V$ features in organic crystals used to distinguish these current regimes are much less pronounced in non-crystalline organics, complicating distinction of OLED current regimes [77,66,75]. In TCL current, it is assumed that strong carrier trapping effects impede carrier transport. That is, as electric field is increased, driving higher currents, large numbers of charges are trapped during transport. Trapped carriers are temporarily removed from the carrier population and can no longer contribute to current density. As the electric field is further increased the vast majority of these sites become statistically filled, as the quasi-Fermi level exceeds the trapping level, and TF-SCL current flow ensues. The TCL current region is noted to have a high polynomial (super-linear) dependence on applied voltage. (Note that this current regime has the potential to be confused with dielectric breakdown, but a detailed understanding of the OLED current mechanism should preclude this diagnosis at typical applied fields [77].) The particulars of the polynomial relationship of the $J - V$ characteristics are related to how the trapping level varies in energy space. The theory and numerics of TCL been

well documented [77]. Several types of carrier distributions have been considered to represent the trap distributions within an amorphous materials, these include discrete and continuous (continuous distributions include exponential and Gaussian distributions [75]). The primary motivation for TCL current is accounting for the affect that traps have on removing charge carriers from the free-carrier population. Further, the overall effect of deep trap states is to lower the effective carrier mobility, μ_{eff} , e.g. for electrons, as shown below:

$$\mu_{eff,n} = \mu_n \left(\frac{n_f}{n_t + n_f} \right) \quad 3.44$$

$$\mu_{eff} = \frac{\theta}{1 + \theta} \mu \quad 3.45$$

where n_{eff} is the free carrier electron concentration, n_t is the trapped electron concentration and μ_n is the trap-free electron mobility. Of course, an analogous hole equation may be produced. Moreover, assuming an exponential distribution of electron trap states, the density of trap states in an energy interval, N_t , may be written as a function of energy level, ϵ , as follows:

$$N_t(\epsilon) = \frac{N_{t,0}}{kT_t} \times \exp\left(\frac{\epsilon - E_{LUMO}}{kT_t}\right) \quad 3.46$$

where $N_{t,0}$ is the total density of deep trap states, T_t is the characteristic temperature of the exponential distribution and E_{LUMO} is the energy level of the LUMO level. Again, an analogous exponential deep trap distribution may be considered for hole carriers. It follows, then, that the full analytical TCL current density, J_{TCL} , for the exponential deep trap distribution described in Equation 3.46 may be written and is given below:

$$J_{TCL} = N_{LUMO} \mu_n q^{1-l} \left(\frac{\epsilon l}{N_t(l+1)} \right)^l \left(\frac{2l+1}{l+1} \right)^{l+1} \frac{V^{l+1}}{L^{2l+1}} \quad 3.47$$

where N_{LUMO} is the total density of states in the LUMO level and $l = (T_t/T)$ is ratio of the trap system characteristic temperature and the ambient temperature of the system, T [66,77]. Further discussion of the practicality of such formalism will be discussed in the next section on the injection limit.

3.4.1.4 Trap-Free Space-Charge Limit

In literature, reports have been made where current density-voltage ($J - V$) characteristics have suggested trap-free space-charge limited current. However, the significant and non-negligible trapping effects of organic materials rule out this effect for all but the purest films deposited with the highest quality deposition processes. In the presence of trapping states this theory must be modified; this is the motivation for trap-charge limited theory. Another important consideration is that the SCL formulation is intended for single-electrode injection with single-carrier current. This is not the case for OLEDs, where it is essential to inject both

charge carriers, electrons at the cathode and holes at the anode. Thus the current flow in OLEDs is bipolar with a heterojunction used to confine both sets of charge carriers at a common surface. These operating conditions tend to increase restrictions leading to SCL current. Finally, SCL current will be ignored in this treatment as there is insufficient evidence that it is unlikely to occur in thin OLEDs without extremely pure films.

3.4.2 Injection Limit

According to Parker and colleagues [131], strongly injecting charge carrier controls $J - V$ response; weakly injecting barrier controls luminance (and efficiency) response. Therefore, even though, one barrier may produce SCL; the other barrier may be injecting weakly and thus produce efficiency limitations. Further, the injection limit occurs when carrier injection at one (or both) of the contacts limits total device current. Fundamentally, this occurs when injection inefficiencies outweigh ohmic losses due to charge transport. The implications of injection limited current are important to consider. Injection limited current implies that by reducing the injection barrier or further enhancing injection, OLED luminous efficacy may be improved. In the literature, special accommodations, including a variety of interfacial layers, have been incorporated to circumvent the injection barrier, allowing for more efficient charge injection into the organic semiconductor bulk. As will be discussed in this section, for the particular lab-grade devices in this work, there is sufficient evidence that the OLED devices are injection limited.

A very detailed study was conducted on small molecule OLEDs by Baldo and colleagues [137]. In particular, this work focused on Alq₃ as an electron transport material, which a focus material in our lab-grade devices. This work concludes that typical ~100nm-thick small molecule OLED devices fabricated by thermal evaporation are injection limited. A variety of tests were conducted. In one test, a thin, phosphorescent probing layer (PtOEP) was used as a proxy for determining the OLED current dependence on carrier concentration. This test demonstrated that the current relation is less dependent on space charge than expected for SCL conditions. In another test, single-carrier OLED devices with material thicknesses between 40nm and 200nm were fabricated. In each device, the driving voltage required to reach a set current density ($J=10\text{mA/cm}^2$) was recorded. The governing current equations in the SCL and TCL regimes have higher dependences on thickness than on drive voltage (Equations 3.43 and 3.47). Moreover, for constant current in the bulk limited regime, the driving voltage should increase less than linearly with thickness. Experiments showed a linear relationship on the drive voltage versus thickness plot, suggesting the current flow was not bulk limited. Similar tests were conducted for a variety of cathode materials including the LiF/Al bilayer cathode considered in this work. It was pointed out that since Alq₃ has a rather large molecular dipole moment, which further hinders injection level (due to disorder) into the organic at the cathode side. This work highlights several justified and reasoned results which conclude that the current flow in OLEDs with ~100nm thick devices employing Alq₃ as an ETL will most likely be cathode injection limited.

Another approach is to consider the two criteria which must be satisfied for SCL effects to occur [125]. First, high-level injection is required to provide sufficiently injected space charge in order to redistribute the electric field. The fulfillment of this condition is dependent on the injection barrier height. Second, the dielectric relaxation time must be longer than carrier drift

time. It was concluded that for most interfaces (and in particular multi-layered OLEDs, considered in this work) the level of carrier injection is insufficient to render current bulk limited.

The first successful application of the full semiconductor equations to PLEDs including injection from thermionic and field effects concluded that for injection barriers, Φ_B , greater than 0.3eV, the space-charge carrier concentration does not sufficiently alter the electric potential profile to induce SCL current conditions [120]. While, the actual injection barrier heights have been the subject of many investigations with some level of disagreement, research suggests that few cathode injection materials form energy barriers which satisfy this condition. The Al/LiF barrier is considered to have a barrier height of 0.3-0.5eV.

For devices in which the effective injection barrier is greater than 0.3eV, i.e. the interface is a weak injector of charges, the device will be injection limited over a wide range of device thicknesses and electric fields at room temperature. Consequently, the space-charge coupling to the Poisson equation does not markedly redistribute the electric field, thereby negating the criterion that SCL may occur. It should be noted that while this assumption neglects space-charge effects leading to effective redistribution of the electric field, it doesn't preclude substantial recombination current. Additionally, TCL, which is an extension of SCL, must abide by the same criteria. And, as such, the SCL mechanism is unlikely to occur. However, it should be noted that as device thicknesses increase there is a transition to SCL. Also, the multi-layered structures used in modern-day OLEDs are much more complicated than can be readily solved from any of the current limit models; therefore, for the highest accuracy device analysis, solution of the full semiconductor current equations is suggested. This work extends a simplification of these commonly made arguments for injection limited current analysis.

3.5 Conclusion

Within this chapter, a summary of important concepts of the OLED electrical system have been included. Concepts related to the present-day understanding of the organic transport mechanism and the metal-organic injection mechanism are introduced. In addition, the interaction of the injection and transport mechanisms is discussed, which leads to further insight of the $J - V$ response curves that are ubiquitous within OLED/LED literature. As highlighted by Figure 3.11, a wealth of information about the transport mechanism can be gained merely from $J - V$ curves. The information introduced in this chapter will be used to gain physical insight to numerical results obtained in the following chapters.

Chapter 4. Analysis of one-dimensional space-charge-limited effects in a single-layer organic light-emitting diode

4.1 Introduction

In the previous chapter, the conceptual device physics of the OLED electrical system were introduced. Of particular importance to the electrical system of equations is the current controlling regime of carrier transport (injection limited versus space-charge limited). In this chapter, numerical methods will be described and implemented for the general transition to the space-charge limited (SCL) current regime. The ability to identify the transition to the SCL regime is crucial in understanding the physics of device operation. To date, nearly all analysis in the field of OLEDs has focused on the Richardson-Schottky (RS) injection mechanism. In this work, the Scott-Malliaras (SM) injection mechanism, which is formulated for low mobility materials, is considered. The format of the findings mirrors the original RS results found in Ref. 114. The current limits from the SM injection mechanism are different than those from the RS mechanism due to the lower effective injection constant occurring in the SM mechanism. Moreover, the focus of this chapter will be to numerically solve the one-dimensional OLED equations implementing common numerical techniques in literature to determine the SCL current regime for the SM mechanism for a single-layer OLED.

4.2 One-dimensional numerical solution

The system of equations has been previously described in Chapter 3 (Poisson equation, Equation 3.5; carrier continuity equations, Equations 3.9 and 3.10; drift-diffusion equations, Equations 3.7 and 3.8; Scott-Malliaras injection equations, Equations 3.29-3.32). A summary of these equations is presented in Table 4.1, below. The procedure and numerical methods required to solve the OLED equations for the one-dimensional case are now described. Additionally, the formulated difference equations that result from these techniques are available in Appendix B.

Table 4.1: Summary of equations solved in this chapter

Bulk Equations:

Poisson Equation:

$$\nabla \cdot (\epsilon \nabla \phi) = -q(p - n)$$

Electron Continuity Equation:

$$\frac{\partial n}{\partial t} - \frac{1}{q} \nabla \cdot \vec{J}_n = -R$$

Electron Drift-Diffusion Equation:

$$\vec{J}_n = -q\mu_n n \nabla \phi + kT\mu_n \nabla n$$

Hole Continuity Equation:

$$\frac{\partial p}{\partial t} + \frac{1}{q} \nabla \cdot \vec{J}_p = -R$$

Hole Drift-Diffusion Equation:

$$\vec{J}_p = -q\mu_p p \nabla \phi - kT\mu_p \nabla p$$

Recombination Rate:

$$R = \frac{q\mu_{max}}{\varepsilon} np$$

Boundary Equations:

Applied Voltage:

$$\phi(x = \text{Cathode}) = 0$$

$$\phi(x = \text{Anode}) = V_{app}(t)$$

SM Injection Equation:

$$J_{SM}(\Phi_B, E) = 4\Psi^2 N_0 q \mu E \exp\left(\frac{-\Phi_B}{kT}\right) \exp(\sqrt{f})$$

$$\Psi(f) = f^{-1} + f^{-1/2} - f^{-1}(1 + 2f^{1/2})^{1/2}$$

$$f = \frac{qEr_c}{kT}$$

$$r_c = \frac{q^2}{4\varepsilon kT}$$

Internal Current Condition (Not applicable for SLOLED):

$$J_p = \frac{qA^*T^2}{N} [p(x^-)Bol(x^-) - p(x^+)Bol(x^+)]$$

$$J_n = \frac{qA^*T^2}{N} [n(x^-)Bol(x^-) - n(x^+)Bol(x^+)]$$

$$Bol(x) = \begin{cases} \exp\left(-\frac{\Delta E}{kT}\right), & \Delta E > 0 \\ 1, & \Delta E \leq 0 \end{cases}$$

4.2.1 Solution procedure

In order to solve the one-dimensional equations, an initial condition must first be solved. This case is physically defined by the situation where there is positional invariance of the Fermi-level (E_F), implying that each carrier maintains an identically zero total current density (i.e., $\vec{J}_n = \vec{J}_p = 0$) on the solution domain. Mathematically, this condition is equivalent to the case $V_{app} = V_{bi}$, where V_{bi} is the difference between the cathode and anode work functions (see [Figure 4.2B](#) for an energy band diagram description). In this case, the electric potential is assumed to vary linearly across a one-dimensional device. The initial condition may then be relaxed to account for any variation from, for example, doping density occurring in the bulk. Iterative modifications to the electric potential may be used for convergence of the numerical solution (see [Appendix B](#) for discretizations). The system's initial conditions are specified below:

$$\phi_0(x) = \frac{1}{q} (\Phi_{B,cathode} - \Phi_{B,anode}) \frac{x}{L} \quad 4.1$$

where $\phi_0(x)$ is the positional initial condition of the electric potential. Here $x = 0$ is taken as the cathode position; and $x = L$ is taken as the anode position. The carrier initial conditions are specified below:

$$n_0(x) = N_{LUMO} \exp\left(\frac{E_{LUMO} - E_F}{kT} + \frac{\phi_0(x)}{V_T}\right) \quad 4.2$$

$$p_0(x) = N_{HOMO} \exp\left(\frac{E_F - E_{HOMO}}{kT} - \frac{\phi_0(x)}{V_T}\right) \quad 4.3$$

where $n_0(x)$ and $p_0(x)$ specify the positional initial electron and hole carrier concentrations, respectively, and $N_{LUMO(HOMO)}$ is the number of carrier states for electrons(holes).

Next, the electric potential system's boundary conditions are modified in time to represent an applied voltage response on the system, which leads to the following boundary conditions on the electric potential:

$$\phi(x = 0, t) = \phi_{cathode} = 0 \quad 4.4$$

$$\phi(x = L, t) = \phi_{anode} = V_{app}(t) \quad 4.5$$

where, $V_{app}(t)$ is the applied voltage on the anode side. Conveniently, the applied voltage values are taken to be values of interest to the solution enabling the data capture and comparison at over a sweep of applied voltages. A steady-state response is signaled by the positional independence of the total current density. Voltage ramping is important in achieving self-consistent solutions to the system through use of converged initial conditions to begin the next voltage step. [Figure 4.1](#) pictorially describes a common solution procedure from above.

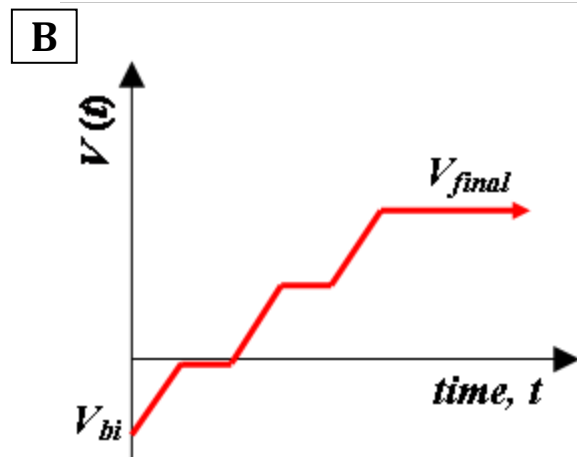
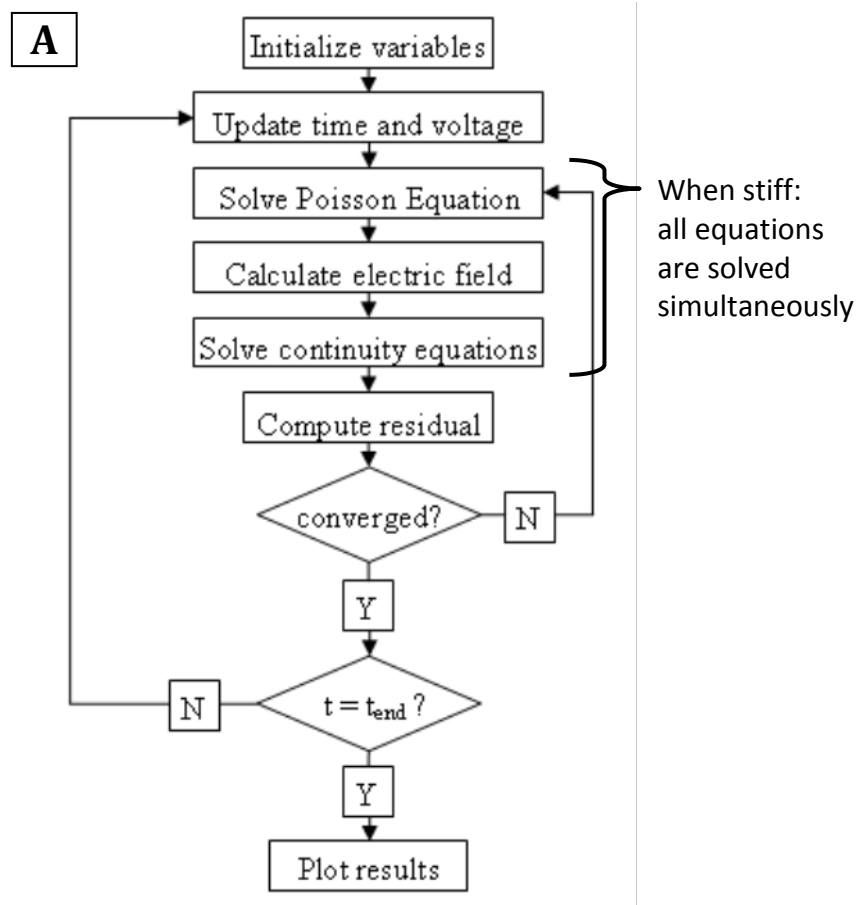


Figure 4.1: In A), program flow diagram showing solution technique for solving the semiconductor equations. In B), the anode applied voltage (relative to ground cathode voltage) as a function of time allowing the system to periodically find a steady-state solution, which is useful for outputting intermediate data for a JV sweep.

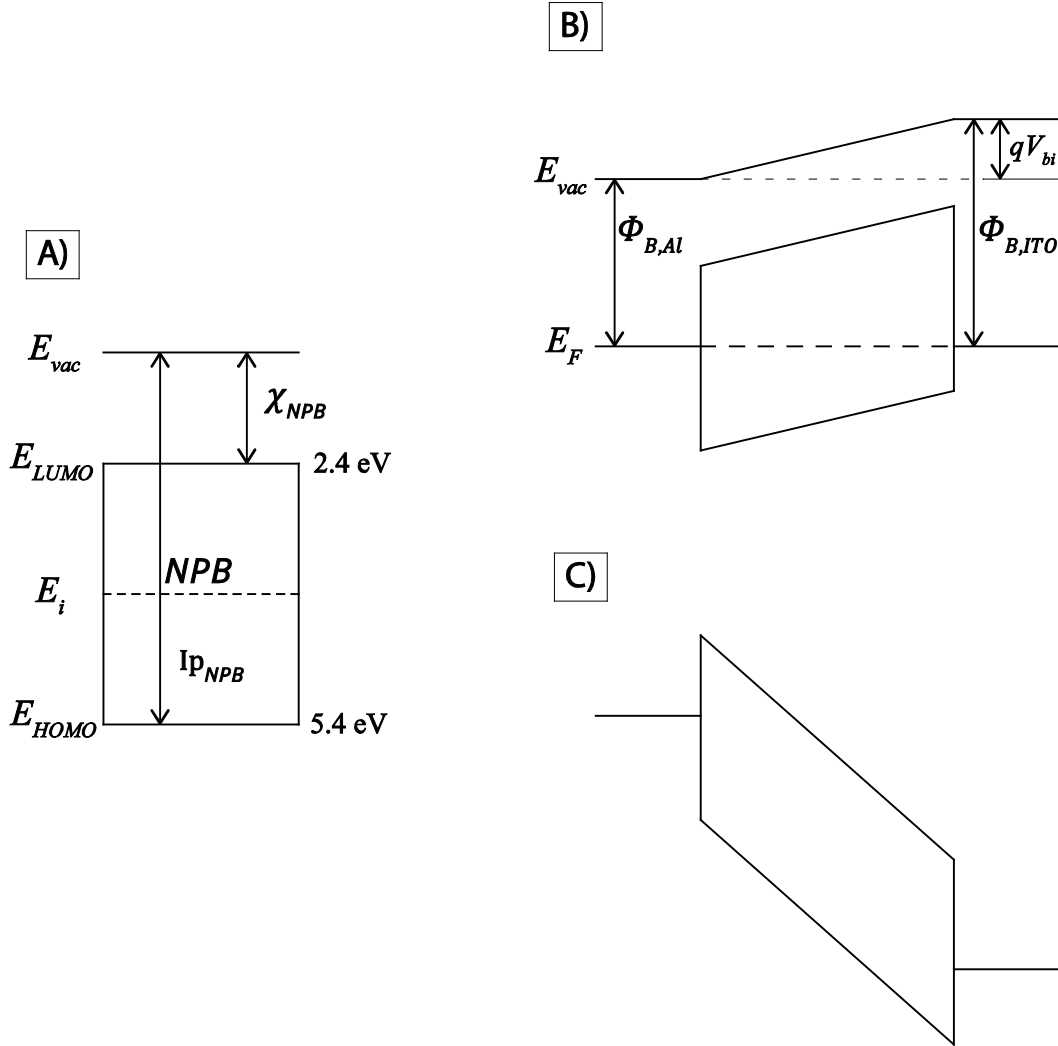


Figure 4.2: Energy band diagrams of (A) common band diagram description of the energy levels in common HTL, NPB, (B) example initial condition band diagram for the NPB material SLOLED device and (C) the band diagram as the applied voltage bends the bands forcing carrier injection.

4.2.2 Finite Difference Formulation

The finite difference method (FD) is a numerical technique for solving a wide range of partial differential equations on simple geometries [153]. In FD, Taylor series expansion is used to rewrite numerical derivatives as difference equations, which are based on neighboring nodes, such equations may simultaneously be solved with boundary conditions to achieve an accurate domain solution. Typical geometries are constructed by the geometric union of rectangles (for two-dimensional geometries) and regular hexahedrons (for three-dimensional geometries). While more general implementations of finite difference exist, e.g. finite boxes [154]. This work considers the finite difference method.

The first step in the finite difference method is to create a mesh to represent the geometry or domain on which the field equation(s) exists. An example of a rectangular two-dimensional

geometry with a rectangular mesh superimposed on it is shown in Figure 4.3. Depending on how the user defines the mesh, either the areal center of each individual element or the intersections of the wire mesh represent nodes at which the following numerical expressions are evaluated. The intuitive, well-defined node numbering schemes within rectangular geometries prove convenient for node connectivity since the nodes may be accessed through row and column locations rather than requiring a look-up table. This is especially useful for aiding implementation and inversion of the matrix since very efficient sparse matrix algorithms exist.

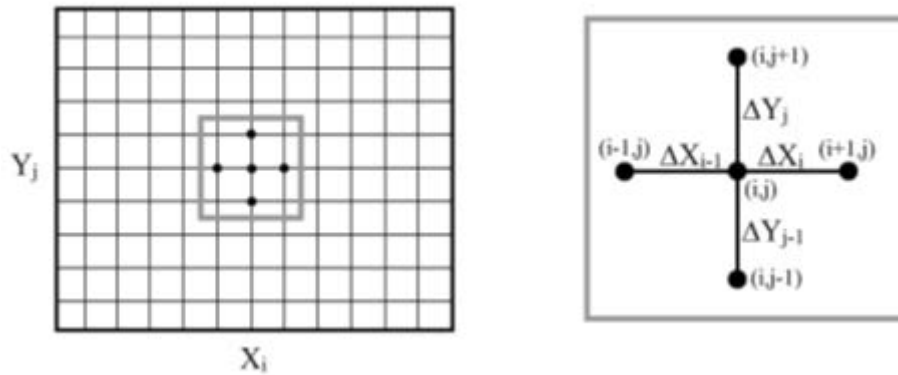


Figure 4.3: Finite difference method mesh. At left, a wire mesh divides a geometry up into discrete points. At right, the 5-point star (for 2d FD) used for basic Laplacian evaluation.

Note as this section is primarily concerned with setting up the one-dimensional FD system, the domain is a line with constant spacing, Δx , with a total thickness, L , equal to the thickness of the organic material (taken as 100nm). These points are then used to evaluate and solve the set of equations. Following the construction of a mesh, FD uses Taylor expansion to approximate spatial and temporal derivatives as discretizations of the neighboring nodes. Below, Taylor expansion is used to approximate the value of variable f at a small positional perturbation, Δx , from a position, x , where the value of f and an arbitrary number of derivatives of f (i.e., f' , f'' , f''' , etc.) are known either analytically or through approximation:

$$f[x + \Delta x] \approx f[x] + \frac{1}{1!}f'[x](\Delta x) + \frac{1}{2!}f''[x](\Delta x)^2 + \dots + \frac{1}{n!}f^{(n)}[x](\Delta x)^n \quad 4.6$$

where brackets are used to distinguish functional dependence on position from the power-series expansion of the positional difference. Through use of method of undetermined coefficients, the governing equations may be recast in terms of such approximations. These numerical approximations may be back substituted into the governing equations.

4.2.3 Potential System Numerics

For the Poisson Equation, the Laplace operator evaluation is of interest. The approximation is shown below (in its second-order accurate numerical approximation form) for one

dimension, x :

$$\nabla^2 \phi = \frac{d^2 \phi}{dx^2} \approx \frac{\phi_{i+1}}{(\Delta x)^2} - 2 \frac{\phi_i}{(\Delta x)^2} + \frac{\phi_{i-1}}{(\Delta x)^2} + O(\Delta x^2) \quad 4.7$$

where ϕ_i is the nodal electrical potential of the organic medium at node i , subscript i is an index to the spatial discretization of the wire mesh with constant mesh spacing, Δx (Figure 4.3). For spatially discretized wire mesh with constant spacing, Δx , $O(\Delta x^2)$ is the truncation error relation to the mesh spacing. This implies that as the mesh is further resolved, numerical accuracy improves (provided instability does not occur). The discretization shown in Equation 4.7 may then be recast as a linear equation in terms of values of the neighboring nodes shown below to represent the Poisson equation:

$$\phi_{i+1} - 2\phi_i + \phi_{i-1} = -\frac{q}{\varepsilon}(p_i - n_i) \quad 4.8$$

where n_i and p_i , respectively, represent the electron and hole carrier concentrations at index location, i . The boundary conditions on the electric potential system are also shown in Table 4.1. An example applied potential difference ramp is shown in Figure 4.1B.

4.2.4 Carrier Concentration System Numerics

4.2.4.1 Spatial discretization – Scharfetter-Gummel

The Scharfetter-Gummel (SG) discretization is a commonly employed technique for achieving accurate and stable element carrier current values (see Appendix B for numerics) [83,117,114]. The local Peclet number, or the local ratio of the magnitude of advection to diffusion within a region of space, is the critical parameter governing the solution profile in the local element. As the applied voltage is increased, the Peclet number is likewise increased, and thus too is the drift contribution to carrier current density. In this case, the local solution shifts from one requiring two boundary values (diffusion limited) to one that requires one boundary value (advection limited) to be satisfied. In this situation, a discontinuity develops in the solution near the side with larger diffusion. This condition in the drift-diffusion equations is referred to as a *singular perturbation* [117,153]. According to Ref. 83, numerical instability results when the voltage difference between mesh points exceeds $2kT/q$. The SG discretization, uses the Bernoulli factor, B , to effectively approximate the drift- and diffusion-only limits:

$$B(x) = \frac{x}{\exp(x) - 1} \quad 4.9$$

where x is the position between two elements. Further, the current density is approximated as [93]:

$$J_{n,i-1/2} = \frac{qD_{n,i-1/2}}{\Delta x} \left[n_i B \left(\frac{V_i - V_{i-1}}{V_T} \right) + n_{i-1} B \left(\frac{V_{i-1} - V_i}{V_T} \right) \right] \quad 4.10$$

In many cases, it is useful to rewrite the carrier concentrations in terms of the electron(hole) quasi-Fermi level values, $F_n(F_p)$, as follows:

$$n = n_0 \exp \left(\frac{q(\phi - F_n)}{k_B T} \right) \quad 4.11$$

$$p = n_0 \exp \left(\frac{q(F_p - \phi)}{k_B T} \right) \quad 4.12$$

where, n_0 is the maximum number of available electronic states in the organic material and is taken to be related to the number density of molecules ($\sim 10^{21} \text{ cm}^{-3}$ [114]).

Furthermore, the boundary values must also be satisfied. This condition can become quite cumbersome since both boundary conditions are highly non-linear and are, in general, formulated as Neumann conditions. The technique used in this analysis was to alternate between updating each boundary condition for carrier type and iterating until convergence.

4.2.4.2 Temporal discretization – Backward Euler

The Backward Euler method is an implicit (stable) difference equation that is used to discretize the transient effects of the continuity equations. The Backward Euler method may be written as:

$$y_i^{k+1} = y_i^k + hf(t^{k+1}, y_i^{k+1}) \quad 4.13$$

where superscript k represents the current time step solution (y_i), h is the update step size and f represents the functional dependence of the mass matrix on the new time step. The functional dependency f is found from Taylor expansion or other analytical differentiation.

4.2.4.3 Non-linear solution techniques

The voltage ramp (Figure 4.1) is accompanied by non-linear effects arising in the carrier densities (a manifestation of the exponential coupling to the potential system). Moreover, it is recommended to ramp the potential and then allow for the system to reach equilibrium before proceeding to the next voltage ramp. In effect, at low applied potential ($\lesssim 3V_{bi}$), the Gummel iteration method is a simplified technique for achieving numerical convergence [82]. This method is, in effect, a decoupled procedure whereby the potential equation is first ramped and then the decoupled carrier density equations are solved (see Appendix B for numerics). After the applied potential exceeds several volts the equations become coupled and require full Jacobian evaluation to solve the system. The common Newton's method technique can be used to solve the nonlinear systems of equations, which is shown below for a vector of equations:

$$\vec{x}_{n+1} = \vec{x}_n - \frac{f(\vec{x}_n)}{f'(\vec{x}_n)} \quad 4.14$$

where \vec{x} is the solution vector, n is the current solution step, $f(\vec{x}_n)$ is the residual from the set of equations and $f'(\vec{x}_n)$ is the system Jacobian.

4.2.4.4 Computing the Numerical Solution

The resulting equations, above, are cast into the following form:

$$A\vec{x} = \vec{b} \quad 4.15$$

where A , commonly referred to as the mass matrix, contains the operations on the neighboring nodes, \vec{x} is the solution vector ($\vec{x} = \{\phi, n, p\}$) and \vec{b} is the forcing (or load) vector. Consider a mesh with N elements, the resulting sizes of the previously stated matrix and vectors are A : $3N \times 3N$; \vec{x} : $3N \times 1$ and \vec{b} : $3N \times 1$.

These equations were implemented via sparse linear array construction in Matlab® [162]. The class of sparse functions allow for rapid matrix creation, assignment and operation of sparse arrays. The sparse class is ideal for matrices which have very few, and preferably periodic, non-zero values. In essence the sparse class removes the need to assign a double precision value to each element of an array in lieu of creating a reference to the non-zero quantities within a column. Additionally, an entire class of efficient operations has been created for the Matlab platform. Thus operations are specifically adept at manipulating these arrays.

The numerical solution of the linearized equations were solved using the Matlab backslash operator (“\” or alternatively the built-in *mldivide* function), which is an optimized, overloaded solver which uses both direct and iterative solution depending on the nature of the matrix, A .

4.3 NPB device numerical solution

The device which will be discussed in Chapter 5 has device structure: ITO/NPB/Al. The electronic properties of the NPB are available in the diagram in Figure 4.2. Here, the work function of Al is taken to be 4.1eV, and the work function of ITO is taken to be 4.7eV. The results of the one-dimensional numerical model at an applied voltage of 10V are shown below (Figure 4.4). Additionally, a more practical device structure of ITO/PEDOT/NPB/LiF/Al is modeled below in Figure 4.5. Here, the anode and cathode injection barrier heights due to the inclusion of PEDOT and LiF, respectively, are 0.5eV and 0.3eV. According to the Davids, et. al. article this device should be in the SCL regime. However, as is depicted in the bottom right plot of Figure 4.5, the current is less than the Mott-Gurney SCL current limit, which means that these conditions do not produce an SCL current. The potential barrier required by the SM mechanism to generate SCL current is the topic of the next section.

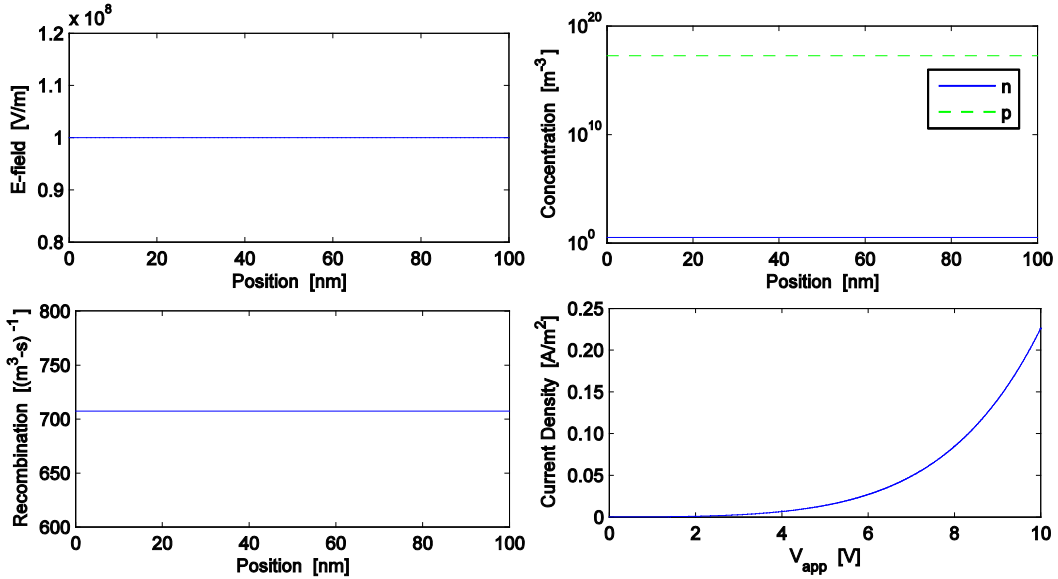


Figure 4.4: Results for an example single-layer device in the injection limited (IL) regime. The device is ITO/NPB(100nm)/Al. In A, device electric field; in B, electron and hole carrier concentrations; in C, recombination rate; in D, JV curve.

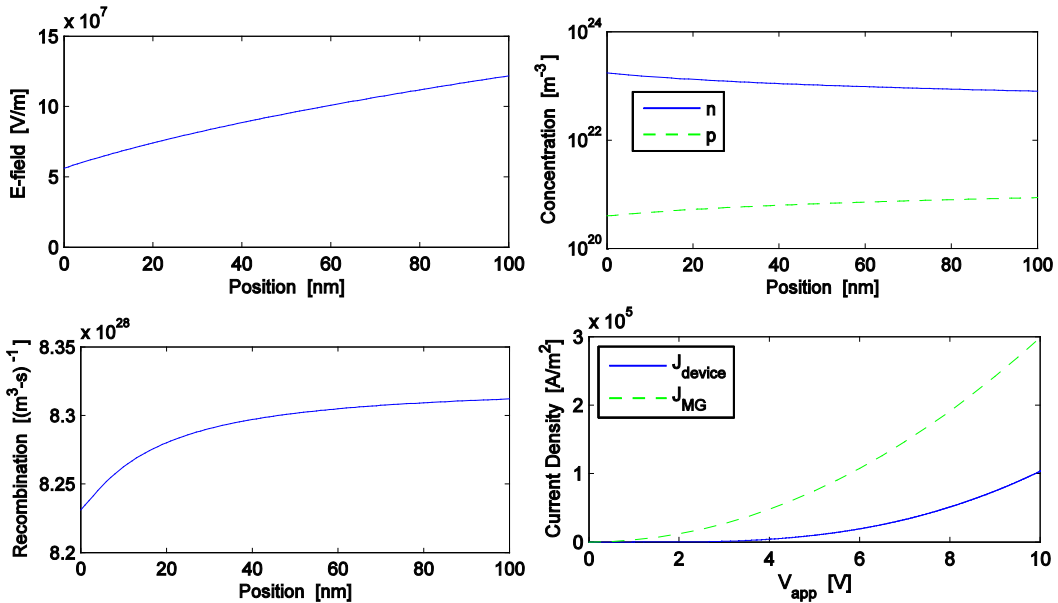


Figure 4.5: Results for an example single-layer device that is considered in the space-charge limited (SCL) regime according to criterion in Ref. 114. The device is ITO/PEDOT:PSS/NPB(100nm)/LiF(0.5 nm)/Al. In top left, device electric field; in top right, electron and hole carrier concentrations; in bottom left, recombination rate; in bottom right, JV curve versus Mott-Gurney SCL limit, J_{MG} (Equation 3.43).

4.4 IL/SCL cross-over for SM model

The results included below identify the difference between the IL/SCL transition from the Scott-Malliaras model (Equations 3.29-3.32) and compare it to the documented IL/SCL transition in the widely used OLED electrical model in Ref. 114 (Equations 3.27-3.28). In the article by Davids, et. al. [114], it is concluded that for SCL current the barrier height must be $\sim 0.3\text{-}0.4\text{eV}$. Due to the reduced effective injection constant for the SM mechanism, it is expected that the barrier height will need to be lower than the barrier height predicted in Ref. 114. In order to make a direct comparison with this work, the same conditions and properties are chosen. Figure 4.6 (left) can then be used to determine the SCL cross-over barrier by comparing the JV characteristic with that of the Mott-Gurney current relation for SCL current (Equation 3.43). The figure shows that the barrier height required by the SM mechanism to achieve SCL conditions is 0.24eV . Note solid lines in Figure 4.6 depict SCL current conditions.

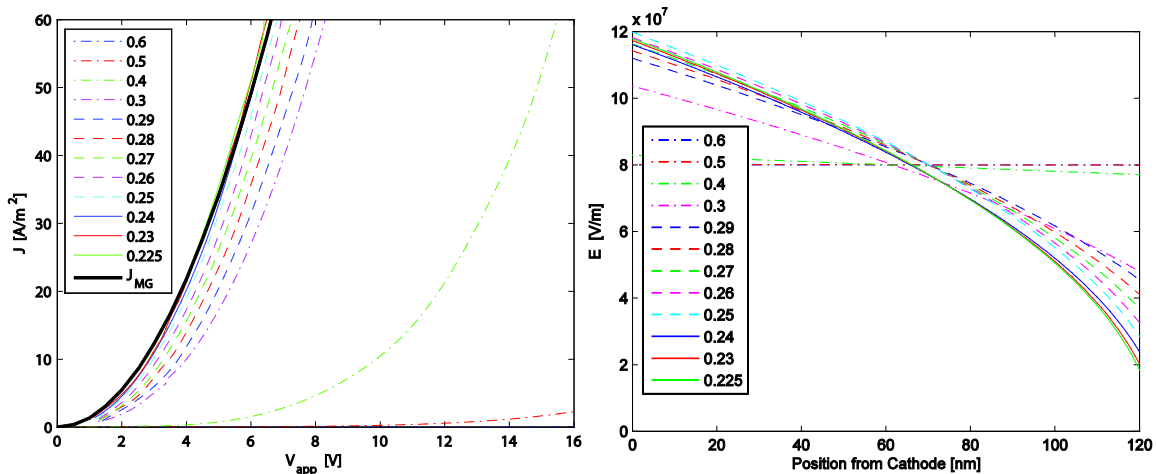


Figure 4.6: Transition from IL to SCL regime as a function of injection barrier height. The device is: ITO/MEH-PPV(120nm)/Al (same as in [114], for comparison), where the hole barrier height is varied according to the inset values. At left, JV curves compared to Mott-Gurney current. At right, the electric field profiles. Non-uniform profiles are caused by SCL effects.

4.5 Conclusion

The injection to space-charge limited transition has been identified for the SM mechanism. The effective barrier height required to yield space-charge limited injection is roughly 0.24eV , which is lower than the $0.3\text{-}0.4\text{eV}$ range predicted in Ref. 114. This means that devices are less likely to be SCL than previous theory predicts. Further, due to the complexity of the set of equations (and related physical phenomena) of the semiconductor equation set for OLEDs, one should conclude injection and space-charge limited current regimes on a per device basis.

Chapter 5. Approximating the Electrical Enhancement Effects in a Nanopatterned, Injection-Limited, Single-Layer Organic Light-Emitting Diode

5.1 Introduction

Within this chapter, a numerical solution technique is developed allowing approximation to the effects brought about by internal geometric modification of OLED devices in the double-sided injection limited regime. In particular, the electrical enhancement effects brought about from nanocolumn-pressing a single-layer PLED are analyzed. A number of pertinent enhancement effects are approximated by this model including charge balance efficiency, confinement efficiency, total current enhancement and recombination efficiency. The results quantify the electrical enhancement effects. The results show favorable enhancement factors that exceed the enhancement of the equivalent thickness-reduced organic film device.

The material in Sections 5.2-5.4 of chapter contains is an excerpt of the previously published article by the author: *“Approximating the electrical enhancement effects in a nanopatterned, injection-limited, single-layer organic light-emitting diode”* [140]. Additionally, this work will be extended to provide an optimization analysis for more general patterning dimensions.

5.2 Background

While the first reports of high efficiency OLEDs (~1% EQE) included a double-layer of small molecule organic materials sandwiched between two electrodes, a resurgent interest in single-layer organic and polymer light-emitting diodes (SLOLED/SLPLED) has surfaced [49-52]. SLOLED technology is complemented by recent advances in solution-processable molecular emitters and presents itself as a workaround to common problems facing the solution processing of consecutive organic layers including interlayer mixing and solvent corrosion of previous layers [61,141,142]. Unfortunately, despite the inherent processing advantages of SLOLED technology, it is challenging to produce the balanced injection and transport conditions required to ensure maximum carrier recombination. Recent reports, however, have demonstrated techniques that can effectively compensate for unbalanced material properties, which include the use of micrometer-thick SLPLEDs to achieve nearly total carrier recombination [49] and incorporation of co-doped layers into devices with thinner, more conventional thicknesses (~100nm) [50,51].

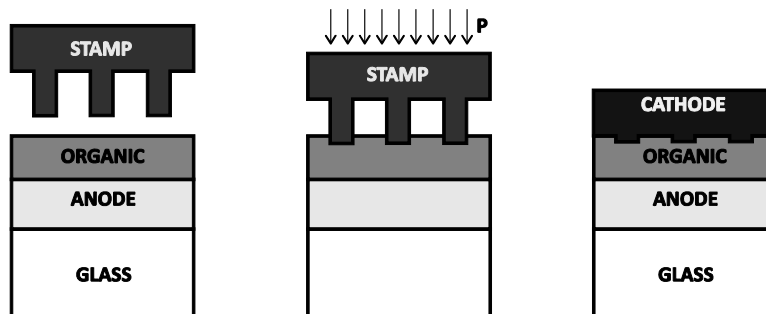


Figure 5.1: Nanoimprint pressing process realizing cathode structuring.

In this work, we address the problem of current balance through incorporation of nanoimprint stamping process (Figure 5.1) that has been shown to enhance carrier injection and luminance in heterojunction OLED devices [143]. This step provides the ability to controllably modify the geometries of the organic active layers on nanoscale dimensions (~100nm feature sizes). Nanoimprinting is a high throughput process and is compliant with roll-to-roll technology [145]. Finally, while this work focuses on enhancements made to the OLED electrical system through nanoimprint stamping, we note that multi-layer stamps may allow for techniques to simultaneously enhance the optical system [146].

5.3 SLOLED Current Theory

5.3.1 SLOLED current analysis

SLOLED electrical operation begins with application of an electric field, which induces carrier injection and transport into the organic medium (Figure 5.2). Carriers recombine to form bound electron-hole pairs, or excitons. Emission occurs as favorable radiative exciton routes spontaneously decay.

In an OLED device, the total, local current density, \mathbf{J} , at any location in the organic material may be found as the superposition of the local, electron and hole current densities, \mathbf{J}_n and \mathbf{J}_p , respectively, as follows:

$$\mathbf{J} = \mathbf{J}_n + \mathbf{J}_p \quad 5.1$$

where, bold-faced type is used to denote vector quantities. For purposes of avoiding confusion with local and average current densities in the forthcoming analysis and device figures of merit, in specific related to the ambiguous description of surface area for variable cross section current paths, we cast device current relations in terms of current (rather than current density).

The total device current, I_{tot} , under steady-state operation, may be obtained through integration of Equation 5.1 or from knowledge of both carrier currents at an injecting electrode, as represented below:

$$I_{tot} = \iint_{A_s} |\mathbf{J} \cdot \mathbf{n}_s| dA = I_n^{cath} + I_p^{cath} = I_n^{an} + I_p^{an} \quad 5.2$$

where, at either electrode, \mathbf{n}_s is the vector surface-normal of the electrode surface, A_s is the electrode surface path and A_{proj} is the projection of the nanopatterned surface path onto a planar electrode. As an example of the above nomenclature, I_n^{cath} is the total cathode electron current; this term may be found from an integral similar to Equation 5.2, where instead the total current term is replaced with the electron current and the integral is taken at the cathode electrode.

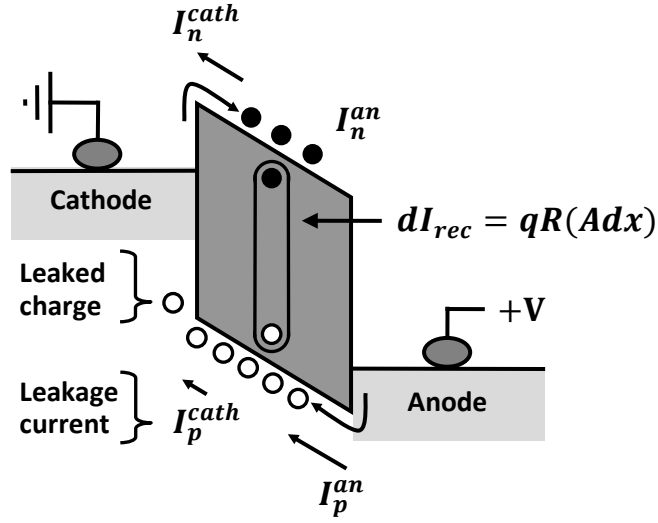


Figure 5.2: Energy diagram with superposed current map (magnitude of arrows) indicating the expected injection and leakage currents within a SLOLED of structure: ITO/NPB/Al for a one-dimensional device. Injection currents: I_p^{an} and I_n^{cath} ; leakage currents: I_p^{cath} and I_n^{an} .

Carrier recombination in OLEDs takes place via a Langevin process [146]. The total recombination current, I_{rec} , may be found through integration of the local recombination rate, R , over the volume, V , of the semiconductor bulk, as described below:

$$I_{rec} = \iiint_V qR dV = I_n^{cath} - I_n^{an} = I_p^{an} - I_p^{cath} \quad 5.3$$

where q is the electron charge. In Equation 5.3, for the one-dimensional case, the differential volume, dV , may be expressed as Adx and is written as such in Figure 5.2 and Figure 5.3. The recombination rate may be defined as follows:

$$R = \gamma np \quad 5.4$$

where $n(p)$ is the local electron(hole) carrier concentration and γ is the recombination factor, specified below:

$$\gamma = \frac{q(\mu_n + \mu_p)}{\varepsilon} \quad 5.5$$

where $\mu_{n(p)}$ is the electron(hole) carrier mobility and ε is the permittivity of the organic layer. Further, the device recombination efficiency, η_{rec} , may be written as [146]:

$$\eta_{rec} = \frac{I_{rec}}{I_{tot}} \quad 5.6$$

where, in the above equation, the recombination efficiency may be found through Equations 5.2-5.3. In terms of OLED devices, efficient multilayer structures have η_{rec} near unity [22]; however, SLOLED devices, without a heterojunction, have less control over minimizing leakage currents resulting from injection carrier current misbalance and less control over producing high recombination cross sections resulting from the energetic heterojunction barrier to charge transfer. Furthermore, we are interested in investigating the potential to improve recombination efficiency as a result of nanopatterning.

As the SLOLED device performance varies depending on the path carriers take through the organic medium, current is subdivided into discrete flow pathways, referred to as current pathways. A formal description of the current pathway analysis follows in Section 5.3.7. Along an arbitrary current pathway, i , the pathway recombination efficiency, $\eta_{rec,i}$, can be broken apart to isolate the device function of the contacts and bulk. The efficiency descriptions are portrayed in graphical form in Figure 5.3.

The carrier (injection) balance efficiency, η_{bal} , describes the ability of the SLOLED to inject nearly balanced electron and hole injection currents and provides an important metric to efficient injection in SLOLEDs. The pathway-specific current (injection) balance efficiency, $\eta_{bal,i}$, is described by the ratio of the pathway-specific carrier *injecting* currents ($I_{n,i}^{cath}$ and $I_{p,i}^{an}$), shown in the following relation:

$$\eta_{bal,i} = \frac{\min(I_{n,i}^{cath}, I_{p,i}^{an})}{\max(I_{n,i}^{cath}, I_{p,i}^{an})} \quad 5.7$$

where $\min(\max)$ is the minimum(maximum) functions.

The efficiency of confining current (or rather minimizing leakage currents) is related to the amount of injected current that recombines before it escapes as leakage current ($I_{p,i}^{cath}$ and $I_{n,i}^{an}$). The pathway (bulk) carrier confinement efficiency, $\eta_{cnf,i}$, may be defined as the ratio of the recombined current to the smaller of the injecting currents, which is also the maximum possible recombination current for that level of injection balance, and is defined below:

$$\eta_{cnf,i} = \frac{I_{rec,i}}{\min(I_{n,i}^{cath}, I_{p,i}^{an})} = 1 - \min\left(\frac{I_{n,i}^{an}}{I_{n,i}^{cath}}, \frac{I_{p,i}^{cath}}{I_{p,i}^{an}}\right) \quad 5.8$$

Equations 5.7-5.8 can be used to provide a simplified definition of the pathway-specific recombination current, $I_{rec,i}$, in terms of the balance and confinement efficiencies as follows:

$$I_{rec,i} = \eta_{bal,i} \times \eta_{cnf,i} \times \max(I_{n,i}^{cath}, I_{p,i}^{an}) = I_{no_cnf,i} - I_{tot,i} \quad 5.9$$

where $I_{no_cnf,i}$ is the pathway-specific current in the absence of confinement (recombination) and is written below:

$$I_{no_cnf,i} = I_{n,i}^{cath} + I_{p,i}^{an} = (1 + \eta_{bal,i}) \times \max(I_{n,i}^{cath}, I_{p,i}^{an}) \quad 5.10$$

Through Equations 5.7-5.8, the recombination current may be written in terms of the balance and confinement efficiencies as follows:

$$I_{tot,i} = \left[1 + \eta_{bal,i} \times [1 - \eta_{cnf,i}] \right] \times \max(I_{n,i}^{cath}, I_{p,i}^{an}) \quad 5.11$$

It follows from Equations 5.6, 5.9 and 5.11 that the recombination efficiency may be described by the following relation:

$$\eta_{rec,i} = \frac{\eta_{bal,i} \times \eta_{cnf,i}}{1 + \eta_{bal,i} \times [1 - \eta_{cnf,i}]} \quad 5.12$$

As the SLOLED device efficiency metrics have now been defined for individual pathways, we describe the process to compare with a planar device. For any of the balance, confinement and recombination efficiencies, now denoted by $\eta_{(\cdot)}$, the pathway-specific enhancement metric, $F_{(\cdot,i)}$, may be found as follows:

$$F_{(\cdot,i)} = \frac{\eta_{(\cdot,i)}}{\eta_{(\cdot),0}} \quad 5.13$$

where $\eta_{(\cdot,i)}$ is the efficiency metric of the nanopatterned device and $\eta_{(\cdot),0}$ is the baseline metric for the equivalent planar device. The overall enhancement metric, $\bar{F}_{(\cdot)}$, which may be computed from the pathway-current-weighted average of $F_{(\cdot,i)}$, is computed as follows:

$$\bar{F}_{(\cdot)} = \frac{\sum_i [F_{(\cdot,i)} \times I_{tot,i}]}{\sum_i I_{tot,i}} \quad 5.14$$

In Equation 5.14, the value in the denominator is deliberately taken as the modified pathway current, rather than the baseline current, $I_{tot,0}$, to avoid double counting the current enhancement effects.

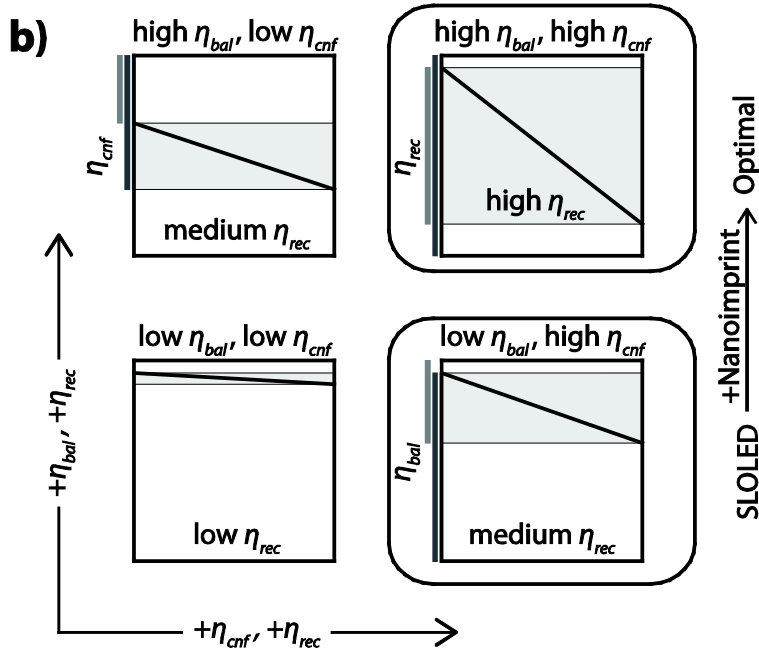
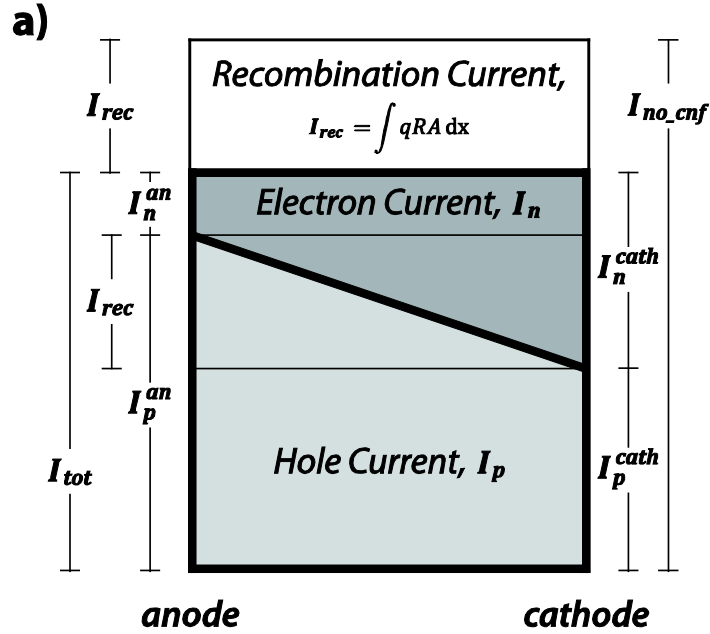


Figure 5.3: (a) Current profile within an SLOLED including visual representations of carrier currents, total carrier currents, total current, recombination current and unconfined current. (b) The influence of carrier balance efficiency, η_{bal} and confinement efficiency, η_{cnf} on recombination efficiency, η_{rec} . To facilitate understanding efficiency terms, the three efficiency terms are shown as a ratio of their graphically represented current equivalents.

We next consider the current balance conditions specific to the SLOLED device structure, ITO/NPB/Al, where NPB is *N,N'*-diphenyl-*N,N'*-bis(1-naphthyl)-1,1'-biphenyl)-4-4'-diamine and is

an ambipolar transport material (i.e., $\mu_{n,NPB} \approx \mu_{p,NPB} \sim 10^{-3} \text{ cm}^2/\text{V-s}$). For this particular device structure, ultraviolet photoemission spectroscopy (UPS) reveals that the electron injection barrier height at the NPB/Al interface is larger than the hole injection barrier height at the ITO/NPB interface [147,148]. Therefore, it can be assumed that the cathode-side injection is decidedly weaker than the anode-side injection, or in other words this is a hole-only device [149]. Moreover, a featured goal of the nanoimprint modification is to assist in restoring parity to injecting carrier currents. In addition, the condition of dominant hole injection allows us to add closure to the set of currents relations by identifying their individual dependencies on maximum injection current, now known to be the anode hole carrier current, as shown below:

$$I_{p,i}^{an} = \max(I_{p,i}^{an}, I_{n,i}^{cath}) \quad 5.15$$

$$I_{n,i}^{cath} = \eta_{bal,i} \times I_{p,i}^{an} \quad 5.16$$

$$I_{n,i}^{an} = \eta_{bal,i} \times [1 - \eta_{cnf,i}] \times I_{p,i}^{an} \quad 5.17$$

$$I_{p,i}^{cath} = [1 - \eta_{bal,i} \times \eta_{cnf,i}] \times I_{p,i}^{an} \quad 5.18$$

As a preliminary to further numerical treatment, it should be expected that the inclusion of the imprinted, periodic nanocolumns at the cathode-organic interface improves current injection through the formation of localized electric field hot-spots. For reasons described in the next section, this device is injection limited at both electrode-organic contacts. In the injection-limited regime, current injection possesses highly non-linear electric field characteristics occurring from Schottky barrier lowering. The localized increases in electric field are expected to produce large overall current injection enhancement at the patterned (cathode-organic) side. Also current injection enhancement at the unpatterned (anode-organic) side is expected but to a reduced extent.

Finally, it should be mentioned on the current flow in nanopatterned SLOLEDs may influence device lifetime. When considering charge transfer from a percolation model, additional stress to the field-enhanced regions may lead to premature device failure [150]. Further investigations into the device lifetime consequences of this modification are required.

5.3.2 OLED current models

Three different types of models are commonly discussed in literature to describe the overall current mechanism in organic devices with the distinguishing feature being the level of statistical incorporation; these models include Monte Carlo simulation, the Master equation and the continuum equations (or semiconductor equations) [76,81,114]. We choose the semiconductor equations to continue our analysis which are posed as a drift-diffusion equation for each carrier coupled with the Poisson equation. These equations have been extensively solved in one-dimensional space through use of the Scharfetter-Gummel discretization with Gummel iteration and Newton's method [83,82,93,119]. In this technique, due to the non-linearity of the governing equations, the solution scheme involves ramping the applied potential to acquire self-consistent, intermediate solutions. We aim to attain useful results from simpler techniques.

In order to circumvent full numerical solution of the semiconductor equations, a large effort in literature has been placed on determining whether current behavior is controlled by injection resistance (injection limited) or bulk resistance (bulk limited) [77,66,131,100,137,138,109,125]. The appropriate current regime depends largely on the materials, device structure and thicknesses of the layers involved and, consequently, both limits have been widely reported in literature.

5.3.3 Requirements for injection limited treatment

The criterion required to satisfy bulk-limited, or space-charge limited (SCL), current is that the carrier injection must be capable of supplying sufficient charges to the bulk to force significant space-charge accumulation [125]. This coupling manifests itself in the Poisson equation which dictates how the scalar electric potential, ϕ , varies in the organic layer with space charge density [114]:

$$\nabla^2 \phi = -\frac{q}{\epsilon}(p - n) \quad 5.19$$

The potential of this device structure to produce sufficient injection to incur SCL effects is now analyzed. First, one-dimensional numerical continuum models for an SLPLED imposing Richardson-Schottky (RS) boundary conditions have concluded that for zero-field injection barriers greater than roughly 0.3-0.4eV, the injection will not produce surface electric field redistribution [114]. This criterion is extended into multiple dimensional space and a conservative comparison of the 0.4eV zero-field literature value is made with the calculated effective barrier height (Schottky lowered) along the device surface, $\Phi_{B,eff}(s)$, shown below:

$$\Phi_{B,eff}(s) = \Phi_{B,0} - q \sqrt{\frac{qE_s}{4\pi\epsilon}} \quad 5.20$$

where $\Phi_{B,0}$ is the zero-field injection barrier height at the electrode and E_s is the surface-normal electric field. From Equation 5.20, and considering a common operating condition of applied electric field of 10^6 V/cm (see Equation 5.22), the Schottky barrier lowering is roughly 0.22eV. In the forthcoming analysis, it is shown that the enhancement effects produced by the geometry lead to a maximum barrier reduction of roughly 0.20eV (Figure 5.9) compared to the base case device. UPS measurements show the zero-field energy barriers for ITO/NPB holes and Al/NPB electrons to be 1.35eV and 1.75eV, respectively [147,148]. Therefore, when considering the barrier shift resulting from the geometric modification, the net effective barrier height of the stronger injecting contact is still ~0.93eV and is much larger than the quoted literature value of 0.4eV zero-field barrier required to reach SCL effects. In addition, it should be noted that the study in Reference 114 utilizes the RS injection mechanism over the Scott-Malliaras (SM) injection mechanism which will be utilized in this work. The RS mechanism uses a larger effective injection rate than the SM mechanism; in effect, choosing the SM mechanism should shift transition to SCL to a smaller barrier height than the indicated value [114,115]. Furthermore, for the device in discussion, ITO/NPB/Al, the surface charge accumulation is incapable of redistributing the electric field at either electrode-organic contact.

5.3.4 Poisson Equation under injection limited conditions

Following from the analysis presented in the previous section (that is, accepting injection-limited behavior, or no carrier-related electric field redistribution resulting from accumulated interfacial carriers), the surface charge at the electrode-organic interface may be ignored in the computation of the electric potential. Since the space charge at the electrode-organic interfaces are expected to possess the highest spatial space-charge densities and, in these regions, are not significant enough to force electric field redistribution, internal electric field redistribution from space charge may also be neglected. Further, a carrier-free Poisson equation, or Laplace equation, may be used to analyze the electric field behavior of the geometrically modified OLED, which can be expressed as:

$$\nabla^2 \phi = 0 \quad 5.21$$

Ignoring the bias voltage to overcome the electrode work function offset, a voltage drop, ΔV , of 10V is taken over an organic layer of thickness, T_{org} of 100nm, which are common operating conditions. It follows that electric field for the baseline, planar device, E_0 is:

$$E_0 = \frac{\Delta V}{T_{org}} = \frac{10 \text{ V}}{100 \text{ nm}} = 10^6 \frac{\text{V}}{\text{cm}} \quad 5.22$$

Neumann (symmetry) boundary conditions are assigned to the horizontal edges of the minimum repetitive unit of the nanocolumn geometry in order to enforce periodic boundary conditions (Figure 5.4). The dimensions of column width and spacing in Figure 5.4 are based on the minimum physical period, which is then cut in half to find the minimum unit. A finite-difference scheme was implemented to obtain numerical solution for the electric potential.

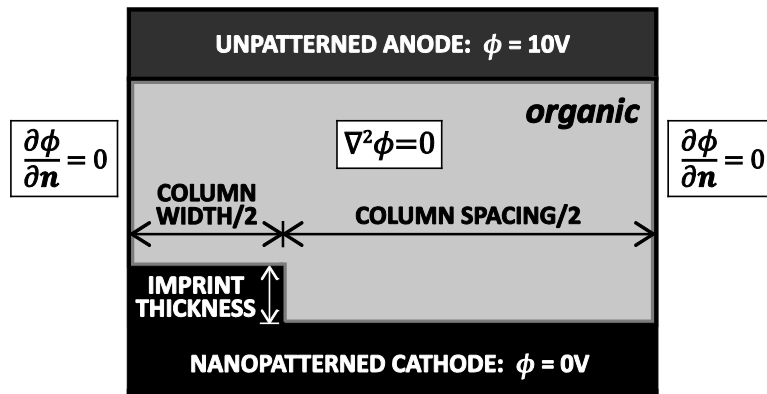


Figure 5.4: Minimum repetitive unit for nanocolumn array at cathode. Representation of the system of equations describing electric potential in the organic layer including domain and boundary conditions.

Following numerical solution of the electric potential in Equation 5.21, the surface-normal electric field along the surface of the cathode(anode), $E_{cath(an)}$ was determined through

numerical differentiation of electric potential as follows:

$$E_{cath(an)} = \mathbf{n}_{cath(an)} \cdot \nabla \phi \quad 5.23$$

where $\mathbf{n}_{cath(an)}$ is the vector surface normal at the cathode(anode) electrode.

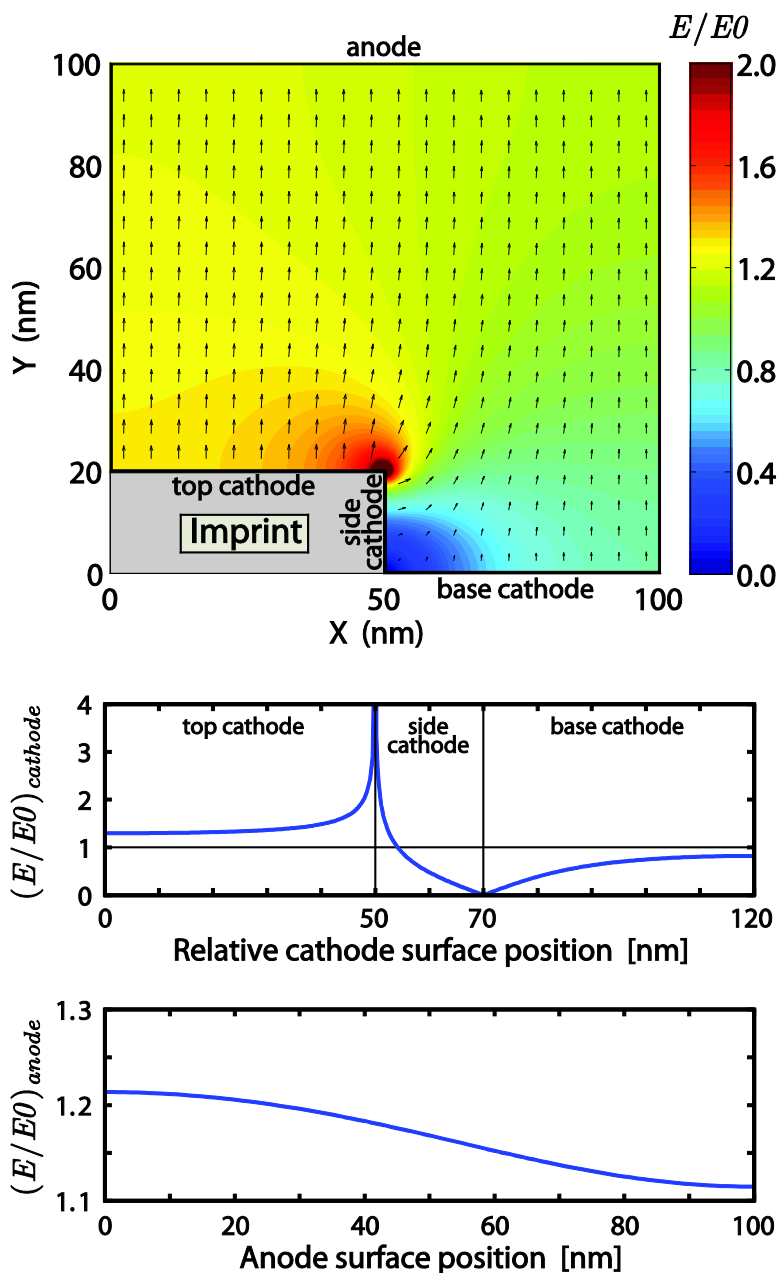


Figure 5.5: A map showing the electric field within the organic material after imprinting a column into the medium. In (A), electric field magnitude compared to baseline device; in (B), surface electric field enhancement along top of the imprinted column.

Figure 5.5A demonstrates how the magnitude of the vector electric field is modified in response to the nanostructuring of the cathode; it is shown that the magnitude becomes large at the interior corner of the imprinted geometry, facilitating electron injection and transport in this region. Figure 5.5B depicts the surface-normal electric field along the top of the imprinted column ("X_top_column" location is indicated on both plots). Please note that the electric field at a perfectly square imprinted corner approaches infinity. This situation is, of course, unphysical; therefore, a small fillet of radius 2\AA , is included at the corner at the corner of the imprint geometry; and, the fillet is removed from subsequent calculations since it causes the injection rates to diverge. Also, the fillet of the interior corner can also be used to represent the fidelity of the nanoimprinting process. We also note that the surface field results become somewhat independent of fillet radius at larger than 2nm.

5.3.5 Carrier-decoupled injection mechanism

The most appropriate analytical mechanism describing current injection at a metal-organic (including ITO/NPB) interface is the Scott-Malliaras (SM) mechanism [115]. This formalism asserts that carrier injection from an electrode into a low mobility organic medium occurs via a drift-controlled injection process with the interface recombination rate being controlled by a Langevin-type process. The injection rate bears exponential dependencies on zero-field barrier height and on the surface electric field, E . The Scott-Malliaras injection current density, J_{SM} is given below:

$$J_{SM} = 4\psi^2 Nq\mu E \exp\left(-\frac{\Phi_{B,0}}{kT}\right) \exp(f^{1/2}) \quad 5.24$$

$$\psi(f) = f^{-1} + f^{-1/2} - f^{-1}(1 + 2f^{1/2})^{1/2} \quad 5.25$$

$$f = \frac{qEr_c}{kT} \quad 5.26$$

$$r_c = \frac{q^2}{4\pi\epsilon kT} \quad 5.27$$

where r_c is the Coulomb radius of a surface image pair, N is the density of chargeable sites in the organic, μ is the carrier mobility of the injected charge in the organic material, k is the Boltzmann constant, T is temperature, f is the non-dimensional reduced electric field and ψ is a non-dimensional parameter [114,115]. It should be mentioned that this current injection equation utilizes a detailed balance to achieve a net injection rate. Therefore, the SM injection mechanism satisfies carrier decoupling of the charge injection process because it holds no dependence on the surface charge concentration. In this model, tunneling injection has been neglected since the device electric fields present in this work are not large enough to make tunneling the dominant current injection mechanism [137]. Furthermore, this set of equation leads to a carrier-decoupled framework.

In this scheme, the electric potential may be solved as previously defined in Equation 5.21, next, the surface electric field may be determined from Equation 5.23 and, then, the current injection rate can be found as a function of the surface electric field in Equations 5.24-5.27.

Finally, the majority injecting current densities may be found through surface integration analogous to Equation 5.2 with only the majority injection current densities in the integrand. We now transition to discussion on the carrier equations to complete the decoupled model.

5.3.6 Drift-diffusion equations

In this section, the carrier equations are revisited. The transient drift-diffusion equations are presented below:

$$\frac{\partial n}{\partial t} - \frac{1}{q} \nabla \cdot \mathbf{J}_n = -R \quad 5.28$$

$$\frac{\partial p}{\partial t} + \frac{1}{q} \nabla \cdot \mathbf{J}_p = -R \quad 5.29$$

$$\mathbf{J}_n = \mathbf{J}_{n,\text{drift}} + \mathbf{J}_{n,\text{diff}} = q\mu_n n \mathbf{E} + kT\mu_n \nabla n \quad 5.30$$

$$\mathbf{J}_p = \mathbf{J}_{p,\text{drift}} + \mathbf{J}_{p,\text{diff}} = q\mu_p p \mathbf{E} - kT\mu_p \nabla p \quad 5.31$$

where Equations 5.28-5.29 are the carrier drift-diffusion relations in terms of local vector carrier current densities, $\mathbf{J}_n(\mathbf{J}_p)$. R and γnp are, respectively, the recombination rate and recombination factor introduced in Equations 5.4 and 5.5. Equations 5.30 and 5.31 express the total carrier current densities in terms of drift and diffusion components, identified with corresponding subscripts. For the specific organic material considered in this work it is recognized that the carrier mobilities are similar, therefore, we include only a single mobility term in the coming analysis.

5.3.7 Determination of electric field streamlines

We proceed by choosing equally-spaced points on the surface of the patterned cathode and step along the direction of the recently-solved electric field lines to achieve a number of streamlines. Mathematically, the pathway-specific streamline, r_i , is found as:

$$\mathbf{r}_i^{j+1} = \mathbf{r}_i^j + \frac{\mathbf{E}_i^j}{\|\mathbf{E}_i^j\|} \times \Delta r \quad 5.32$$

where \mathbf{r}_i^j is a vector describing the streamline points, \mathbf{E}_i^j is the electric field at the current streamline point and Δr is step length taken along the streamline direction. The streamlines determined are shown below in Figure 5.6. Notice that as can be expected regions near the interior corner, which possess larger electric fields, sweep out larger anode surface than regions near the bottom corner, which possess smaller electric fields. The resulting streamlines constitute the maximum gradient of the electric potential and thus no electric field exists in a direction orthogonal to the streamlines, a characteristic which will be revisited momentarily.

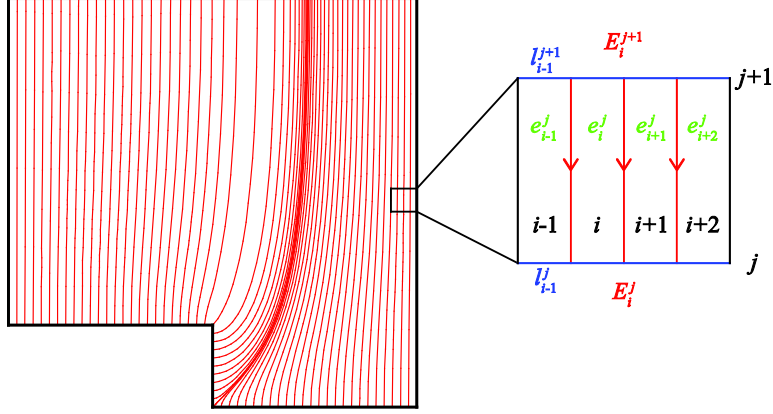


Figure 5.6: Streamline formulation utilized throughout analysis section. l is the streamline width, E is the streamline electric field, i is the streamline index and j is a discrete element along the streamline. e is an element located in stream i and is the j^{th} element along the streamline starting at the cathode.

5.3.8 Cross-streamline diffusion analysis

We next examine the relative influence of cross-streamline diffusion current. Setting the SM injection current density equal to the surface drift current leads to the following prediction of the surface charge density, n_{SM} [115]:

$$n_{SM} = 4\psi^2 N \exp\left(-\frac{\Phi_{B,0}}{kT}\right) \exp(\sqrt{f}) \quad 5.33$$

As per Equation 5.32, the surface carrier concentration is exponentially related to the surface electric field. Therefore, since diffusion is related to the gradient of the carrier concentration, the surface region with the most rapidly changing electric field will have the largest diffusion current. This condition occurs at the interior corner; further, we examine the ratio of the diffusion current to the drift current at this location to establish the significance of the diffusion current contribution. The cathode electron surface diffusion current, $J_{n,diff}^{cath}$ can be found from the cathode-electron surface carrier concentration gradient, as shown below:

$$J_{n,diff}^{cath} = kT\mu \frac{\partial n_{SM}^{cath}}{\partial s_{cath}} \quad 5.34$$

where s_{cath} is the cathode surface direction. The values required for Equation 5.33 can be extracted from Figure 5.5B. It is determined that the surface electric field increases by roughly 10^6 V/cm within 1nm from the interior corner. From Equation 5.32, and noting that ψ is a relatively weak function of electric field, the relative diffusion-to-drift current density effects may be approximated as follows:

$$\left| \frac{J_{n,diff}^{cath}}{J_{n,i}^{cath}} \right| = \frac{kT}{q} \times \frac{1}{E_{cath}} \times \frac{\partial \ln(n_{SM}^{cath})}{\partial s_{cath}} \quad 5.35$$

Equations 5.26 and 5.27 are then used to reduce the right–most term above with discretized variables in Figure 5.6 as displayed below:

$$\left| \frac{J_{n,diff}^{cath}}{J_{n,i}^{cath}} \right| \approx \frac{\sqrt{V_T r_c}}{C_i} \times \left| \sqrt{E_{ic}^{cath}} - \sqrt{E_{ic-1}^{cath}} \right| \quad 5.36$$

where V_T is thermal voltage, r_c is the Coulomb radius of a surface image pair in Equation 5.26, the subscript ic refers to the evaluation of the discretized points neighboring the inner corner and C_i is the pathway-specific electric flux. The result in Equation 5.36 is that the diffusion component contribution is less than ten percent of the drift component. It should be noted that any electrons leaving one streamline equivalently lead to increased injection rate in the streamline to which they enter. Therefore, the cross-streamline diffusion will not affect the overall metric computed, but will lead to slight errors in the individual streamline enhancement factors. Additionally, the influence of the cross-streamline diffusion effect is expected to be mediated by choosing wider streamlines since the surface diffusion effect drops off geometrically from the corner. Further, the diffusion component is neglected from further analysis. One-dimensional approximations for single-layer devices have concluded neglecting diffusion to be valid under larger applied voltages and under injection limited cases [151]. The reduction of the system of equations to a drift-only system allows for a semi-analytical numerical solution to arise.

5.3.9 Formulation of streamline analysis

As previously stated, the streamlines constitute the maximum gradient of the electric potential; therefore, under the drift-only approximation, current flows in the streamline direction only. Under these conditions, the streamlines possess the following pathway-specific characteristics:

$$E_i^{cath} \times l_i^{cath} = E_i^{an} \times l_i^{an} = E_i^j \times l_i^j = C_i \quad 5.37$$

$$(n + p)_i^{cath} = (n + p)_i^{an} = (n + p)_i^j = N_i \quad 5.38$$

where i is the streamline index, l is the streamline width and j is a discrete element along the streamline (see Figure 5.6). Above, Equation 5.37, follows from Equation 5.21 and no electric potential flux along streamline edges; Equation 5.38 follows from Equation 5.37 and the drift-only approximation. In Equation 5.37, C_i is the pathway-specific electric flux. In Equation 5.38, N_i is the pathway-specific, summed carrier density of both electron and hole species.

We next conduct a continuum analysis of the electron current from Equation 5.28 about an arbitrary differential element on flow path i . We expand the electron current term along the streamline direction from Equation 5.30 and substitute the recombination terms from Equations 5.3-5.5, which leads to the following equation:

$$\mu \frac{d(nEl)}{ds} ds = -\gamma np dA_i \quad 5.39$$

where, above, we choose to remove the element indexes i and j where they are understood to be local components described by the differential equation and preserve i where it is known to be a constant property of the streamline, e.g. C_i , A_i and N_i . In the above equation, it is recognized that the product of electric field and streamline width is the streamline electric flux constant in Equation 5.37, producing the reduced form:

$$\mu C_i \frac{dn}{ds} ds = -\gamma np dA_i \quad 5.40$$

We cast Equation 5.40 in separable differential form as:

$$\frac{dn}{n \times p} = -\frac{\gamma}{\mu} \frac{1}{C_i} dA_i \approx -\frac{2q}{\varepsilon C_i} dA_i \quad 5.41$$

where n and p describe how the carrier concentrations change along the streamline, C_i is a constant specific to the streamline (from Equation 5.37, above) and dA_i is the area swept by the differential element. The left-hand side of Equation 5.41 may be rewritten using Equation 5.38 and partial fraction decomposition, resulting in the respective expression progression below:

$$\frac{dn}{n \times p} = \frac{dn}{n \times [N_i - n]} = \left(\frac{1}{N_i}\right) dn \left[\frac{1}{n} + \frac{1}{N_i - n}\right] \quad 5.42$$

For separable systems it is more convenient to in cast the expression in Equation 5.42 as a full differential to simplify future integration, this results in the following expression:

$$\frac{dn}{n \times p} = \frac{1}{N_i} \times d \ln \left[\frac{n}{N_i - n} \right] \quad 5.43$$

Evaluation of the substitution of Equation 5.43 into Equation 5.41, produces the following result:

$$\frac{1}{N_i} \times \int_{s=0}^{s=S_i} \frac{an}{cath} d \ln \left[\frac{n}{N_i - n} \right] = -\frac{2q}{\varepsilon C_i} \times \int_{s=0}^{s=S_i} \frac{an}{cath} dA_i \quad 5.44$$

where S_i is the total streamline length swept by the integral from the cathode to the anode side. After some further logarithm manipulation, the above equation leads to the following relation of carrier concentrations:

$$n_i^{an} \times p_i^{cath} = n_i^{cath} \times p_i^{an} \times \exp\left(-\frac{2q N_i}{\epsilon C_i} A_i\right) \quad 5.45$$

where, above, the total area swept along the streamline, A_i , can be computed using trapezoidal approximation of the discretized elements as:

$$A_i^j = (\mathbf{l} \times \Delta \mathbf{s})_i^j = (l \sin \theta \Delta s)_i^j \quad 5.46$$

where \mathbf{l}_i^j is a vector streamline width and $\Delta \mathbf{s}_i^j$ is a vector differential step taken along the streamline path. Alternatively, θ_i^j , the angle between vectors \mathbf{l}_i^j and $\Delta \mathbf{s}_i^j$, may be found as intermediate step to calculating the element area, A_i^j . The total area swept may be found as the summation of all element areas as follows:

$$A_i = \sum_j A_i^j \quad 5.47$$

Next, Equation 5.45 is placed in terms of currents rather than carrier concentrations. An example equation used to convert cathode electron carrier concentration to cathode electron current is given below:

$$I_{n,i}^{cath} = q\mu C_i n_i^{cath} \quad 5.48$$

Equations 5.45 and 5.48 are then combined to arrive at:

$$\frac{I_{tot,i} - I_{n,i}^{cath}}{I_{n,i}^{cath}} \times \frac{I_{tot,i} - I_{p,i}^{an}}{I_{p,i}^{an}} = \exp\left(-\frac{2 A_i}{\mu \epsilon C_i^2} I_{tot,i}\right) \quad 5.49$$

where, in the above equation, all values have been computed from geometry and the previous solution of Equation 5.21 except $I_{tot,i}$. We note that since the result of an analogous analysis on Equation 5.29 leads to an equivalent equation and two carrier concentrations remain unknown, we resort to non-linear methods to solve Equation 5.49. We write out the implicit formula describing the total current below:

$$I_{tot,i} = \frac{1}{2} \left((I_{p,i}^{an} + I_{n,i}^{cath}) + \sqrt{(I_{p,i}^{an} - I_{n,i}^{cath})^2 + 4I_{an,i}^p I_{cath,i}^n \exp\left(-\frac{2 A_i}{\mu \epsilon C_i^2} I_{tot,i}\right)} \right) \quad 5.50$$

where, in Equation 5.50, the expected current limits for $I_{tot,i}$ are met. The solution of the total pathway current completes solution to the set of variables that were previously set out to attain.

5.4 Results and Discussion

5.4.1 Injection current enhancement

The local pathway-specific current enhancement ratio, $F_{I_{n,i}^{cath}}$, may be found as the ratio of the pathway-specific carrier injection current to the baseline injection current as follows:

$$F_{I_{n,i}^{cath}} = \frac{I_{n,i}^{cath}}{I_0^{cath}} = \frac{J_{SM}(E_i^{cath})|_n^{cath}}{J_{SM}(E_0)|_n^{cath}} \quad 5.51$$

where J_{SM} is computed from Equations 5.24-5.27. In going from the middle to right expressions above, we have assumed equivalent injecting surface areas; the discrepancy in the overall current brought about by assuming equivalent injection surface areas will be remedied in the following computation. The overall level of injecting current enhancement at the cathode-patterned surface can be determined from summation over all the current pathways in the following equation:

$$\bar{F}_{I_{n,i}^{cath}} = \frac{\sum_i (F_{I_{n,i}^{cath}} \times l_i^{cath})}{l_{proj}} \quad 5.52$$

where $\bar{F}_{I_{n,i}^{cath}}$ is the overall electron current injection enhancement factor at the cathode, l_i^{cath} is the surface injection width for nanostructured geometry at the cathode surfaces contributing to electron injection and l_{proj} is the total injection area for the comparable planar injecting electrode. An analogous enhancement factor may be computed over the unpatterned anode for hole injection from Equation 5.52. Figure 5.7 displays the results of the injecting current enhancement factors for both the cathode-organic (patterned) and anode-organic (unpatterned) sides resulting from various nanoimprinted-cathode geometries.

The results in Figure 5.7 demonstrate the strongly asymmetrical current enhancement behavior resulting from this modification. The overall cathode-side current injection enhancement is, for some geometries, one to two orders of magnitude larger than the overall anode-side current injection enhancement. In order to further investigate the effects to the SLOLED device, we isolate a specific geometric condition chosen to promote the asymmetry of the injection currents. The geometry chosen is the $\bar{F}_{I_{n,i}^{cath}}$ -optimized values in Figure 5.7 (demarcated by black dots) with nanoimprint width of 100nm and imprint thickness of 20nm, which is optimized at a spacing of 100nm. The overall injection current enhancement factors for electrons and holes are 34.98 and 2.06, respectively. This geometric condition will be used in the forthcoming analysis to study the impact of the geometric modifications on a variety of efficiency metrics.

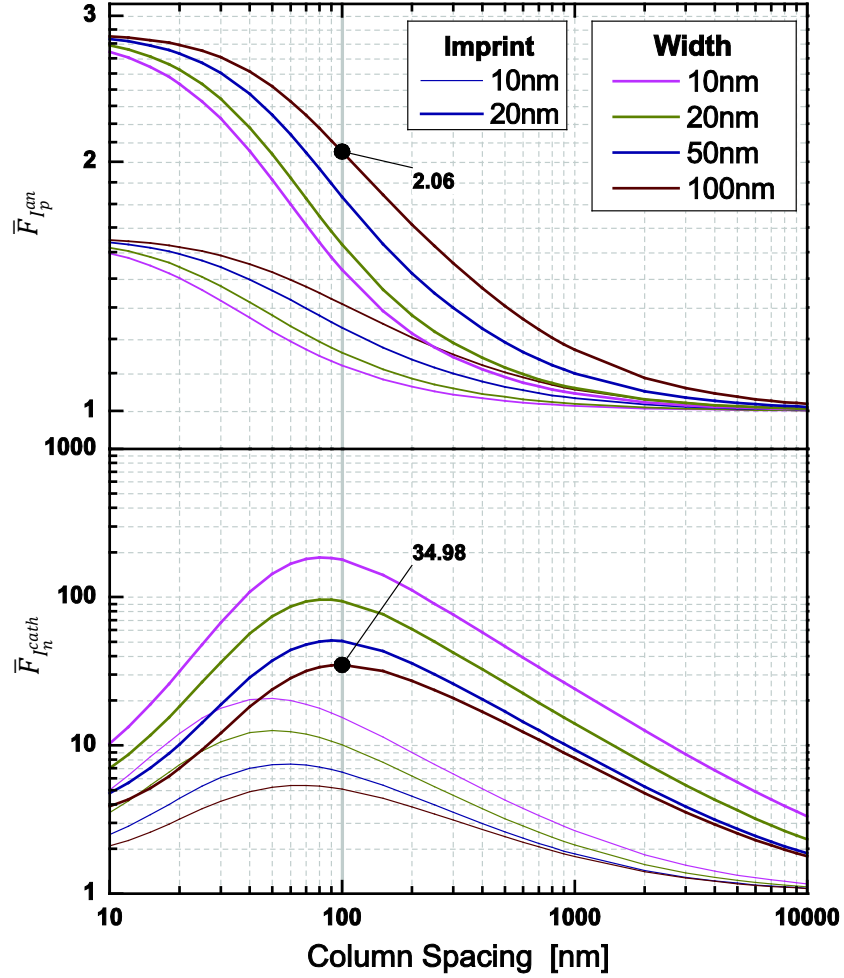


Figure 5.7: Average carrier current enhancement factors due to the incorporation of nanoscale column structures at the cathode interface. At top, the anode holes current enhancement factor; at bottom, the cathode electrons current enhancement factor. The inserted dots represent the optimized conditions used in forthcoming analysis.

5.4.2 Total current enhancement

Just as the individual carrier injection is improved by the nanopatterning, so is the total current improved. The resulting pathway current enhancement, $F_{I_{tot,i}}$, is described by the equation below:

$$F_{I_{tot,i}} = \frac{I_{tot,i}}{J_{tot,0} \times l_i^{an}} \quad 5.53$$

where, the choice to include the anode streamline width to compute the baseline current is chosen because it allows us to retain the original surface area defined by the surface electrode projection. The resulting pathway current enhancement factors are depicted in the colormap in [Figure 5.8](#). The total current enhancement factor, $\bar{F}_{I_{tot}}$, can then be determined from

Equations 5.13, 5.14 and 5.50, as follows:

$$\bar{F}_{I_{tot}} = \frac{\sum_i (I_{tot,i} \times l_i^{an})}{\sum_i l_i^{an}} \quad 5.54$$

The computed overall current enhancement, $\bar{F}_{I_{tot}}$, for the device considered is found to be 2.06. It should be expected that for cases where the current balance is much less than one from unbalanced injection that, according to Equation 5.11, the total current enhancement should be nearly that of the overall enhancement to the majority injection current, depicted in Figure 5.7.

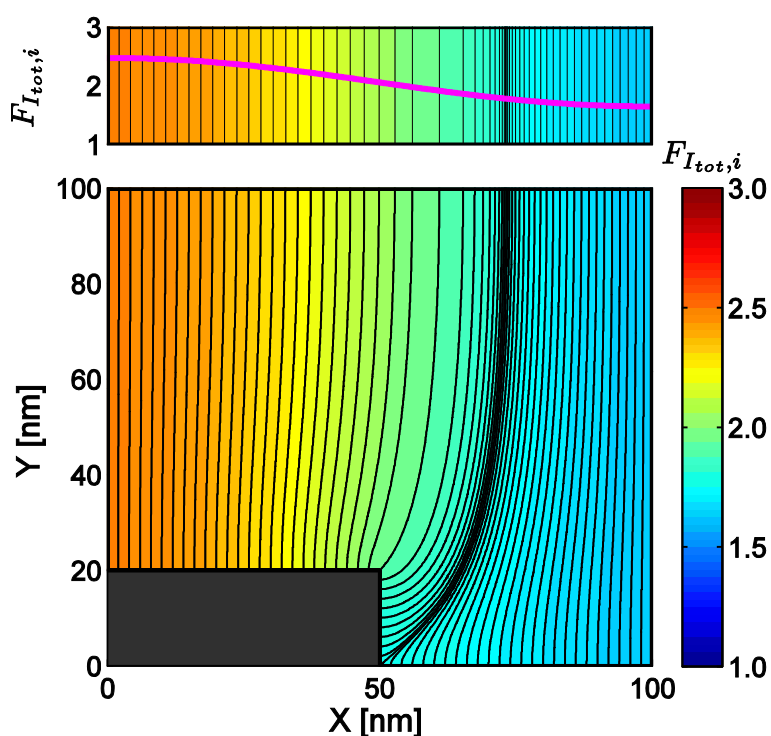


Figure 5.8: (Bottom) Colormap of streamline total current enhancement factor, $F_{I_{tot},i} (= I_{tot,i}/I_{tot,0})$. Following from the dominant hole carrier injection current and the largest electric field enhancement occurring at the left side of the anode surface, the current is improved by the largest amount in the left-most streamlines. (Top) Anode-organic interface profile of the total current enhancement factor with superposed streamline colormap.

5.4.3 Current injection balance

As shown in Figure 5.7, nanopatterning of the electrode-organic interface lead to asymmetrical modifications to the carrier injection characteristics. Since the patterning effect predominantly benefits current injection on the patterned side which also corresponds to the injection-deficient contact, this technique can be used to improve current injection balance. We

now analyze the influence of the nanopatterned interface on current balance.

As previously discussed, even though an organic material may have ambipolar mobilities, e.g. NPB, the injection rates from the electrode-organic interfaces are in general very dissimilar. In Equation 5.7, current injection balance has been written in terms of the injecting carrier currents (i.e., the ratio of weaker injecting carrier current to the stronger injecting carrier current). Through incorporation of the SM injection mechanism from Equations 5.24-5.27, the previously defined carrier current enhancement factors from Equation 5.51, the hole-only nature of the device structure and neglecting the Poole-Frankel mobility effect for simplicity, the pathway current balance, $\eta_{bal,i}$, can be rewritten as:

$$\eta_{bal,i} = \frac{I_{n,i}^{cath}}{I_{p,i}^{an}} = \frac{\exp(-\Phi_{B,0}^{cath}/kT)}{\exp(-\Phi_{B,0}^{an}/kT)} \times \frac{F_{I_{n,i}^{cath}}}{F_{I_{p,i}^{an}}} \times \frac{l_i^{cath}}{l_i^{an}} \quad 5.55$$

where in the right-most expression above, all remaining factors (ψ , f and E) of the injection mechanism have already been included in the individual current enhancement factors Equation 5.51. It is apparent from the results of in Figure 5.7 that, when the nanoimprinting modification is applied to the weaker injecting electrode-organic interface, current balance is promoted through compensation of the minority carrier injection rate.

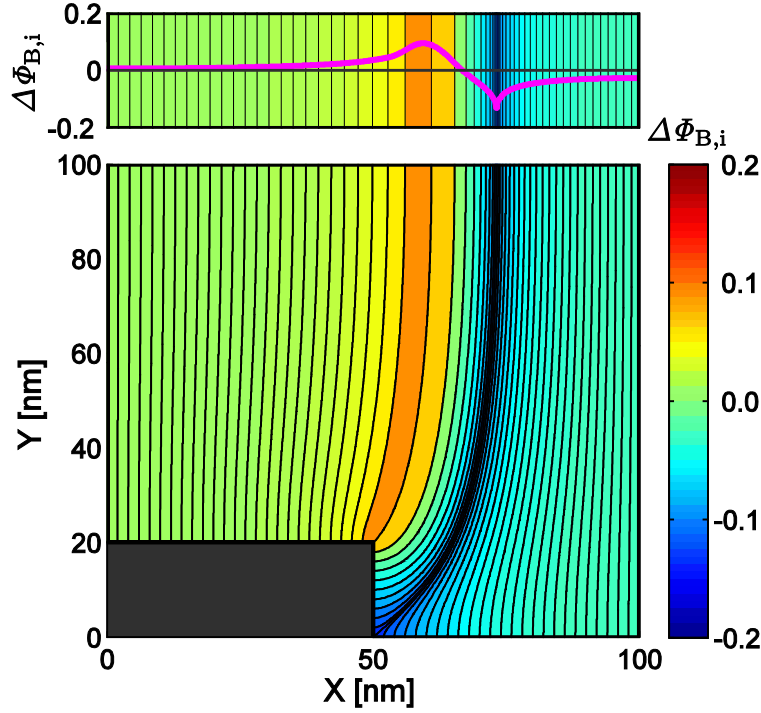


Figure 5.9: (Bottom) Colormap showing the shift in effective barrier height, $\Delta\Phi_{B,i}(= \Phi_{B,eff}^{cath} - \Phi_{B,eff}^{an})$ [eV]. The effects are most pronounced on the interior and exterior corners of the geometry, where the barrier shift leads to excess concentrations of electrons and holes along the streamline, respectively. (Top) Anode-organic interface profile of the effective barrier height shift with superposed streamline colormap.

We now revisit the ITO/NPB/Al hole-only device, experimental UPS values indicate that the difference in injection-barrier heights is 0.40eV (although these values are highly dependent on surface preparation). Additionally, the carrier mobilities are roughly equal. We are interested in determining by how much the optimized barrier height difference is altered by the nanoimprinted structure. The pathway-specific injection barrier shift, $\Delta\Phi_{B,i}$, can be found from:

$$\Delta\Phi_{B,i} = kT \ln \left[\frac{F_{I_{n,i}^{cath}}}{F_{I_{p,i}^{an}}} \times \frac{l_i^{cath}}{l_i^{an}} \right] \quad 5.56$$

Figure 5.9 below shows a colormap of the effective barrier shifts due to the geometric nature of the nanopatterning. The electric field streamlines emanating from the top (interior) corner of the organic produce roughly 0.2eV effective barrier shift introducing excess electron concentrations; whereas, the effective barrier on the bottom (exterior) corner of the imprint experiences roughly -0.2eV shift introducing excess hole concentrations along the electric field streamlines.

The overall current balance enhancement factor, \bar{F}_{bal} , may be found from Equations 5.13-5.14. For the specified geometry, the computed current balance enhancement factor is 3.53.

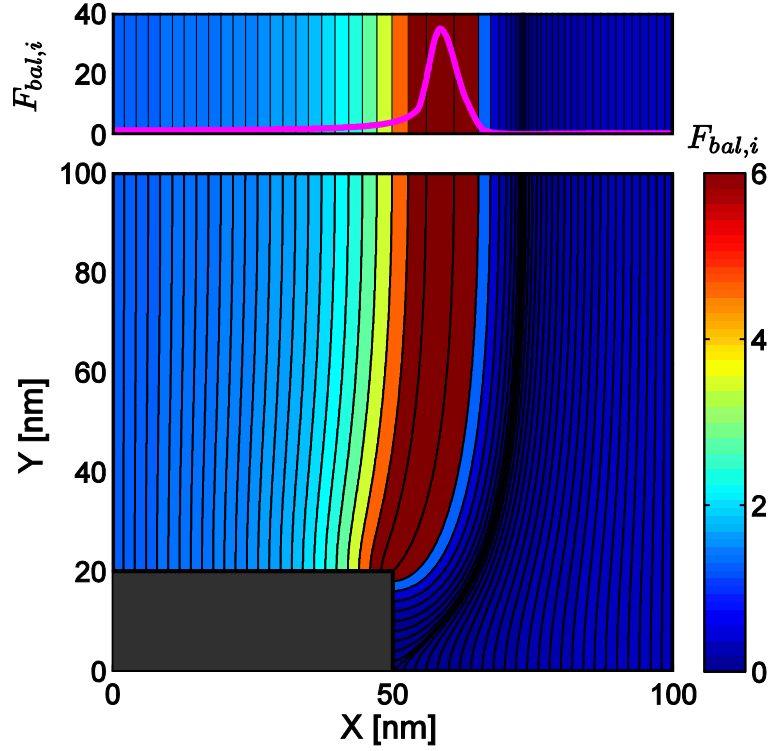


Figure 5.10: (Bottom) Colormap showing pathway current balance enhancement factor, $F_{bal,i}$. Due to the effective barrier height shift in the left-most current pathways, as seen in Figure 5.9, the improvement in electron injection leads to substantial enhancements in current injection balance. (Top) Anode-organic interface profile of the current injection balance factor with superposed streamline colormap.

5.4.4 Carrier confinement

Carrier confinement is also modified by the geometric structure. We begin by considering an approximation to the second term in Equation 5.50 in the limit of a low current balance factor (applicable for a wide range of cases where $\eta_{bal,i} < 0.3$) upon implementing Taylor series expansion we produce the following equation:

$$I_{tot,i} = I_{p,i}^{an} + I_{n,i}^{cath} \exp\left(-\frac{2 A_i}{\mu\epsilon C_i^2} I_{tot,i}\right) \quad 5.57$$

Next, we notice the resemblance of the above equation with Equation 5.11 and develop an equivalent relation expressing the pathway carrier confinement efficiency, shown below:

$$\eta_{cnf,i} = 1 - \exp\left(-\frac{2 A_i}{\mu\epsilon C_i^2} I_{tot,i}\right) \quad 5.58$$

where, in the expression within the exponential above, we recognize from Equation 5.24, the exponential dependence on the barrier height leads to a very small absolute term appearing in the exponential. That is due to the large injection barrier height, large electric fields and thin films, relatively few carriers have a chance to recombine before being extracted. From Taylor expansion we arrive at the following approximation:

$$\eta_{cnf,i} \approx \frac{2}{\mu \varepsilon} \frac{A_i}{C_i^2} I_{tot,i} \quad 5.59$$

A colormap depicting the computed pathway confinement enhancement, $F_{cnf,i}$, results are for the sampled geometry are shown in Figure 5.11. The largest carrier confinement enhancement is reported in the regions near the exterior corner. From Equations 5.13 and 5.14, the overall carrier confinement enhancement factor, \bar{F}_{cnf} , is found to be 1.32.

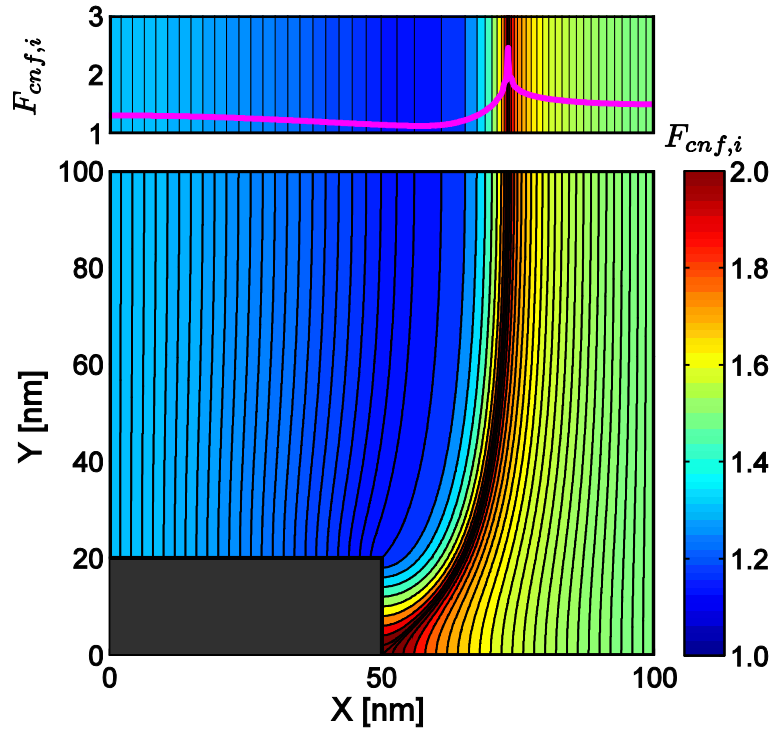


Figure 5.11: (Bottom) Colormap of the streamline confinement enhancement factor, $F_{cnf,i}(= \eta_{cnf,i}/\eta_{cnf,0})$. Carrier confinement is improved in regions having low ratios of pathway current density to electric field. In such regions, where carrier velocity is slow, carriers are allowed more opportunity to find counter-carriers, thus promoting recombination. (Top) Anode-organic interface profile of the confinement enhancement factor with superposed streamline colormap.

5.4.5 Recombination efficiency

The pathway recombination efficiency enhancement, $F_{rec,i}$, can be computed from

Equations 5.12-5.14 and is depicted in Figure 5.12. The results suggest high recombination enhancement near the interior corner. The overall enhancement factor, \bar{F}_{rec} , from the geometric modification is computed to be 4.13.

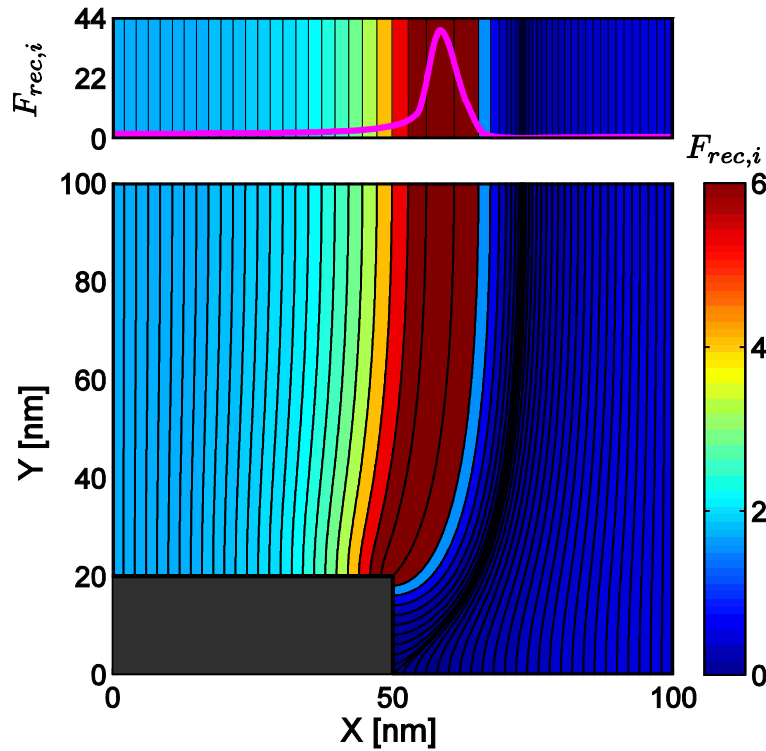


Figure 5.12: Colormap of streamline overall recombination efficiency enhancement factor, $F_{rec,i}(= \eta_{rec,i}/\eta_{rec,0})$. Recombination efficiency, as defined through Equation 5.12, is related to the product of the current balance efficiency and the confinement efficiency. Therefore, the regions demonstrating the largest enhancement in pathway recombination efficiency are near the interior corner due to the enhancement in current balance over these streamlines. (Top) Anode-organic interface profile of the confinement enhancement factor with superposed streamline colormap.

5.4.6 Influence of effective thickness reduction

Until now the effects of the current enhancement have been removed from the current-weighting. If we were to approximate the total recombination or luminance enhancement from the surface modification, the appropriate figure of merit should be the product of recombination enhancement and current enhancement. However, an important aspect of the modification is that it serves to reduce the effective thickness of the organic layer thereby increasing the overall electric field. In other words, to place the enhancement effects on equal footing with simply reducing the device thickness, we should compare the device with that of a planar device which has equally reduced thickness. Since we now know the total current enhancement factor is 2.06, we may use the results from Equation 5.50 for a planar device to

invert the current enhancement ratio and find that the effective electric field enhancement for the geometrically modified device is 17% which translates to an effective thickness of 85.5nm. Further, when compared to a planar device of thickness 80nm, which is the minimum thickness of the patterned structure, the overall recombination enhancement is shown to be 5.71. Therefore, the modification shows significant recombination improvement even over an equivalently reduced thickness device, again in support of the proposed design strategy.

5.5 Comparison with experiments

The methods for device fabrication and device characterization are given in [Appendix C](#). Previous experimental results from our research group on the nanopatterning effect of a similar nanopatterned cathode device may be found in [\[143\]](#). Using the numerical model, the device current and luminance enhancement results are compared with our previous experimental results. In the following two figures ([Figure 5.13](#) and [Figure 5.14](#)), the device structure: Al/MEH-PPV/PEDOT:PSS/ITO is modeled with 100nm MEH-PPV layer, a 1 μ m half-pitch nanoimprint pattern and a 10nm nanoimprint thickness. The results show comparable enhancement to results predicted by the model.

[Figure 5.13](#) show similar current enhancement over a wide range of applied voltages. Of course, the experimental nanopatterned version from literature will not have perfect corner fidelity, reducing the level of current enhancement.

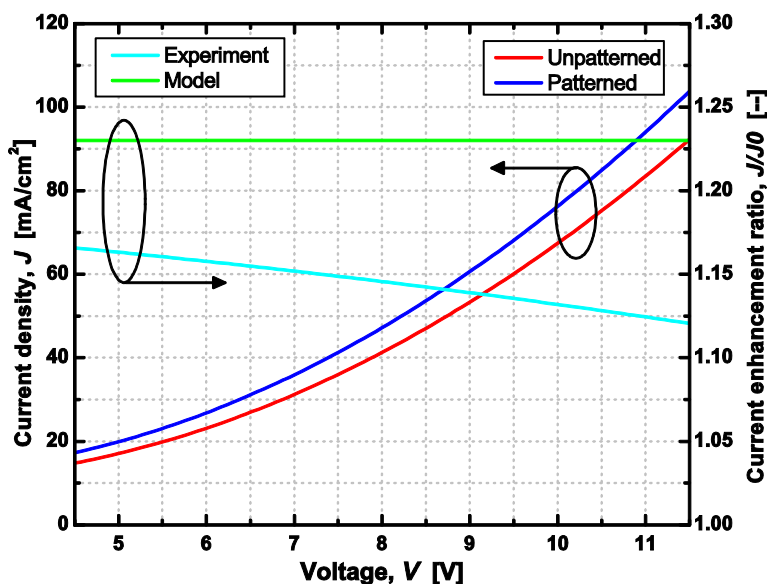


Figure 5.13: Comparison of numerical model and experimental (from [\[143\]](#)) current enhancement results of nanopatterned PLED with structure: Al/MEH-PPV/PEDOT:PSS/ITO.

The experimental results in [Figure 5.14](#) demonstrate the ability for luminance enhancement. This enhancement results primarily from electrical enhancement effects brought about by the patterning of organic layers [\[143\]](#). The results show the favorable luminance

enhancement characteristics of approximately 70% luminance improvement brought about by nanopatterning. The results from Figure 5.14 show the comparison of the predicted luminance enhancement factor from the model developed above. Good agreement is again shown towards the larger applied potential values.

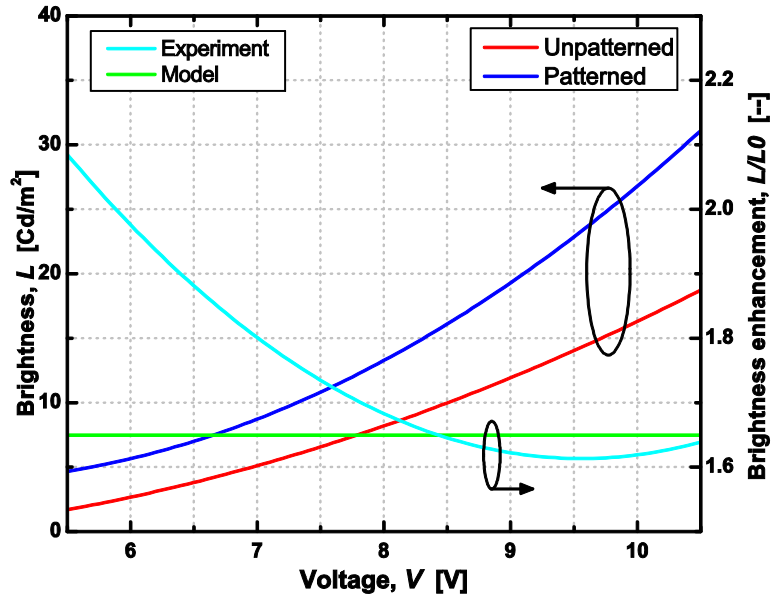


Figure 5.14: Comparison of numerical model and experimental (from [143]) luminance enhancement results of nanopatterned PLED with structure: Al/MEH-PPV/PEDOT:PSS/ITO.

5.6 Geometrically-optimized enhancement from model

The model developed in Sections 5.3-5.4 is now extended to show the enhancement factor trends over a range of geometries for the nanopatterned column geometry (Figure 5.15). Figure 5.15 depicts the geometric *width*, *spacing* and *height* parameters of the nanocolumns that are used to specify the geometry of interest below. The nanopattern *half-pitch* discussed below is equivalent to the sum of the width and spacing. In the following analysis, the computed geometries that are considered have width-to-spacing ratios of unity.

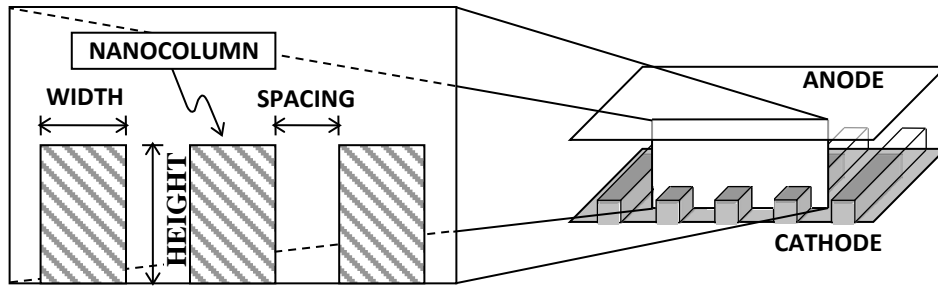


Figure 5.15: Schematic showing dimensions of the nanoimprint press process applied to cathode, producing nanocolumn impressions at the cathode-organic interface.

In this section, the overall enhancement effects are determined over a range of widths. The results of the geometry sweeps are shown below in [Figures 5.16-5.21](#). The main features are demonstrated by the colormaps below over the range of geometries. These figures show that the enhancement effects are most prominent when the half-pitch width length scale is small and the imprint thickness length scale is large. As the half-pitch length scale is decreased (say <10nm), the carrier transport becomes dominated by the imprint-thickness-reduced section where the field-enhancement effects are large. This is shown by the low fractional area of the current paths originating from the cathode which reach the anode, which quickly decreases when reducing the half-pitch length scale. Other important considerations also limit the practical usefulness of a low half-pitch length scale such as nanoimprint fidelity and molecular lifetime (from high field). Conversely, the reduced benefits from using micrometer length scale imprints are reduced electrical efficiency enhancement benefits. Therefore, an intermediate nanoimprint half-pitch of ~100nm is recommended for ideal electrical enhancement.

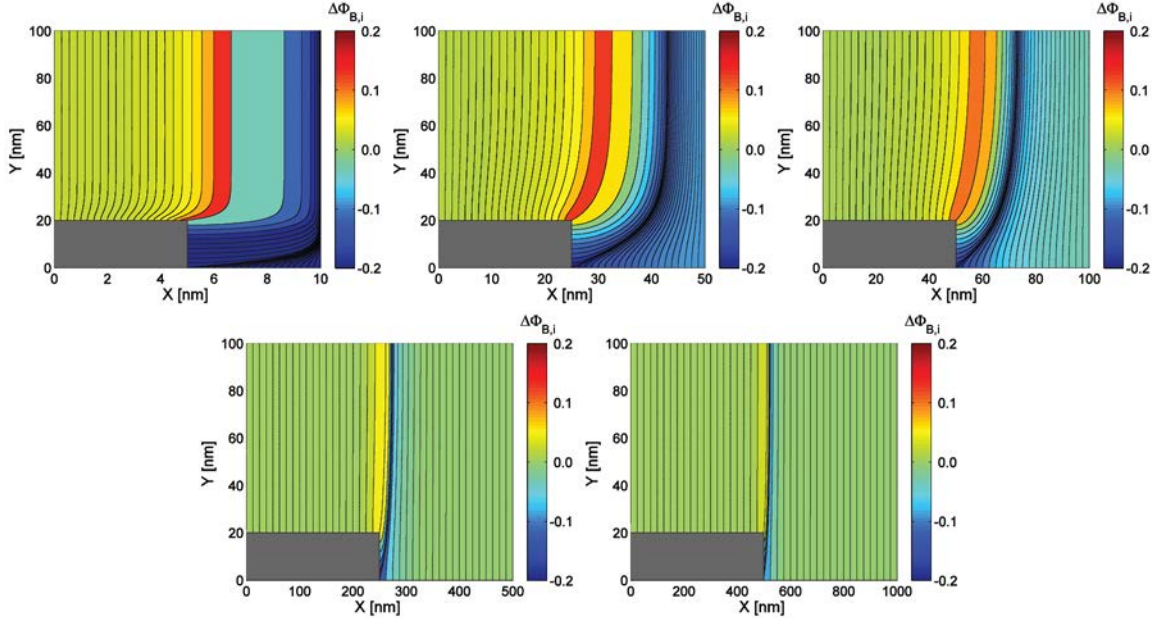


Figure 5.16: Barrier height shifts, $\Delta\Phi_{B,i}$, for the orders of magnitude patterning dimension. The half-pitch dimensions are 10, 50, 100, 500, 1000 nm, respectively.

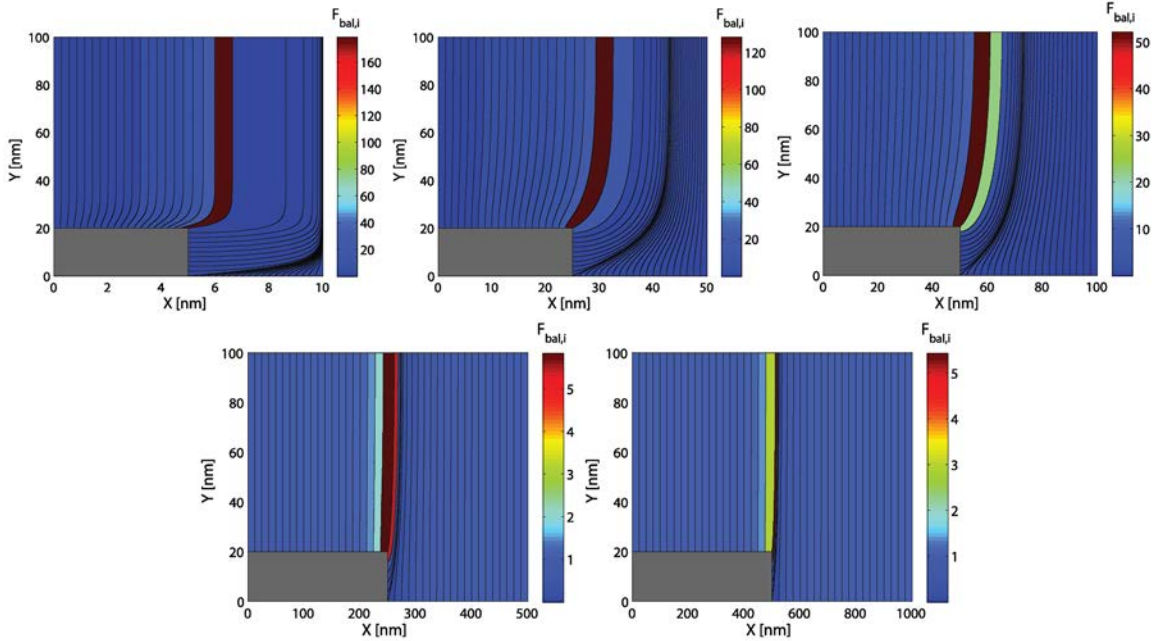


Figure 5.17: Balance current enhancement factor, $F_{bal,i}$ over the nm- μ m length scales. The half-pitch dimensions are 10, 50, 100, 500, 1000 nm, respectively.

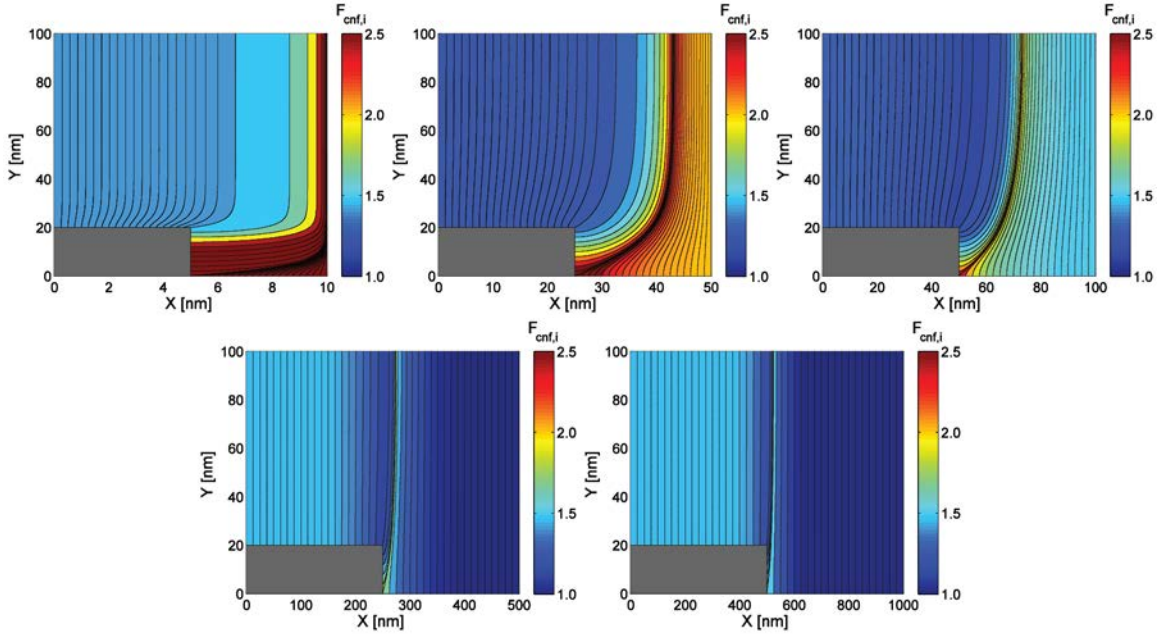


Figure 5.18: Confinement enhancement factor, $F_{cnf,i}$ over the nm- μ m length scales. The half-pitch dimensions are 10, 50, 100, 500, 1000 nm, respectively.

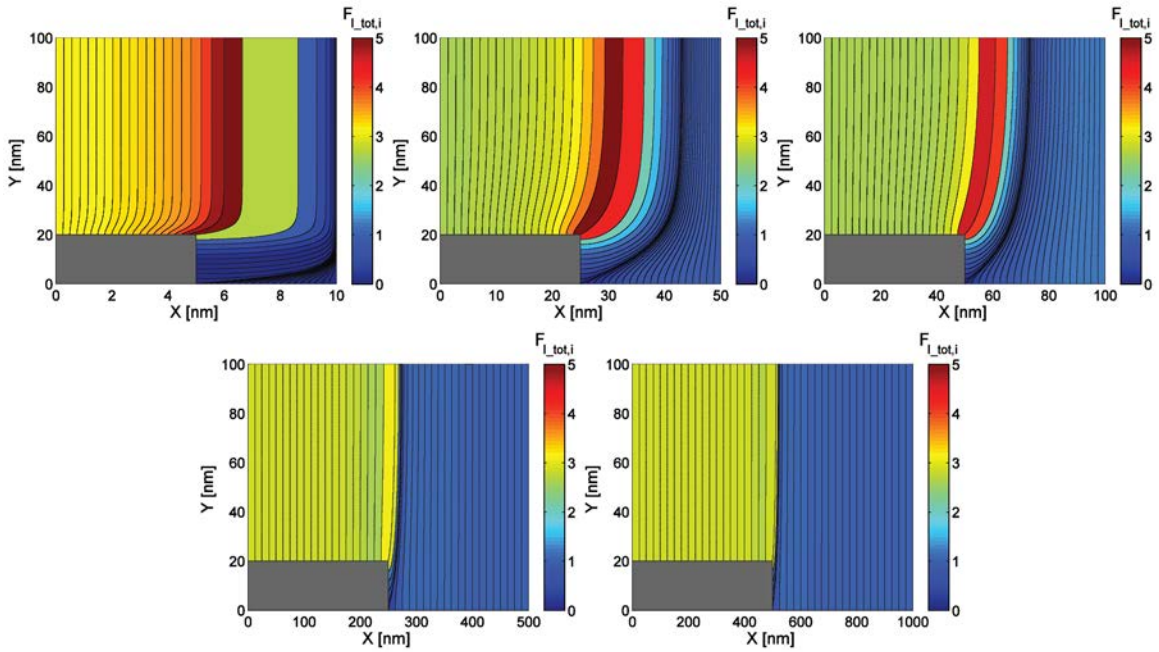


Figure 5.19: Overall current enhancement factor, $F_{I_{tot},i}$ the nm- μ m length scales. The half-pitch dimensions are 10, 50, 100, 500, 1000 nm, respectively.

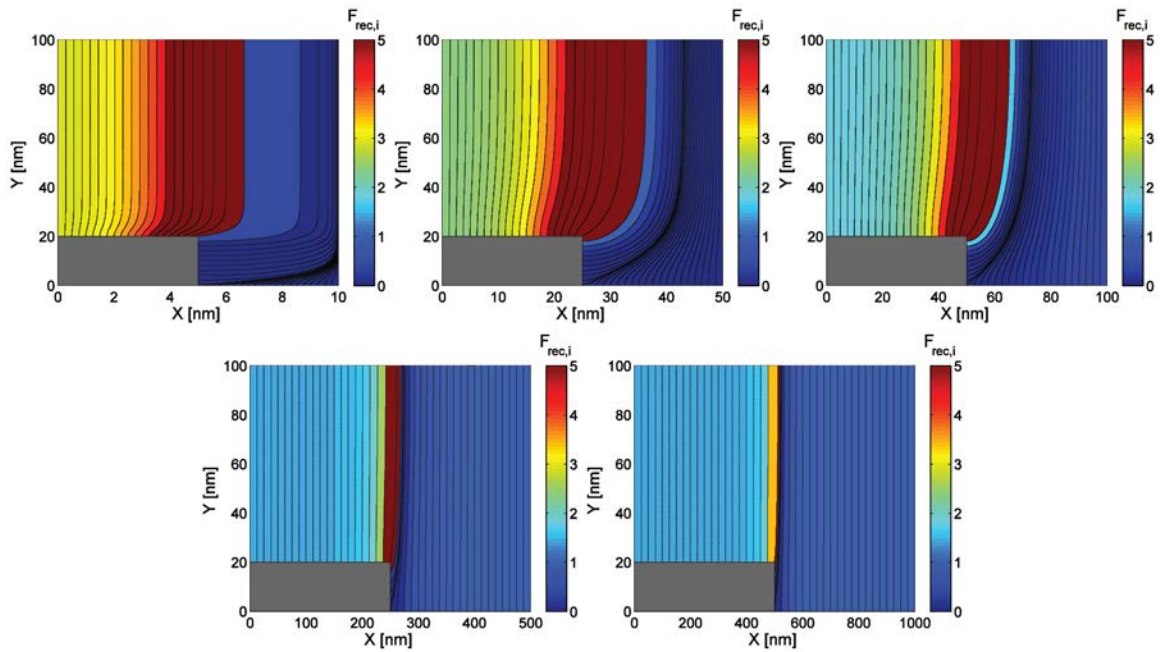


Figure 5.20: Overall recombination enhancement factor, $F_{rec,i}$ the nm- μ m length scales. The half-pitch dimensions are 10, 50, 100, 500, 1000 nm, respectively.

Figure 5.21 demonstrates the overall efficiency enhancements over the same variation of length scales shown above in Figure 5.16-Figure 5.20. The geometries where the nanoimprint thickness is increased to 20nm over the 10nm universally show more electrical enhancement with the exception of the current balance factor at larger half-pitches. The most pronounced enhancement (also Figure 5.17) by the nanoimprint is that of the carrier balance efficiency. This occurs due to the net barrier shift (also Figure 5.16) which serves to enhance recombination in the areas surrounding the inner corner of the nanopattern. The recombination enhancement (also Figure 5.20), which as derived in Equation 5.12, is related to the product of the current balance and carrier confinement efficiencies, increases gradually to a half-pitch of ~ 100 nm and then exponentially rises at lower half-pitches.

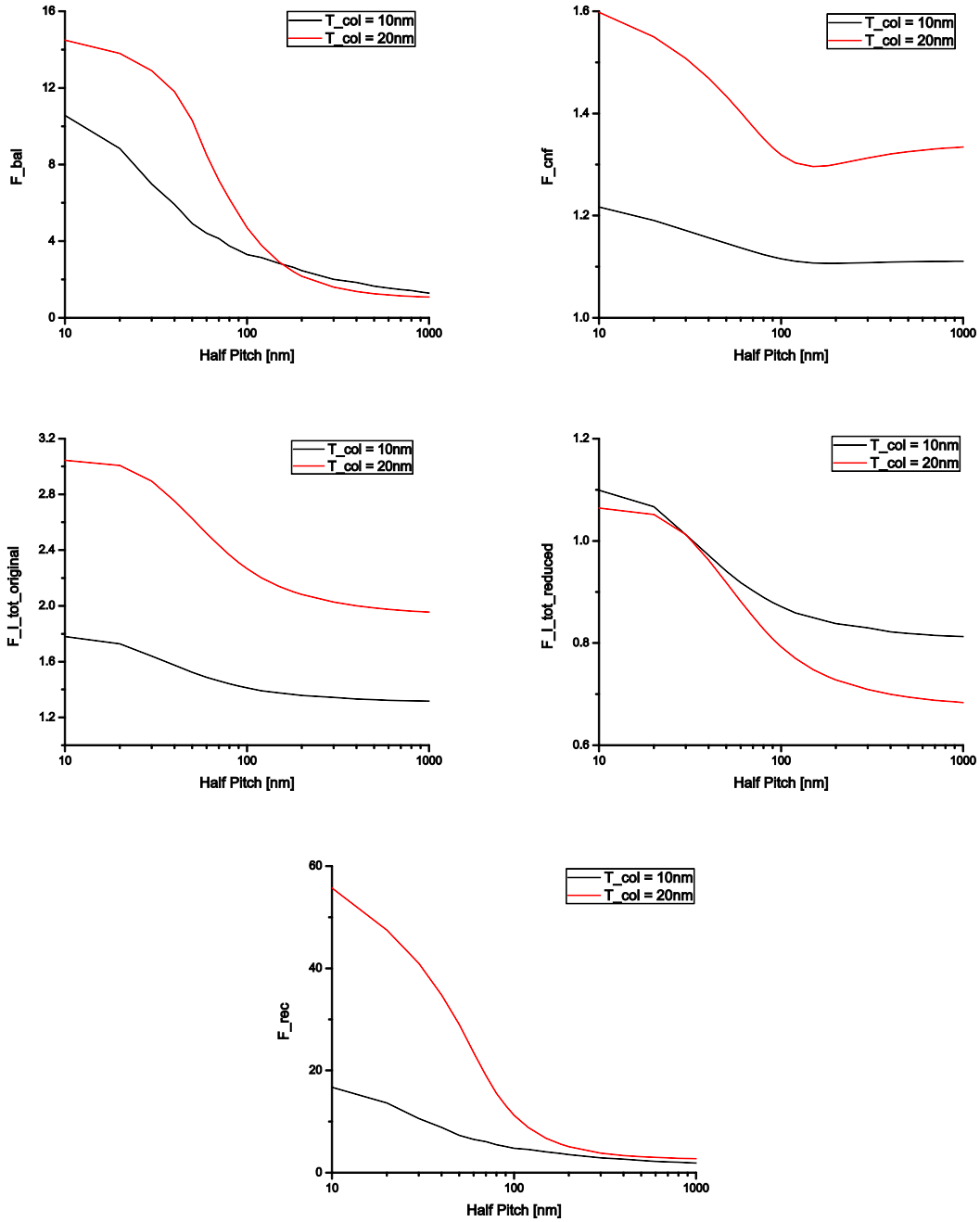


Figure 5.21: Enhancement factors for (A) balance, (B) confinement, (C) total current against original thickness T_{org} , (D) total current against T_{col} -reduced thickness and (E) total recombination. The enhancement factors universally show absolute maxima occurring at smallest half pitch. And, except for confinement, monotonically increase over all patterning geometries towards smaller half pitch.

5.7 Conclusions

In total, these results demonstrate advantages to the SLOLED electrical system from nanoimprint patterning the weaker injecting contact in an SLOLED device. The advantages of total current enhancement and more balanced carrier current are computed for a single geometry.

A carrier-decoupled technique introduced here may be used to extend this treatment to more general cases of SLOLED and multi-layer OLED devices where full numerical solution of the multi-dimensional semiconductor equations would be prohibitive. In particular, the results outline a facile method to determine several important SLOLED device metrics including current balance, carrier confinement, current enhancement and recombination efficiency from use of a streamline analysis.

A numerical study on the influence of nanoimprinting on electrical enhancement effects in a double-sided, injection-limited SLOLED has been conducted. For the optimized nanoimprint geometries selected, with a 20nm imprint thicknesses into a 100nm-thick organic layer in the Al/NPB/ITO device specified, the following enhancement factors compared to the baseline device were found: current balance, 3.53; carrier confinement, 1.32; total current enhancement, 2.06; and recombination efficiency, 4.13. It is finally noted that in regards to recombination efficiency, the nanopatterned device outperforms the planar device reduced by the nanoimprint depth by a factor of 3.00, demonstrating its advantage over merely reducing the film thickness.

Finally, the electrical analysis is extended to a wide range of geometries. It is concluded that the nanoimprint half-pitch on ~100nm is optimal for electrical enhancement. This is the result of the existing tradeoff between high enhancement with reduced practical usefulness (e.g., pattern fidelity) at low half-pitch length scales and reduced electrical efficiency enhancement when using micrometer length scale nanoimprint patterns.

Chapter 6. Analysis of the Emission Enhancement Effects in a Nanopatterned, Single-Layer Organic Light-Emitting Diode

6.1 Introduction

Within this chapter, results from [Chapter 5](#) will be used to extend and analyze the emission enhancement effects associated with the nanopatterned device. In particular, the cumulative enhancement effects of internal quantum efficiency and outcoupling efficiency will be evaluated. Additionally, the knowledge of the optical enhancement is combined with the current-voltage analysis conducted in [Chapter 5](#) to find the optical efficiency enhancement resulting from the nanopatterned device (by weighting by recombination efficiency found in [Chapter 5](#)). These results serve to further quantify the enhancement effects brought about from device nanopatterning.

6.2 Device Emission Metrics

Common metrics exist for quantifying OLED device performance [[155,144](#)]. These metrics will be introduced below in order to describe the enhancement effects experienced by the optical system. Internal quantum efficiency, η_{IQE} , is defined as the number of photons generated to the number of electrons injected. External quantum efficiency, η_{EQE} , is another commonly reported experimental efficiency, that describes the number of photons producing useful light (forward hemispherical) compared to the number of electrons injected into the device. External quantum efficiency, η_{EQE} , can be expressed as:

$$\eta_{EQE} = \gamma \times \eta_{EX} \times \eta_{PL} \times \eta_{OUT} = \eta_{IQE} \times \eta_{OUT} \quad 6.1$$

where γ is the current balance factor (described in [Chapter 5](#)), η_{EX} is the fraction of excitons formed that emit radiatively (roughly 0.25 for fluorescent emitting devices and roughly unity for phosphorescent emitting devices [[155](#)]), η_{PL} is the photoluminescence quantum yield (nearly unity for bulk organic light-emitting materials; however, less than unity when considering exciton-metal-surface quenching) and η_{OUT} is the outcoupling efficiency or light extraction efficiency. In practice, η_{EQE} can be approximated following a common procedure [[156](#)]. Next, the wall-plug efficiency, $\eta_{W/W}$ introduces the electrical power required to operate the OLED circuit into the performance metric and is defined as:

$$\eta_{W/W} = \frac{P_R}{IV} \quad 6.2$$

where P_R is the total forward hemispherical radiant power emitted from the device, I is the device current and V is the driving voltage. Finally, the luminous efficacy or luminous power efficiency, η_P , incorporates photopic correction, or the perceived spectral response of the human eye ([Figure 6.1](#)), and can be expressed as:

$$\eta_P = \frac{L_P}{IV} \quad 6.3$$

where L_p is the total forward hemispherical emitted luminous power. Another commonly reported quantity is the luminance efficiency or current efficiency, η_L , which is the photometric analogy of external quantum efficiency, and can be calculated as:

$$\eta_L = \frac{LA}{I} \quad 6.4$$

where L is device luminance and A is device-emitting area. It follows from Equations 6.1-6.4 that OLED device efficiency bottlenecks include light extraction efficiency, device current balance and carrier injection resistance.

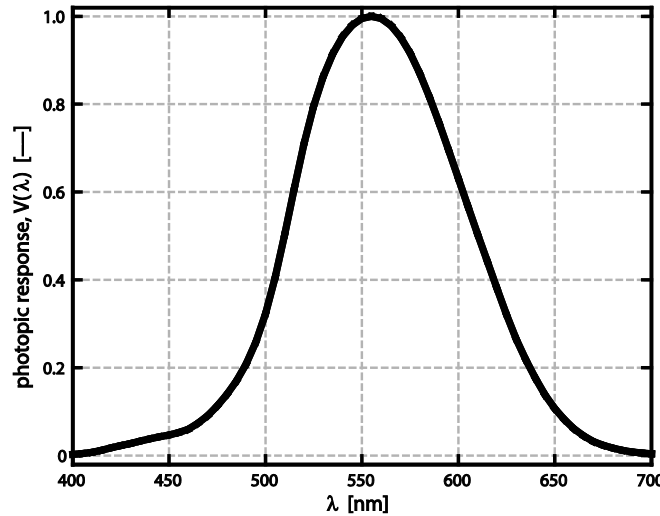


Figure 6.1: Photopic response curve, $V(\lambda)$. This function expresses the normalized perceived light intensity spectrum by the human eye. Data values from [157,158].

6.2.1 Internal Quantum Efficiency

As was previously described internal quantum efficiency relates the number of internally emitted photons to the number of electrons injected. And, further, represents the first of two radiation loss mechanisms of the OLED optical system. But, while the photoluminescence efficiency of organic emitters can approach unity, the exciton decay rate is influenced by the cavity environment in the neighborhood of the dipole emitter [53,54,173,174]. This phenomenon arises from the ability of the optical cavity to influence the radiative decay rate, Γ_{rad} of the dipole emitter. This emitter decay rate is in competition with a non-radiative decay, Γ_{nrad} that unlike the radiative decay rate is relatively independent of the optical environment. Moreover, in a bulk material, the internal quantum efficiency may be expressed as:

$$\eta_{IQE} = \frac{\Gamma_{rad}}{\Gamma_{rad} + \Gamma_{nrad}} \quad 6.5$$

where Γ_{rad} expresses the rate of spontaneous emission and Γ_{nrad} is the rate of non-radiative processes. As previously mentioned, dipole emission may decay by radiative or non-radiative routes. These routes can be described in a Jablonski diagram (see [Figure 2.7](#)), which demonstrates the alternate decay pathways an excitation may take in order to relax to the ground state. However, when the optical cavity is considered, the cavity effect modifies the emission rates leading to the rewritten internal quantum efficiency shown below:

$$\eta_{IQE} = \frac{\Gamma_{rad}^*}{\Gamma_{rad}^* + \Gamma_{nrad}} \quad 6.6$$

where Γ_{rad}^* denotes the modified decay rate due to the optical environment.

[Figure 6.2](#) illustrates the energy transfer to the metallic cathode that arises from the evanescent coupling of the dipole emitter to a surface-plasmon polariton (SPP) mode, which modifies the decay rate of the dipole emitter. This can, alternatively, be seen using a classical oscillator model for the dipole emitter and considering the interference effects that that strong image oscillations that are formed at the metal cathode surface [54].

Following a derivation published elsewhere [166], the quantum mechanical radiative decay rate is proportional to classical dipole power radiated. Thus, the following relationship exists:

$$\Gamma_{decay} \propto P_{rad} \quad 6.7$$

This relationship is shown by relating decay rate to Fermi's golden rule about the photonic mode density as follows [54]:

$$\Gamma_{ij} \propto |M_{ij}|^2 \rho(\nu_{ij}) \quad 6.8$$

where Γ_{ij} is the transition rate from higher energy state i to lower energy state j , M_{ij} is related to the wave function overlap of the excited states and $\rho(\nu_{ij})$ is the photonic mode density of the transition. Further, this quantity can be shown to be related to the imaginary Green's function and ultimately back to power radiated. This result, despite the value of Γ_{nrad} , allows for determination of the η_{IQE} enhancement factor brought about from surface modification (under the assumption that Γ_{nrad} is relatively unaffected by geometric patterning effects). Further, the relationship below can be used as a metric for determining the internal quantum efficiency enhancement due to the patterning, F_{IQE} , shown below:

$$F_{IQE} = \frac{P_{rad}}{P_{rad}^0} = \frac{\Gamma_{decay}}{\Gamma_{decay}^0} \quad 6.9$$

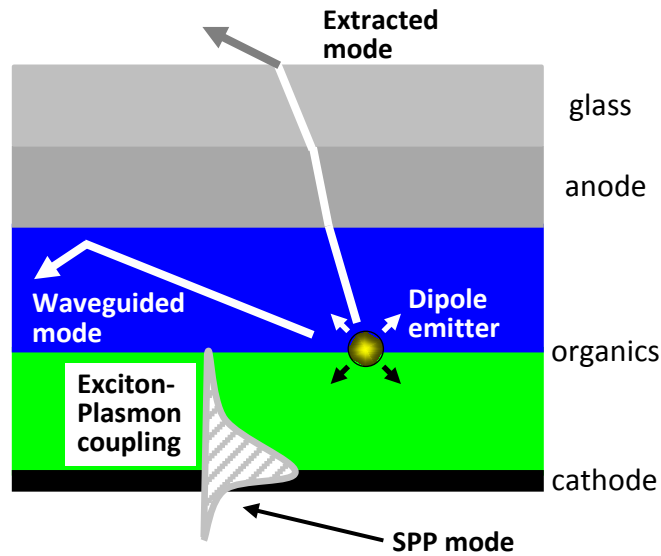


Figure 6.2: Picture of dipole emitter and coupling to waveguide modes and surface-plasmon polariton mode.

6.2.2 Classical Light Extraction Efficiency

During OLED operation, a large number of emitted photons become waveguided in the organic and glass layers (see Figure 6.2). Thin-film optics occur when the thickness of the thin-film cavity is less than or on the order of the wavelength of light traversing the medium. In light-emitting devices, it follows from human perception, that the wavelength range of importance is 400-700nm. Typical OLED device thicknesses are on the order of 100-200nm. The thickness of lab-grade devices commonly includes a transparent conductive oxide (TCO) of Indium-Tin Oxide (ITO) which has thickness of roughly 150nm. Due to the spontaneous emission, directionally-random light is generated. Also, following from Snell's Law, light favors paths ending in high refractive index materials. For this reason, many of the OLED's emitted light rays become waveguided in the organic material (Figure 6.3). From classical ray optics, the outcoupling efficiency that results for a planar emitting layer may be approximated as:

$$\eta_{OUT} \approx \frac{1}{\xi n^2} = 17\% \quad 6.10$$

where ξ is the dipole alignment factor (taken to be 2) and n is the refractive index of the organic media (taken to be 1.7) [23,31]. Therefore, roughly 80% of the generated photons are lost due to absorption in planar OLEDs including nearly 50% of total energy loss through ITO/organic waveguiding and another 30% of total energy loss due to total internal reflection within the glass substrate [31]. Using a variety of different techniques including microlens arrays, optical layers and internal structuring of the organic layers and electrodes, substantial

enhancement in outcoupling efficiency has been demonstrated [31].

From a physical perspective, the extraction efficiency, or outcoupling efficiency, η_{out} , can be written in terms of the previously discussed decay rates as:

$$\eta_{out} = \frac{\Gamma_{rad}}{\Gamma_{rad} + \Gamma_{abs}} \quad 6.11$$

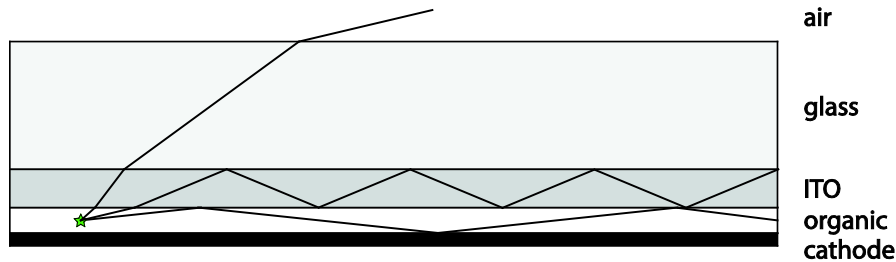


Figure 6.3: Ray tracing of Lambertian emission in an OLED. Classical thin-film optics dictates roughly 20% of emitted light escapes a planar OLED architecture.

6.3 Maxwell Equations

Maxwell Equations govern light propagation in OLEDs (Table 6.1) [97,159,160]. In the following sections, the Maxwell Equations are used to simulate the classical electromagnetic wave (EM) equations, and therein obtain an understanding of the effects of nanopatterning the cathode. The applicability of this set of equations depends on the size scale of the system of interest. For OLEDs, the thicknesses of the active layers are in the 100nm range. However, since the layers and energy transfer occurs on length scales larger than quantum scale, these equations are applicable.

The Maxwell equations represent coupled wave equations. The field variables of vector electric field (\mathbf{E}) and vector magnetic field (\mathbf{M}) are sought to be determined. The Maxwell Equations may be written in either differential or integral forms. Below, in Table 6.1, the Maxwell Equations are portrayed in both forms. The names of the variables within the equations are also included.

Table 6.1: Maxwell Equations in both integral and differential forms [159].

Faraday's Law:

$$\frac{\partial \mathbf{B}}{\partial t} = -\nabla \times \mathbf{E} - \mathbf{M}$$

$$\frac{\partial}{\partial t} \iint_A \mathbf{B} \cdot d\mathbf{A} = - \oint_{\ell} \mathbf{E} \cdot d\boldsymbol{\ell} - \iint_A \mathbf{M} \cdot d\mathbf{A}$$

Ampere's Law:

$$\frac{\partial \mathbf{D}}{\partial t} = \nabla \times \mathbf{H} - \mathbf{J}$$

$$\frac{\partial}{\partial t} \iint_A \mathbf{D} \cdot d\mathbf{A} = - \oint_{\ell} \mathbf{H} \cdot d\boldsymbol{\ell} - \iint_A \mathbf{J} \cdot d\mathbf{A}$$

Gauss' Law (electric field):

$$\nabla \cdot \mathbf{D} = 0$$

$$\iint_A \mathbf{D} \cdot d\mathbf{A} = 0$$

Gauss' Law (magnetic field):

$$\nabla \cdot \mathbf{B} = 0$$

$$\iint_A \mathbf{B} \cdot d\mathbf{A} = 0$$

Constitutive Relationships:

$$\mathbf{D} = \epsilon \mathbf{E} = \epsilon_r \epsilon_0 \mathbf{E}$$

$$\mathbf{B} = \mu \mathbf{H} = \mu_r \mu_0 \mathbf{H}$$

Symbols:

\mathbf{E} : Electric field

\mathbf{D} : Electric flux density

\mathbf{H} : Magnetic field

\mathbf{B} : Magnetic flux density

\mathbf{J} : Electric current density

\mathbf{M} : Magnetic current density

Constants:

ε :	Electric permittivity
ε_r :	Relative permittivity
ε_0 :	Permittivity of free space
μ :	Magnetic permeability
μ_r :	Relative permeability
μ_0 :	Permeability of free space

6.4 FDTD Simulation Setup

The Finite Difference Time Domain (FDTD) is an applied finite difference theory commonly used to discretize the Maxwell Equations. A common implementation used for FDTD is the Yee algorithm [167]. A variety of commercial FDTD packages are available. In this work, Lumerical FDTD Solutions[®] was used [163]. Lumerical FDTD Solutions is a fully vectorial Maxwell Equation solver.

The nanoimprinted geometry discussed in Chapter 5 will again be the geometry of interest. The first part to developing a simulation is to define the simulation domain. A 3d simulation domain is defined with an equal width and breadth of 24 μm . The region should be large enough such that nearly all injected energy which contributes to forward hemispherical (useful) radiation is capable of escaping the system. Some fraction of the energy will be waveguided in the ITO and organic layers and may not be fully absorbed within the simulation domain. In order to ensure that the energy escaping is accurately tabulated and not allowed to reenter the solution domain, a series of PML (perfectly-matched layers) are used to effectively absorb this energy. The aluminum cathode may be assumed to completely absorb emitted light due to its penetration depth being $\sim 6\text{nm}$ at optical wavelengths (Figure 6.5). Nonetheless, at some time during the simulation, a significant amount of the input energy from the source pulse is absorbed and the simulation is deemed complete. Once the simulation is completed, post-processing of the collected data may begin. The layer thicknesses are representative of the device specified in Chapter 5. In addition to the previously specified organic layer thickness (NPB is 100nm), the thicknesses of the electrodes and glass must now be included in the geometry. The Al layer that has been consistently deposited in our experiments is 50nm. The ITO-coated-glass is purchased commercially and consists of 150nm thick ITO on 250 μm glass. The optical constants of the requisite layers (Al, NPB, ITO, glass, air) are described using a multiple-coefficient fits in the Lumerical software [163]. The raw thin-film optical constants are shown in Figure 6.4.

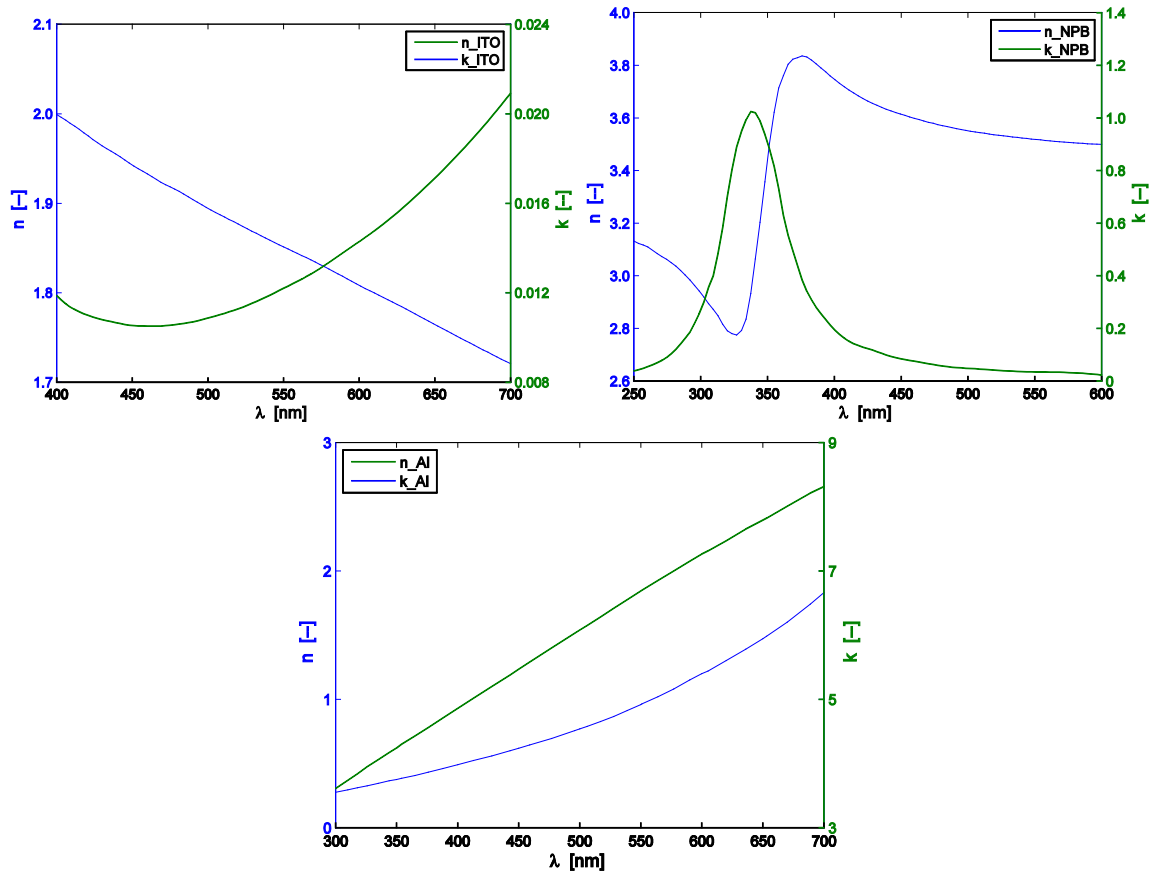


Figure 6.4: Optical constants for ITO [169], NPB [170] and Al [171].

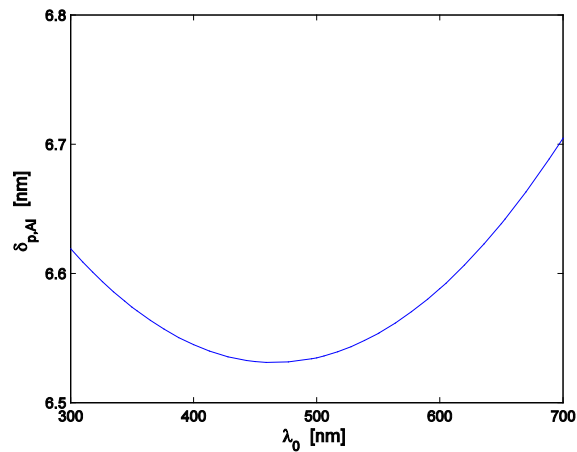


Figure 6.5: Penetration depth of Al, $\delta_{p,Al}$ computed from data in [171]. This data validates the optically thick approximation for the Al cathode layer for the 50nm Al layer.

Next, a series of dipole elements and energy monitors are inserted into the simulation domain. The power monitors act to keep track of the aggregate energy (in time) that has left the system. When all of the energy injected has either been absorbed or exits the system, the simulation ends. A series of positions and orientations of dipoles with an emission spectrum matching that of NPB are entered into the simulation region.

The emission mechanism for organic materials is assumed to be modeled by an incoherent, unpolarized dipole emission [168]. Therefore, as is commonly used in literature, an ensemble of orthogonal dipole sources (of a convolution of wavelengths) will be used to model the emission of the spontaneous dipole emission. The emission source is taken as a dipole which is constructed with frequency data nearly approximating the emission spectrum of an emitting NPB molecule (approximated as Gaussian with FWHM at 475 and 600nm). Further, multiple dipole locations are simulated in order to reproduce the locations of light emission from the periodic modifications within the OLED cavity. In order to produce the effective emission from a single point at a single wavelength in the organic media, the time-averaged effective electric field intensity, $\langle |E|^2 \rangle$, is found from superposition of Cartesian-basis-oriented dipoles as follows [168]:

$$\langle |E|^2 \rangle = \frac{1}{3} \left\{ |E_{pol_x}|^2 + |E_{pol_y}|^2 + |E_{pol_z}|^2 \right\} \quad 6.12$$

where the subscript pol_i represents the dipole polarization of the emitting dipole. Figure 6.6 is an example of the simulation domain showing the dipole emitter.

Once the simulations have been completed, post-processing may then be performed. Following the simulation run, a number of monitors have recorded the electric field flux data at cell nodes bounding the FDTD transmission data region (as shown in Figure 6.6). The electric field flux may be integrated over time to achieve a total energy spatial profile along the FDTD transmission region. Using frequency-domain techniques, the electric field flux can also be converted into frequency space to recover spectral information. Next, a far-field profile (“Transmission Data (far field)” in Figure 6.6) may be determined for the emitting source [159]. This allows the electric field to be projected onto a surface at a distance of ~1mm and determines the emission profile that passes through the glass/air interface. Note that this technique does not account for multiple reflections inside the glass layer. Finally, for the case of computing the outcoupling efficiency, the integral of total energy radiated that crosses the glass/air interface is measured and compared to the total energy of the dipole pulse. The dipole emission energy is measured by a small transmission monitor to account for the absorbing characteristics of the emitting layer.

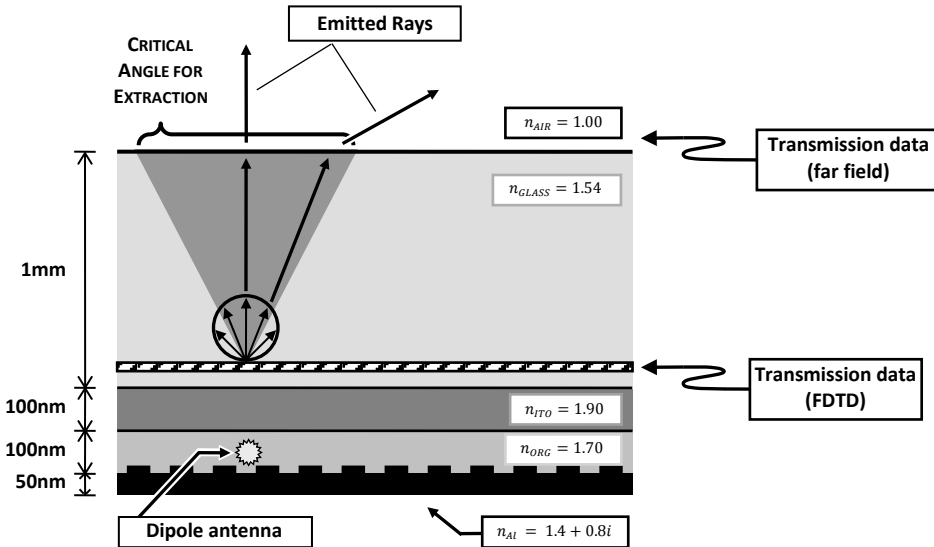


Figure 6.6: Description of the physical OLED system under investigation using the FDTD solver. A dipole antenna is placed in the organic active layers to resemble the spontaneous emission of light. During the simulation, information regarding the energy of light is extracted as the “Transmission Data”. Using far-field transformation techniques, the far-field data can be extrapolated from the ITO-glass interface to the air-glass interface to acquire knowledge about the light energy that is emitted from the device.

6.5 FDTD Results

FDTD simulations are used to solve the expected optical enhancement resulting from a nanopatterned column OLED modification. Below, the results using the simulation setup above are a standard simulation is depicted. The resulting energy emitted is computed in the near field through use of the transmission computation from the FDTD software. Following this calculation, this data may be projected through use of ray tracing in order to determine the amount of emitted dipole energy emitted in the forward hemispherical direction or any particular angle of interest. With this capability, general dipole environments may be simulated revealing the expected light extraction enhancement from internal and optical modifications to the OLED cavity.

6.5.1 Planar OLED

First we consider the case of a planar OLED. The results showing the external quantum efficiency for the dipole emitters are shown below in [Figure 6.7](#) and [Figure 6.8](#). Note that the X-dipole plot is identical to the Y-dipole case; therefore, this plot is not included. The Z-dipole shows a small contribution to the overall power radiated. According to the [Figure 6.8](#), which is an average of the dipole orientations, the recombination position which maximizes the power radiated is at 56nm from the cathode (or 44nm from the anode).

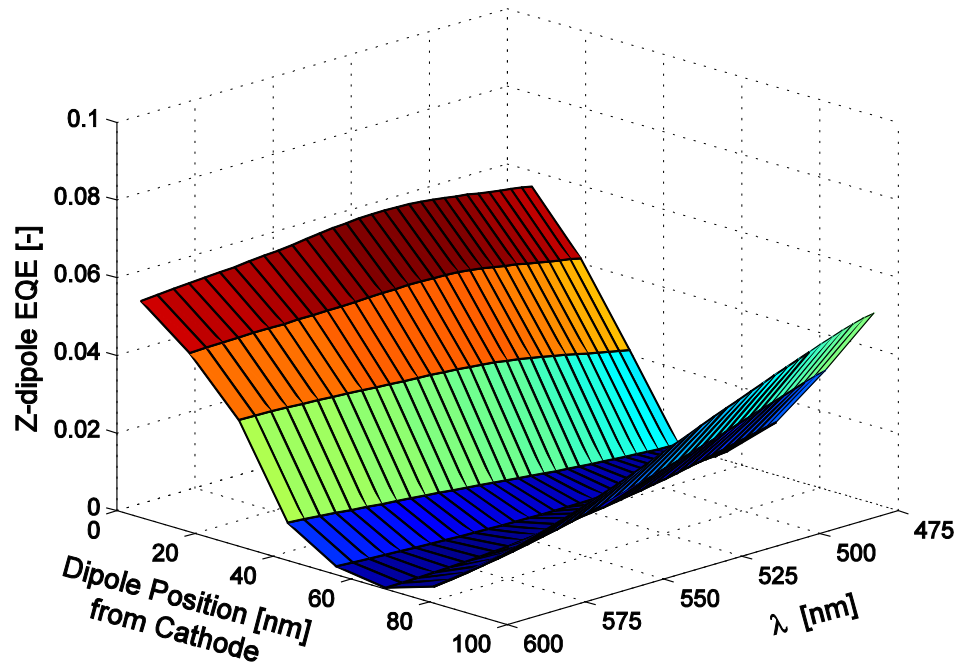
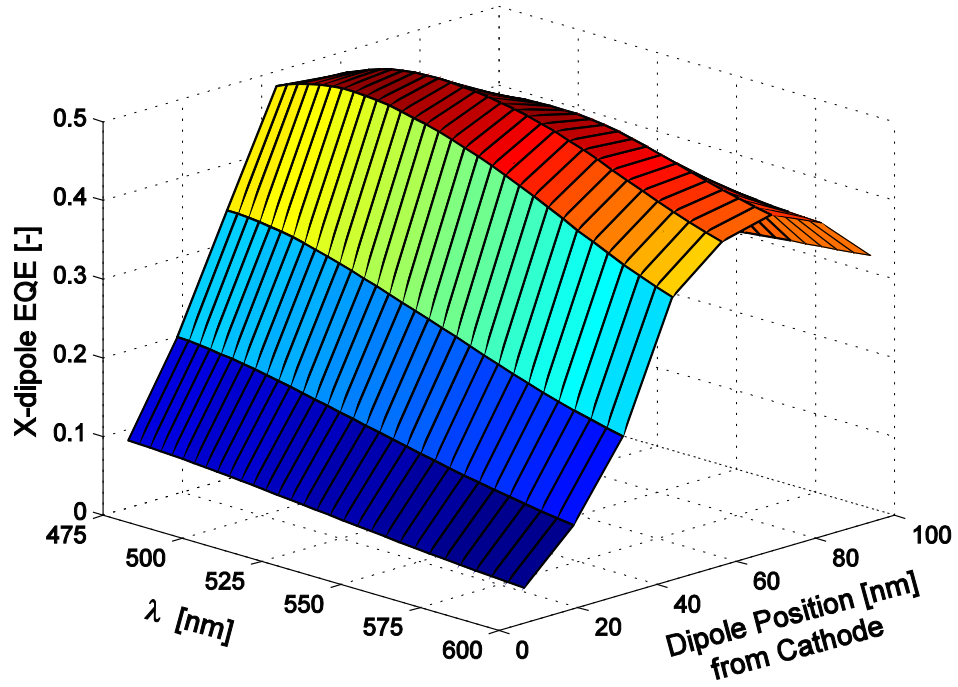


Figure 6.7: On top, X-dipole spectral, positional EQE for planar OLED. On bottom, Z-dipole spectral, positional EQE for a planar OLED.

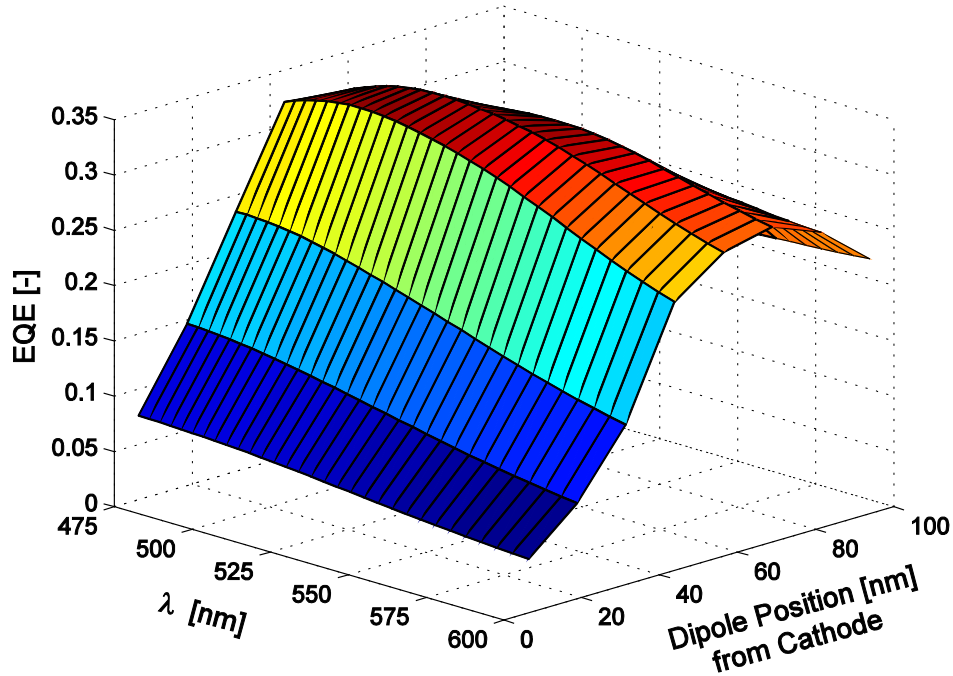


Figure 6.8: Dipole-averaged spectral, positional EQE for a planar OLED.

6.5.2 Dipole Emission Enhancement from Nanopatterning

The figures in this section show the enhancement from periodic nanopatterning for the 100nm width, 100nm spacing structure with a 20nm imprint. The insets map the location of the dipoles in relation to the OLED organic layers.

Figure 6.9 shows the Z-dipole enhancement resulting from the nanopatterned cathode. It is shown that for the Z-dipoles, the dipoles that are radiated near the cathode pattern are significantly enhanced over the planar OLED. The enhancement is most notably improved at blue emission wavelengths (near 475nm), where the enhancement grows to ~8X (~30%) that of the original dipole (~4%) for the dipole between in the nanoimprint region (filled-in triangle).

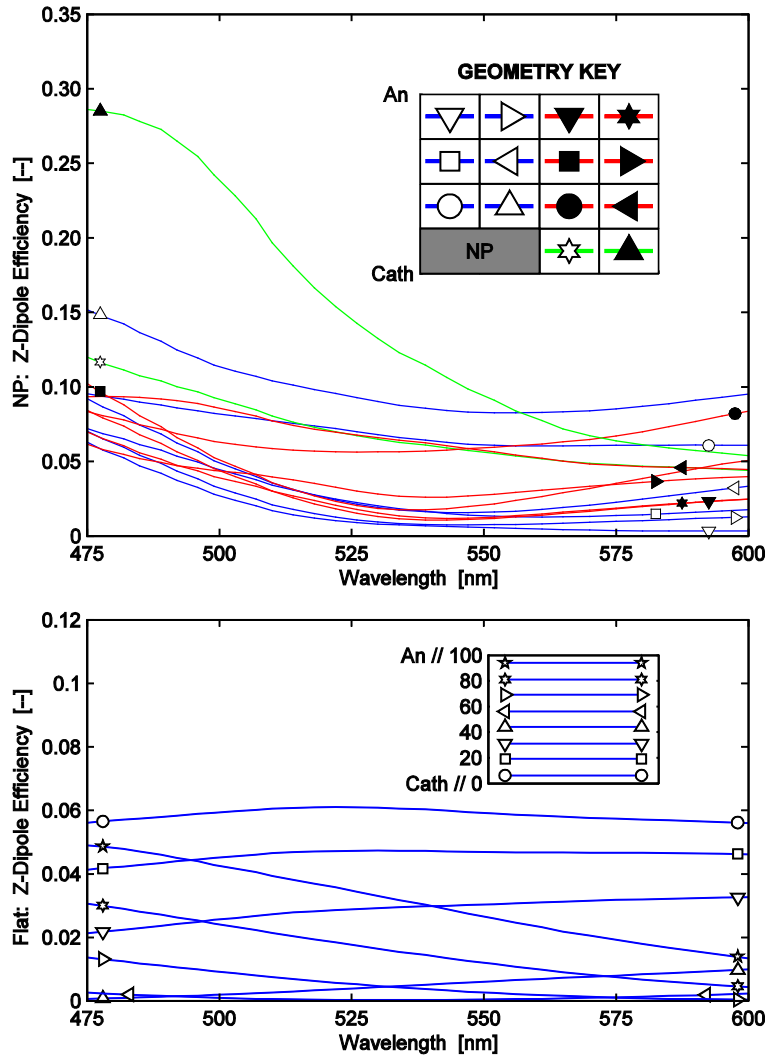


Figure 6.9: Z-dipole external quantum efficiency. At top, Z-dipole EQE when including internal nanopatterning; at bottom, Z-dipole EQE for the planar device. The insets show the dipole location within the OLED environment.

Figure 6.10 compares the X-dipole efficiencies of the planar and nanopatterned OLED. The X-dipoles are perpendicular to cathode-imprinted nanocolumn array. In this case, the dipole that exhibits the largest enhancement in Z-dipole efficiency (filled-in triangle) now experiences negligible enhancement. And, its neighbor (open star) now experiences large enhancement at blue wavelengths. The dipole locations above the open star (left and right filled-in triangle) experience reduced radiation enhancement at blue wavelengths. The dipoles closest to the cathode have the lowest efficiencies for the planar case; however, the nanopatterned modification shows improved efficiency at blue wavelengths near the corners.

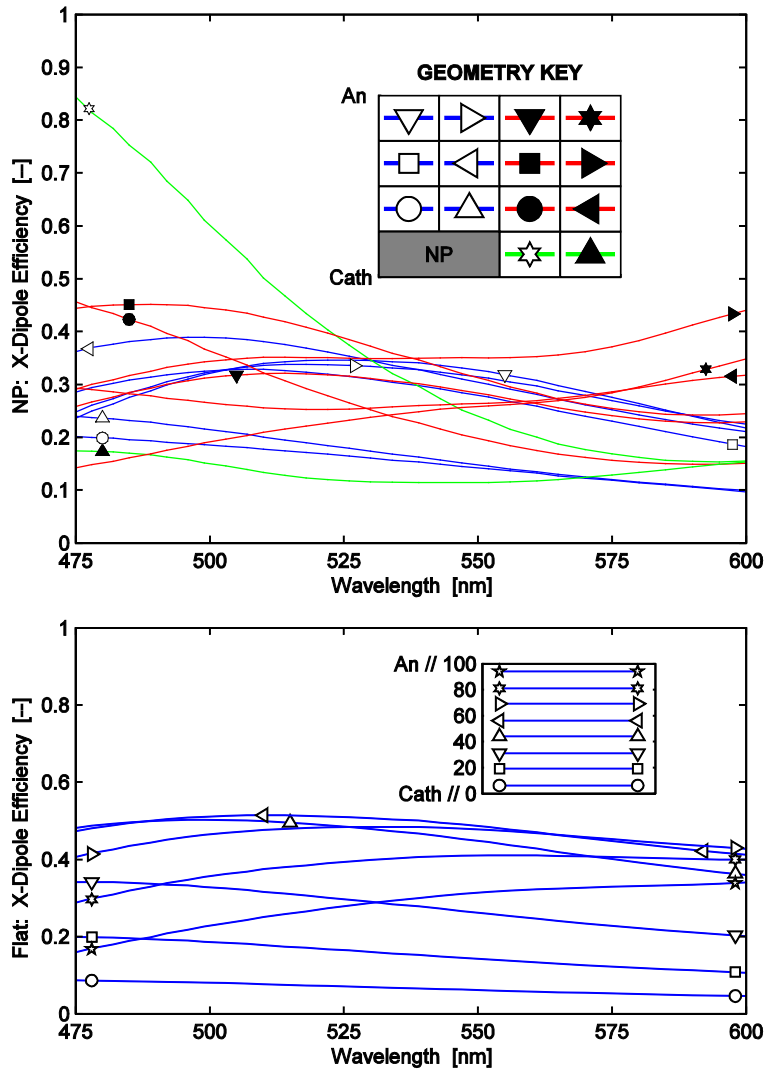


Figure 6.10: X-dipole external quantum efficiency. At top, X-dipole EQE when including internal nanopatterning; at bottom, X-dipole EQE for the planar device. The insets show the dipole location within the OLED environment.

Figure 6.11 compares the Y-dipole efficiencies of the planar and nanopatterned OLED. The Y-dipoles are parallel to the cathode-imprinted nanocolumn array. The results show modest enhancements for a number of dipole positions at blue wavelengths. This can best be seen by the monotonic increases in dipole efficiency at near the blue side of the emission spectrum for nearly all dipole positions. The positions with the largest enhancement occur near the organic-anode interface. Conversely, dipole positions near the cathode have reduced efficiency, especially the dipoles that are located next to the nanoimprinted Al contact (open star and filled-in triangle).

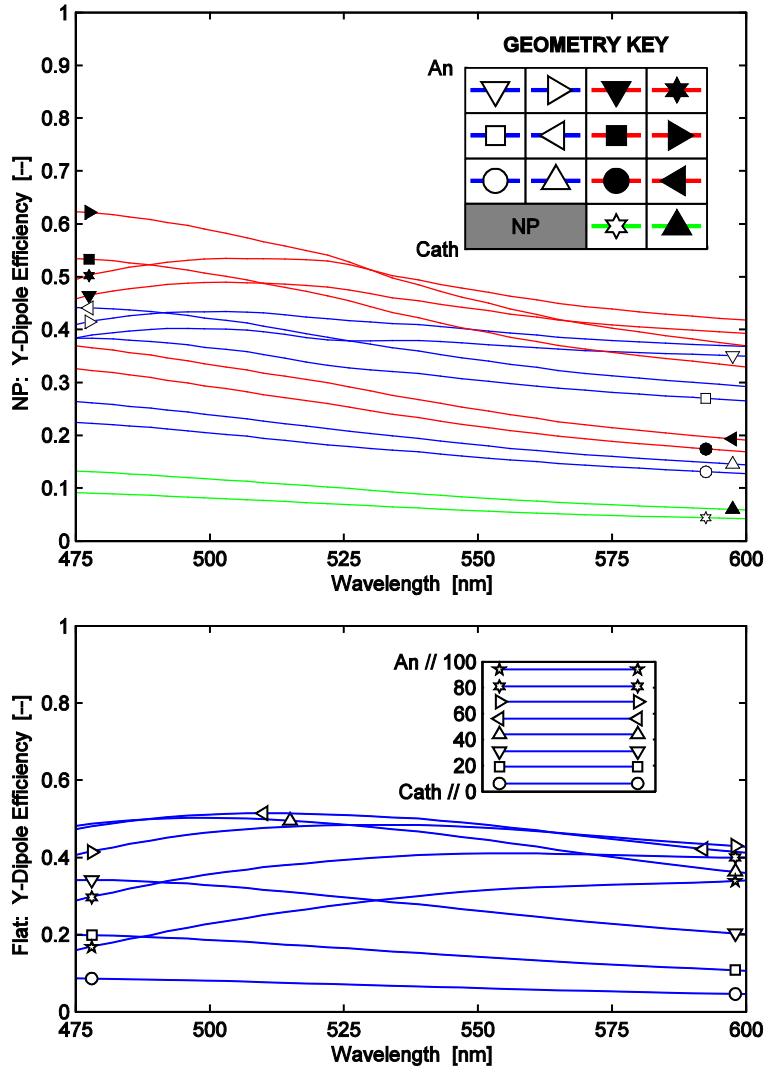


Figure 6.11: Y-dipole external quantum efficiency. At top, Y-dipole EQE when including internal nanopatterning; at bottom, Y-dipole EQE for the planar device. The insets show the dipole location within the OLED environment.

Figure 6.12 compares the incoherent dipole (dipole averaged, see Equation 6.12) efficiencies of the planar and nanopatterned OLED. The trend shows enhanced dipole efficiencies at blue wavelengths over the planar device. The dipole position with red lines (above non-imprinted part of nanopatterned OLED) show the largest overall efficiencies, closely followed by the dipole positions with blue lines (above imprinted part of nanopatterned OLED). It is interesting to note that the efficiencies become enhanced near the blue part of the spectrum. It can be seen that the red wavelengths (near 600nm) are similar to the efficiencies of the planar device. This suggests that there is the potential for an optical enhancement similar to the microcavity effect for nanopatterned OLEDs. Further, a resonant nanopatterned cavity device could promote further enhancement beyond the device geometry in question, which

was optimized for electrical enhancement.

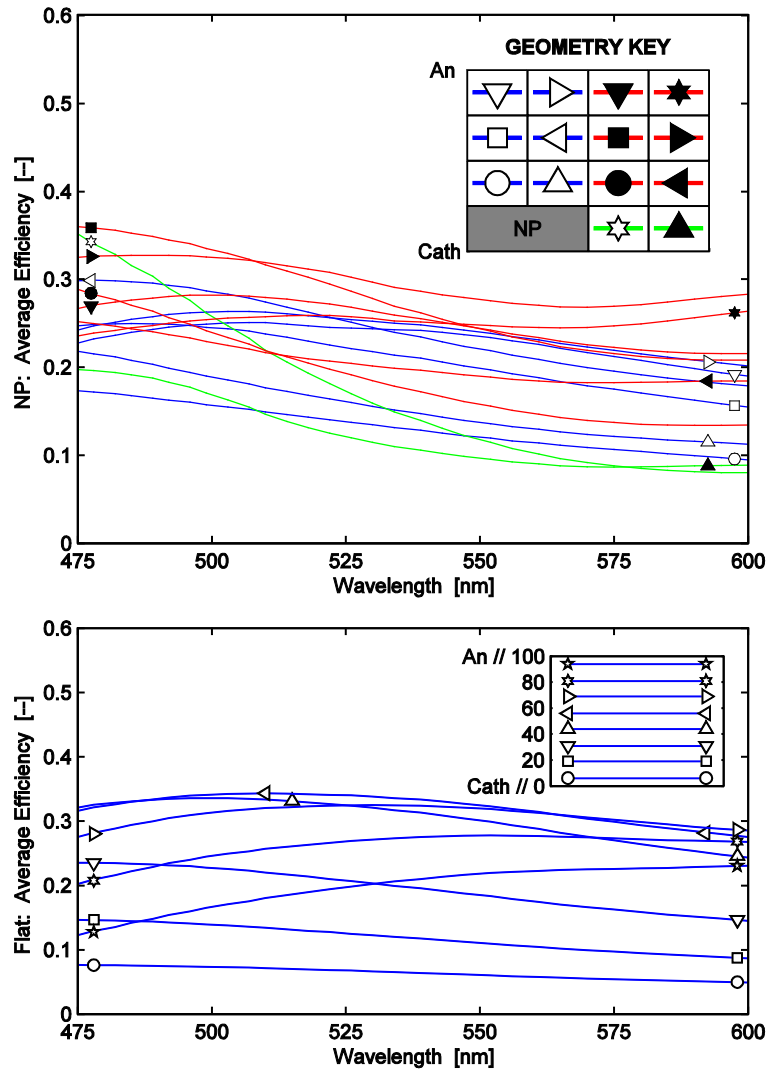


Figure 6.12: Incoherent dipole (dipole-averaged) external quantum efficiency. At top, the incoherent dipole EQE when including internal nanopatterning; at bottom, incoherent dipole EQE for the planar device. The insets show the dipole location within the OLED environment.

6.5.3 Recombination-Weighted External Quantum Efficiency Enhancement

The external quantum efficiency include the effects from the electrical model to determine and weight the positional enhancement effects.

6.5.3.1 Recombination rate weighting from electrical model

In the previous analysis conducted in [Chapter 5](#), the recombination rate over a streamline

was found. However, as the more pertinent piece of information required to conduct the dipole analysis is the positional recombination rate, the analysis is now extended. From the developed set of equations in [Chapter 5](#), the recombination rate, R_i^j :

$$R_i^j = \frac{q\mu}{\varepsilon} n_i^j \times p_i^j \quad 6.13$$

where, the discretization above corresponds to the streamline path, i and the path element, j . The streamline carrier conservation from Equation [5.38](#) is restated below:

$$(n + p)_i^{cath} = (n + p)_i^{an} = (n + p)_i^j = N_i \quad 6.14$$

Along the streamline, i , the total carrier concentration, N_i , is conserved. Additionally, since the anode-side injection barrier height is smaller than the cathode-side injection barrier height and charge carriers can only be created and destroyed in matching pairs, the following relationship exists:

$$p_i^j \gg n_i^j \quad 6.15$$

Then, the following relation follows from Equation [6.14](#) and Equation [6.15](#) that the hole carrier concentration is roughly constant along the pathline and may be found from the following relation:

$$p_i^j \approx p_i^{an} = n_{SM}(E_i^{an}, \Phi_{B,p}) \quad 6.16$$

Where n_{SM} is the Scott-Malliaras carrier injection concentration, previously described in Equation [5.33](#). Further, substitution into the recombination rate described in Equation [6.13](#) may be made with the electron carrier concentration found in Equation [5.45](#), as follows:

$$R_i^j \approx \frac{q\mu}{\varepsilon} p_i^{an} \times n_i^{cath} \times \exp\left(-\frac{2q}{\varepsilon} \frac{p_i}{C_i^2} A_i^j\right) \quad 6.17$$

The above relation expresses the positional recombination rate on the streamline position. Linear interpolation is then used to transform the streamline position onto a rectangular map. [Figure 6.13](#) (left) shows the normalized calculation of recombination rate across a nanopatterned device. [Figure 6.13](#) (right) displays the same information as the left plot except it is portrayed as a logarithm measurement to show finer features of the recombination rate where the recombination rate is low. This mapping and weighting is then used in the FDTD solver to weight the emission regions, where dipoles are most likely to emit radiation.

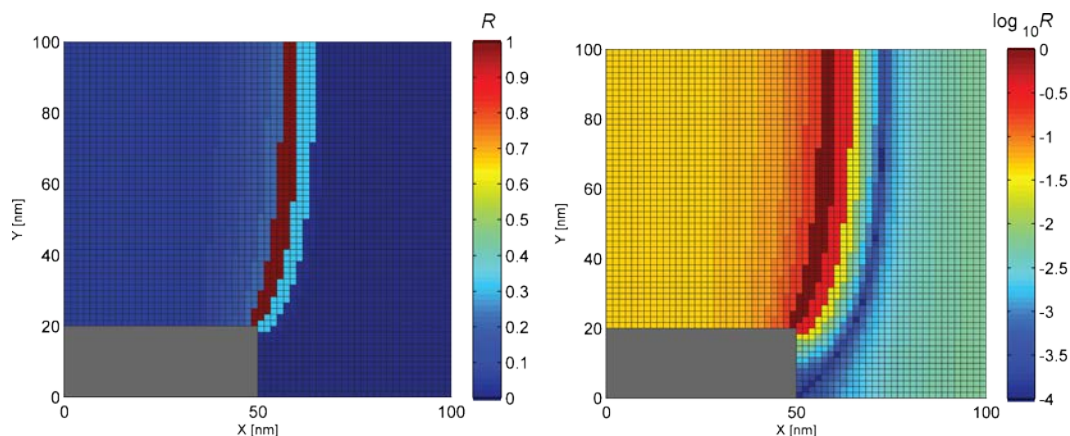


Figure 6.13: Normalized recombination map transformed from streamline grid to a rectangular grid. At left, a finely resolved rectangular grid mapping. At right, a logometric depiction of the same normalized recombination map at left.

6.5.3.2 Optical Enhancement

In this section the results from the Section 6.5.2 are converted to an easier-to-read form. The efficiencies are compared to that of planar OLEDs of the same thickness region as the part of the nanopatterned device. Therefore, two separate emission bases are included. One is for the imprinted portion of the nanopatterned OLED (left 50nm in, e.g., Figure 6.14). The other is the non-imprinted portion of the nanopatterned OLED (right 50nm in, e.g., Figure 6.14). Using these background values allows assignment of enhancement to the nanopatterned device over that of the planar device. In all of the figures below, a colormap was associated between enhancement limits of 0.5(blue) and 1.5(red). Additionally, the color of the numeric values of the enhancement factors in the figures is used only to make the values more legible.

Figure 6.14 (Z-Dipole map) shows strong enhancement throughout the internal region of the device at blue wavelengths that recede from the electrode-organic regions at the wavelength is increased. For the Z-Dipole, the internal dipole positions (c.f. Figure 6.9) have lower overall efficiencies than the two regions near the cathode. Also, in general, the Z-Dipole has a lower effective efficiency than the X- and Y- dipoles (c.f. Bottom Figure 6.9, Bottom Figure 6.10, Bottom Figure 6.11). The maximum EQE for the planar Z-Dipole is ~6% whereas the maximum EQE for the X- and Y- dipoles are ~50%. Furthermore, these dipoles represent a potential mechanism for improving the overall optical efficiency of OLED devices.

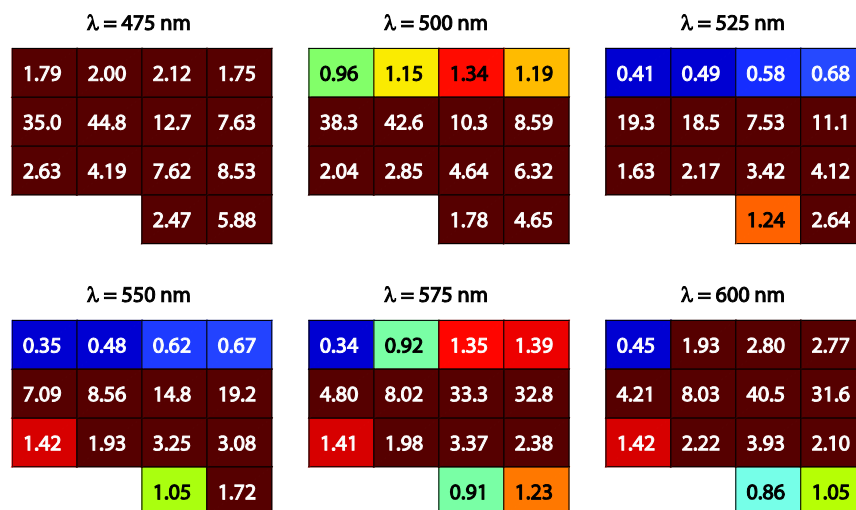


Figure 6.14: Z-Dipole external quantum efficiency (EQE) position map.

Figure 6.15 (X-Dipole map; dipole perpendicular to the nanocolumn arrays) shows strong enhancement in the vicinity of the internal cathode corner. The enhancement effect is strongest near blue part of the spectrum. This enhancement effect diminishes at dipole emission energies near the red part of the spectrum. Also the fractional amount of light energy, compared to the planar OLED, decreases with wavelength except in the areas in the middle of the non-imprint nanopatterned areas (rightmost column of the dipole map).

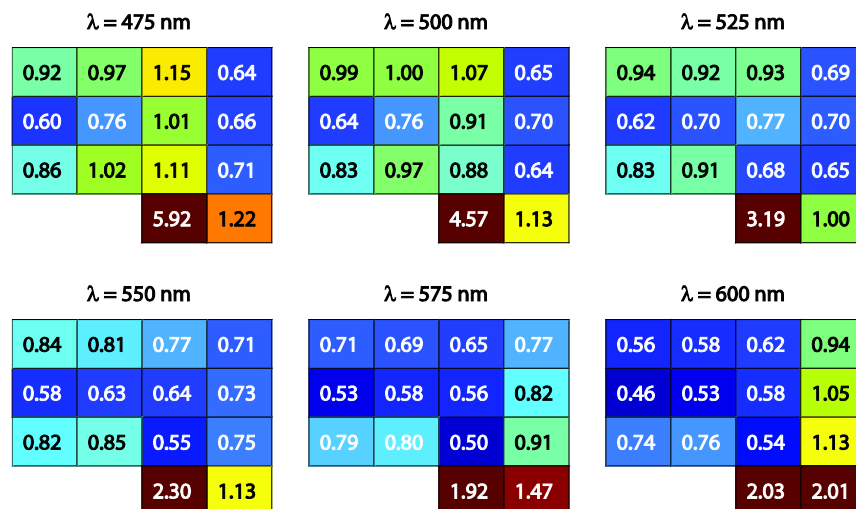


Figure 6.15: X-Dipole external quantum efficiency (EQE) position map.

Figure 6.16 (Y-Dipole map; dipole parallel to the nanocolumn arrays) shows enhanced optical efficiency near the anode of the cavity that decreases toward the cathode side. Again, the enhancement is strongest near the blue wavelength region and diminishes with increasing wavelengths. As the wavelength is increased the nanopattern benefits along the anode recede beginning from the nanoimprinted side eventually rendering the entire anode with minimal enhancement at red wavelength part of the spectrum.

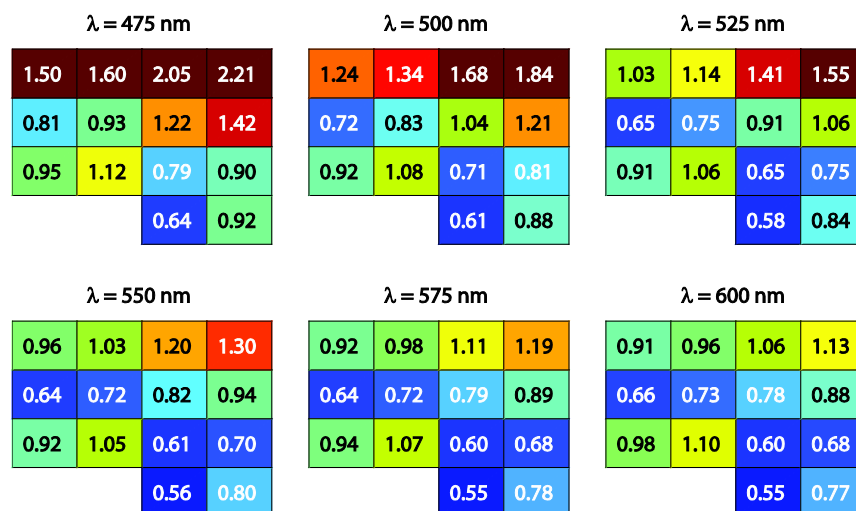


Figure 6.16: Y-Dipole external quantum efficiency (EQE) position map.

Figure 6.17 shows the dipole-averaged optical efficiency (computed from Equation 6.12). The results show at wavelengths near the blue part of the spectrum 11 of 14 regions exhibit enhanced optical efficiency. In particular, there is ~30% optical enhancement near the interior corner where the results from the electrical model from Chapter 5 indicate there will be the largest recombination enhancement (this will be considered in more detail later this section). However, this enhancement is diminished as the emitting wavelengths shift toward the red side of the spectrum. There is also a factor of two (2) enhancement near the base cathode region at the blue wavelengths and a 50% enhancement near the middle of the anode. Again the enhancement effects are strongly related to the wavelength of the emitted light.

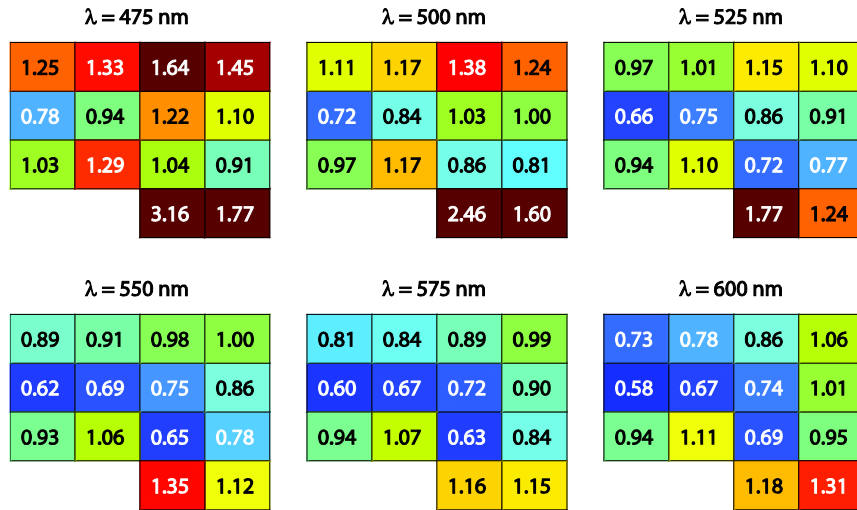


Figure 6.17: Isotropic external quantum efficiency (EQE) position map.

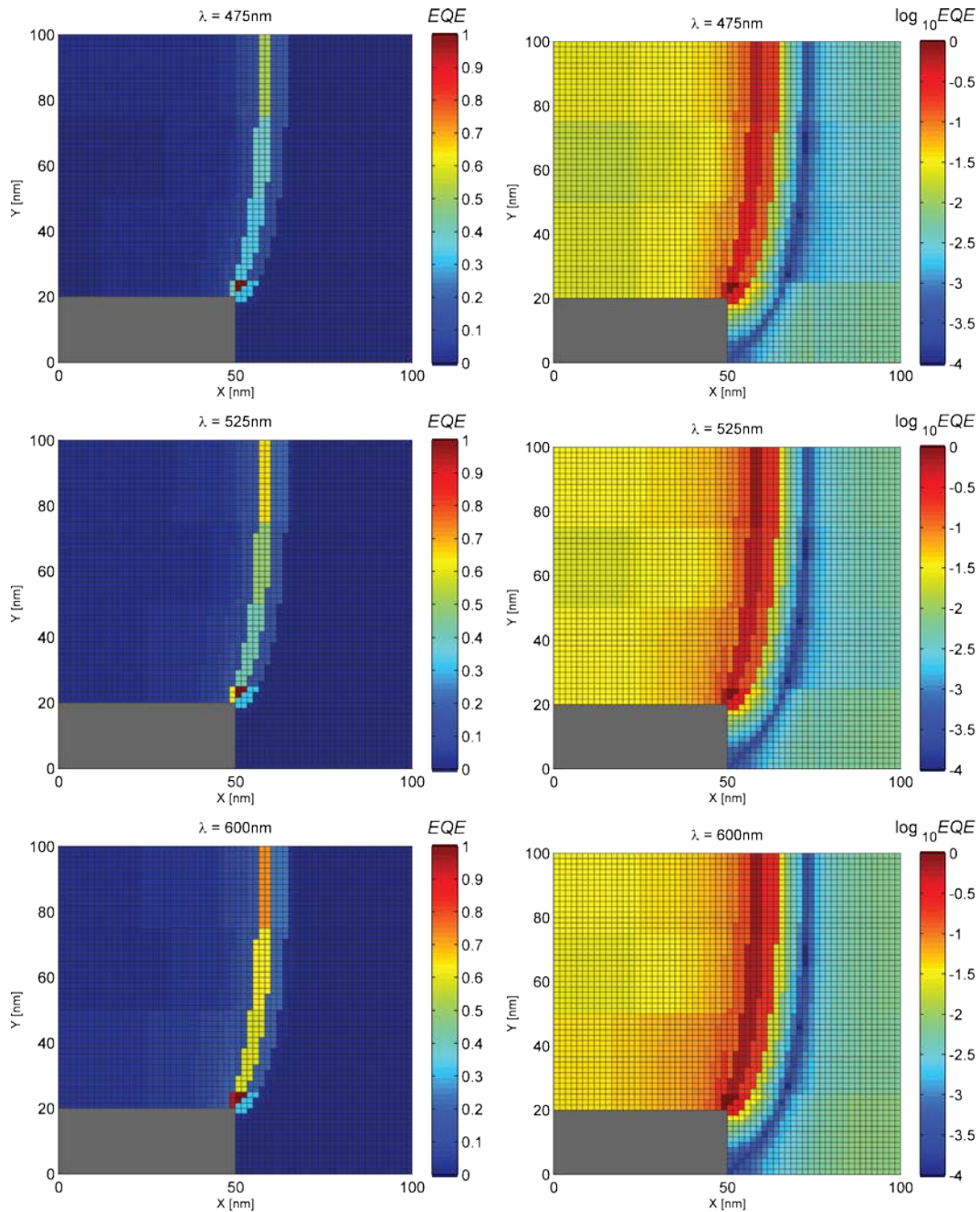


Figure 6.18: Normalized external quantum efficiency maps transformed to a rectangular grid. From top to bottom, EQE at wavelneghts 475, 525 and 600nm. At left, a finely resolved rectangular grid mapping. At right, a logometric depiction of the same normalized recombination map at left.

Figure 6.18 shows that the largest EQE values exist ($\sim 5\text{nm}$) outside of the interior corner. The trends also show that the EQE maintains the largest EQE along the streamlines of the interior corner, largely related to the high η_{rec} (Chapter 5) in this region.

The overall spectral optical enhancement, $F_{opt,\lambda}$, is found in [Figure 6.19](#) from the following relation:

$$F_{opt,\lambda} = \frac{\sum_i \left[\left(\frac{R}{R_0} \right)_i \times \left(\frac{L}{L_0} \right)_{\lambda,i} \right]}{\sum_i \left(\frac{R}{R_0} \right)_i} \quad 6.18$$

where, above, $(R/R_0)_i$ is the normalized positional recombination ([Figure 6.13](#)), $(L/L_0)_{\lambda,i}$ is the spectral, dipole-averaged, normalized luminance profile ([Figure 6.17](#)) and i an element in the wire mesh shown in, for example, [Figure 6.13](#). Additionally, the recombination-optical product in the braces of the numerator is displayed in [Figure 6.18](#). The overall spectral optical enhancement factor is shown in [Figure 6.19](#). It is shown that the overall optical enhancement is roughly 30% at the blue wavelength of 475nm but then experiences a loss at wavelengths greater than 510nm and, ultimately, is decreased by 20% at wavelengths between 550 and 600nm. Again, these results show the spectral effect that the nanopattern cavity has on preferentially increasing the optical efficiency.

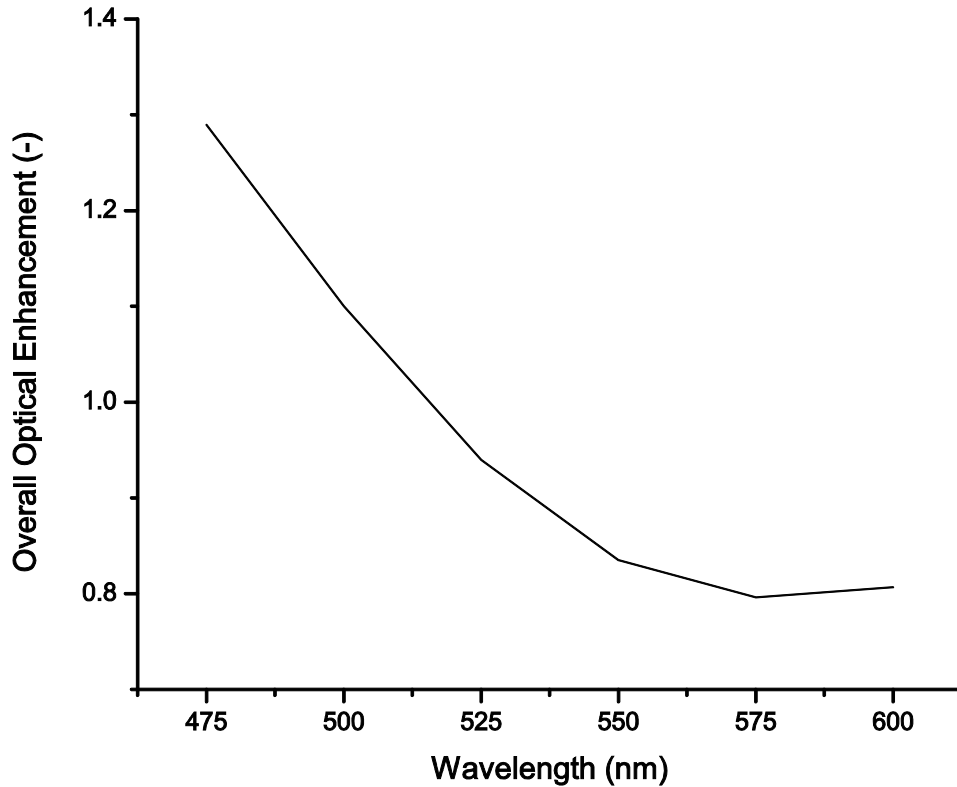


Figure 6.19: Overall spectral optical enhancement, $F_{opt,\lambda}$ (Equation 6.18).

6.6 Conclusions

The optical effects for the electrically-optimized nanopatterned SLOLED device determined in [Chapter 5](#) have been analyzed. The goal was to determine the influence on the optical effects may have on OLED device efficiency. In conventional devices, there is much room for improvement as only 20% of all photons generated are emitted as useful light. It is then postulated that internal nanopatterning may also improve optical efficiency of the device.

First, the device metrics used to characterize the overall performance of an OLED were introduced with emphasis on the internal quantum efficiency and outcoupling efficiency as the two processes that may be affected by the internal nanopatterning.

Next, the concepts and setup of the FDTD Solutions® commercial software were discussed. The simulations were then conducted and useful results presented. The planar device dipole emission was first evaluated to serve as a basis for nanopatterned emission comparison. The dipole emission enhancements were shown in [Section 6.5.2](#). The overall optical enhancement from the nanopattern was discussed in [Section 6.5.3](#). The final results showed that for the 100nm width, 100nm spacing and a 20nm imprint thickness, the emission was enhanced by roughly 30% for blue (475nm) wavelengths and was reduced by 20% for the green/red (550-600nm) wavelengths.

Finally, the results of this chapter showed that the ~100nm internal nanopattern has a minor influence on the overall external quantum efficiency ($\pm 30\%$ depending on emission wavelength). The dipole emission trends show that there is enhancement near the electrode-organic interface regions and that there is a reduction of radiated power in the inner parts of the OLED cavity. However, it is again noted that the nanopattern geometry was chosen to optimize the electrical enhancement effects, if the geometry was designed to enhance the optical effects of the device it is possible that larger optical enhancement effects could be realized.

Chapter 7. Conclusions and Future Work

7.1 Conclusions

This work investigates the enhancement effects that internally nanopatterned OLED devices have over their planar counterparts. Experimental results demonstrate enhanced JV and LV characteristics for nanopatterned anode and nanopatterned cathode devices. Through the analyses developed and conducted in this work, the beneficial effects to the electrical and optical systems are explained.

In [Chapter 5](#), the electrical system was considered. When the weaker injecting electrode is nanopatterned, the electrical system has improved carrier injection parity and recombination efficiency since the injection enhancement favors the nanopatterned electrode. Furthermore, the suggested nanopattern feature size to optimize electrical enhancement is ~100nm.

In [Chapter 6](#), the optical system was considered. Commercial FDTD software was used to evaluate the modification to the optical system resulting from the nanopatterned array. The results show that for the ~100nm feature size nanopatterned array, there was around 15-30% optical enhancement for blue part of spectrum which diminished near the red wavelength part of the spectrum.

Overall, the comprehensive series of results documented in this work demonstrate that nanopatterned OLED devices experience enhanced device characteristics over their planar counterparts.

7.2 Future Work

Future investigation could be aimed at comparing and investigating the feature size dependence of the nanopattern stamp with the optical simulation results from commercial FDTD software. The optical cavity effect could be uniquely probed through deposition of emitting and non-emitting layers of similar refractive index (to probe emitting layer depth) and then could be monitored by time-resolved photoluminescence (TRPL).

Another future direction could be aimed at fabricating OLED devices with integrated nanopatterned optical layers (e.g., MoO₃, ZnO and TiO₂) to further improve light extraction. Again, the experimental findings could be compared with numerical results from the electrical and optical modeling to outline a comprehensive method for predicting device enhancement and to determine the effective benefits for a wide range of device modifications. There is also a potential that wavelength-scale patterning and cavities can be used for interesting optical phenomenon such as optically-pumped lasers [[175](#)].

References

1. Round, H.J. *Elec. World*. **49**, 308 (1907).
2. Schubert, E.F. *Light-emitting Diodes*. Cambridge University Press, 2003.
3. Loebner, E.E. *IEEE T. Electron Dev.* **23**, 675 (1976).
4. Lossev, O.V. *Phil. Mag.* **6**, 1024 (1928).
5. Zheludev, N. *Nature Photonics*. **1**, 189 (2007).
6. Destriau, G. *J. Chim. Phys.* **33**, 587 (1936).
7. Hilsum, C. *New Scientist*, **369**, 666 (1963).
8. Kitai, A. *Luminescent Materials and Applications*. Wiley, 2008.
9. Bernanose, A., Comte, M., Vouaux, P. *J. Chim. Phys.* **50**, 65 (1953).
10. Shinar, S., ed. *Organic Light-Emitting Devices*. New York: Springer-Verlag, (2004).
11. Vlasenko and Popkov. *Optics & Spectroscopy*. **8**, 39 (1960).
12. Welker, H. *Z. Naturforsch.* **7a**, 744 (1952).
13. Welker, H. U.S. Patent 2,798,989 (1957).
14. Lehovec, K., Accardo, C.A., Jamgochian, E. *Phys. Rev.* **83**, 603 (1951).
15. Holonyak, N., Bevacqua, S.F. *Appl. Phys. Lett.* **1**, 82 (1962).
16. Pope, M., Kallman, H.P., Magnante, P. *J. Chem. Phys.* **38**, 2042 (1963).
17. Helfrich, W., Schneider, W.G. *Phys. Rev. Lett.* **14**, 229 (1965).
18. Hartman, W.A., Armstrong, H.L. *J. Appl. Phys.* **38**, 2393 (1967).
19. Hush, N.S. *Ann. New York Acad. Sci.* **1006**, 1 (2003).
20. Ferraris, J., Cowan, D.O., Walatka, V., Pearlstein, J.H. *J. Amer. Chem. Soc.* **95**, 948 (1973).
21. Borsenberger, P.M., Weiss, D.S. *Organic photoreceptors for xerography*. New York: Marcel Dekker, Inc. 1998.
22. Kim, J.S., Ho, P.K.H., Greenhan, N.C., Friend, R.H. *J. Appl. Phys.* **88**, 1073 (2000).
23. Shinar, J., Shinar, R. *J. Phys. D: Appl. Phys.* **41**, 133001 (2007).
24. Ruhstaller, B., et. al. *J. Appl. Phys.* **89**, 4575 (2001).
25. Tang, C.W., VanSlyke, S.A. *Appl. Phys. Lett.* **11**, 913 (1987).
26. Burroughes, J.H., et. al. *Nature*. **347**, 539 (1990).
27. Baldo, M.A., et. al. *Nature*. **395**, 151 (1998).
28. Friend, R.H., et. al. *Nature*. **397**, 121 (1999).
29. Möller, S., Forrest, S.R. *J. Appl. Phys.* **91**, 3324 (2002).
30. Reineke, S., et. al. *Nature*. **459**, 234 (2009).
31. Saxena, K., Jain, V.K., Mehta, D.S. *Optical Materials*. **32**, 222 (2009).
32. Sun, Y., Forrest, S.R. *Nature Photonics*. **2**, 483 (2008).
33. Hung, L.S., Tang, C.W., Mason, M.G. *Appl. Phys. Lett.* **70**, 118344 (1997).
34. Shen, Y., Hosseini, A.R., Wong, M.H., Malliaras, G.G. *Chem. Phys. Chem.* **5**, 16 (2004).

35. Walzer, K., Maennig, B., Pfeiffer, M., Leo, K. *Chem. Rev.* **107**, 1233 (2007).
36. "Multi-Year Program Plan FY '09 - FY '15: Solid-State Lighting Research and Development." United States Department of Energy, Energy Efficiency and Renewable Energy. [Online] Available: <http://www1.eere.energy.gov/buildings/ssl/techroadmaps.html>.
37. "Total Energy – Annual Energy Review." Energy Information Administration. [Online] <http://www.eia.gov/totalenergy/data/annual/index.cfm>
38. "Current OLED projects." United States Department of Energy. [Online] Available: http://www1.eere.energy.gov/buildings/ssl/organic/current_organic.html
39. "Current LED projects." United States Department of Energy. [Online] Available: http://www1.eere.energy.gov/buildings/ssl/light/current_light.html
40. "World Record White OLED Performance Exceeds 100 lm/W." United States Department of Energy. [Online] Available: http://www1.eere.energy.gov/buildings/ssl/highlights_udc08.html
41. OLED-Display.net. [Online] Available: <http://www.oled-display.net/>
42. "Global Organic Light Emitting Diode (OLED) Display Market holds Enormous Revenue Potential and is expected to reach \$10.6 billion by 2020." Electronics.ca Research Network. [Online] Available: <http://www.electronics.ca/presscenter/articles/1335/1/Global-Organic-Light-Emitting-Diode-OLED-Display-Market-holds-Enormous-Revenue-Potential-and-is-expected-to-reach-106-billion-by-2020/Page1.html>
43. "Semiconductor Manufacturing Organic Light Emitting Diodes (OLEDs): Tehnologies and Global Markets." BCC Research Market Forecasting. [Online] Available: <http://www.bccresearch.com/report/SMC069A.html>
44. Earmme, T., Ahmed, E., Jenekhe, S.A. *Adv. Mater.* **22**, 4744-4748 (2010).
45. Fukagawa, H., Yokoyama, N., Irida, S., Tokito, S. Pyridoindole Derivative as Electron Transport Host Material for Efficient Deep-blue Phosphorescent Organic Light-emitting Diodes. *Adv. Mater.* **22**, 4775-4778 (2010).
46. *Handbook of Optoelectronics, Volume I*. Chapter by Grell, Martin; *Organic light emitting diodes*. Taylor and Francis, 2006.
47. Partridge, R.H. *Polymer*, **24**, 733, 739, 748, 755 (1983).
48. Chiang, C.K., Fincher, C.R., Park, Y.W., Heeger, A.J., Shirakawa, H., Louis, E.J., Gao, S.C., MacDiarmid, A.G. *Phys. Rev. Lett.* **39**, 1098 (1977).
49. Kabra, D., Liu, L.P., Song, M.H., Snaith, H.J., Friend, R.H. Efficient Single-Layer Polymer Light-Emitting Diodes. *Adv. Mater.* **22**, 3194 (2010).
50. Tse, S.C., Tsung, K.K., So, S.K. *Appl. Phys. Lett.* **90**, 213502 (2007).
51. Wang, Z., Lou, Y., Naka, S., Okada, H. *Appl. Phys. Lett.* **97**, 203302 (2010).
52. Lane, P.A., Kushto, G.P., Kafafi, Z.H. *Appl. Phys. Lett.* **90**, 023511 (2007).
53. Chance, R.R., Prock, A., Silbey, R. Molecular Fluorescence and Energy Transfer near Interfaces. *Adv. Chem. Phys.* **37**, 1 (1978).
54. Barnes, W.L. Fluorescence near interfaces: the role of photonic mode density. *J. Mod.*

- Optic.* **45**, 661 (1998).
55. Pierret, R.F. *Semiconductor Device Fundamentals*. Addison Wesley, 1996.
 56. Sze, S.M., Ng, K.K. *Physics of Semiconductor Devices*. Wiley-Interscience, 2007.
 57. Moore, G.E. *Electronics*. **38**, 114 (1965).
 58. Menard, E., et. al. *Chem. Rev.* **107**, 1117 (2007).
 59. Shirota, Y., Kageyama, H. *Chem. Rev.* **107**, 953 (2007).
 60. Chen, H.-Y., Hou, J., Zhang, S., Liang, Y., Yang, G., Yang, Y., Yu, L., Wu, Y., Li, G. *Nat. Photonics*. **3**, 649 (2009).
 61. So, F., ed. *Organic Electronics: Materials, Processing, Devices and Applications*. New York: CRC Press, 2010.
 62. Klauk, H., ed. *Organic Electronics: Materials, Manufacturing and Applications*. Weinheim, Germany: Wiley-VCH Verlag GmbH & Co., 2006.
 63. Silinch, E. A., Capek, V. *Organic Molecular Crystals: Interaction, Localization, and Transport Phenomena*. New York: AIP Press, 1994.
 64. Brütting, W., ed. *Physics of Organic Semiconductors*. Weinheim, Germany: Wiley-VCH Verlag GmbH & Co., 2005.
 65. Pope, M., Swenberg, C. E. *Electronic Processes in Organic Crystals and Polymers*. New York: Oxford University Press, 1999.
 66. Kao, K.C., Hwang, W. *Electrical Transport in Solids: with particular reference to organic semiconductors*. New York: Pergamon Press, 1981.
 67. Schwoerer, M., Wolf, H.C. *Organic Molecular Solids*. Weinheim, Germany: Wiley-VCH Verlag GmbH & Co., 2007.
 68. Vardeny, Z.V., ed. *Ultrafast dynamics and laser action of organic semiconductors*. New York: CRC Press, 2009.
 69. Stallinga, P. *Electrical Characterization of Organic Electronic Materials and Devices*. John Wiley & Sons, Ltd., 2009.
 70. Kittel, C. *Introduction to Solid State Physics (8th Ed.)*. John Wiley & Sons, Inc., 2004.
 71. "Thin Film Evaporation Guide." Vacuum and Engineering Materials. [Online] Available: http://www.vacengmat.com/downloads/VEM_Thin_Film_Evaporation_Guide.pdf
 72. Bao, Z., Locklin, J., ed. *Organic Field-Effect Transistors*. New York: CRC Press, 2007.
 73. Kagan, C., Andry, P. *Thin-film Transistors*. New York: Marcel Dekker, 2003.
 74. Forrest, S.R. *Nature*. **428**, 911 (2004).
 75. Kalinowski, J. *Organic Light-Emitting Diodes: Principles, Characteristics, and Processes*. New York: Marcel Dekker, 2005.
 76. Bässler, H. Charge Transport in Disordered Organic Photoconductors. *Phys. Stat. Sol. (b)*. **175**, 15 (1993).
 77. Lampert, M., Mark, P. *Current Injection in Solids*. New York: Academic Press, 1970.
 78. Bulovic, V. *Phys. Rev. B*. **58**, 3730 (1998).
 79. Chance, Prock, Sibley. *Adv. Chem. Phys.* **37**, 1 (1978).

80. Bässler, H. *Phys. Stat. Sol. (B)*. **175**, 15 (1983).
81. Tutiš, E., Bussac, M.N. *J. Appl. Phys.* **89**, 430 (2001).
82. Gummel, H.K. *IEEE T. Electron Dev.* **11**, 455 (1964).
83. Scharfetter, D.L., Gummel, H.K. *IEEE T. Electron Dev.* **16**, 64 (1969).
84. Malliaras, G.G, Shen, Y., Dunlap, D.H. *Appl. Phys. Lett.* **79**, 2582 (2001).
85. Wallace, J.U., Young, R.H., Tang, C.W., Chen, S.H. *Appl. Phys. Lett.* **91**, 152104 (2007).
86. Cheung, C.H., Tsung, K.K, Kwok, K.C., So, S.K. *Appl. Phys. Lett.* **93**, 083307 (2008).
87. Madigan, C.F.: Ph.D. dissertation, Massachusetts Institute of Technology (2006).
88. Montroll, E.W., Scher, H. *J. Stat. Phys.* **9**, 101 (1973).
89. Walker, A. *J. Phys: Cond. Mater.* **14**, 9825 (2002).
90. Tessler, N., Preezant, Y., Rappaport, N., Roichman, Y. *Adv. Mater.* **21**, 2741 (2009).
91. Anderson, P.W. *Phys. Rev.* **109**, 1492 (1958).
92. Montroll, E.W., Scher, H.J. *Stat. Phys.* **9**, 101 (1973).
93. Vasileska, D., Goodnick, S.M., Klimeck, G. *Computational Electronics*. New York: Taylor and Francis Group, LLC., 2010.
94. Kalinowski, J. *J. Phys. D.* **32**, R179 (1999).
95. Blom, P.W.M., de Jong, M.J.M., Liedenbaum, C.T.H.F. *Polym. Adv. Technol.* **9**, 390 (1998).
96. Gill, W.D. *J. Appl. Phys.* **43**, 5033 (1972).
97. Siegel, R., Howell, J. *Thermal Radiation Heat Transfer (4th Ed.)*. New York: Taylor and Francis, 2002.
98. Chen, G. *Nanoscale energy transport and conversion*. New York: Oxford University Press, 2005.
99. Malliaras, G.G., et. al. *Appl. Phys. Lett.* **79**, 2582 (2001).
100. Burrows, P.E., Shen, Z., Bulovic, V., McCarty, D.M., Forrest, S.R., Cronin, J.A., Thompson, M.E. *J. Appl. Phys.* **79**, 7991 (1996).
101. Snowden, C.M., Snowden, E. *Introduction to Semiconductor Device Modeling*. River Edge, New Jersey: World Scientific Publishing, 1986.
102. "Notes on Disordered Matter." [Online] Available: <http://blog.disorderedmatter.eu/2008/04/04/recombination-in-low-mobility-semiconductors-langevin-theory/>
103. Tutis, E., Batistic, I., Berner, D. *Phys. Rev. B.* **70**, 161202(R) (2004).
104. Yampolskii, S.V., Genenko, Y.A., Melzer, C., Stegmaier, K., von Seggern, H. *J. Appl. Phys.* **104**, 073719 (2008).
105. Richardson, O.W. *Phil. Trans. R. Soc. Lond. A.* **201**, 497 (1903).
106. Fowler, R.H., Nordheim, L. *Proc. R. Soc. Lond. A.* **119**, 173 (1928).
107. So, F., Ed. *Organic Electronics*. New York: CRC Press, 2010.
108. Ishii, H., et. al. *Adv. Mater.* **11**, 605 (1999).
109. Scott, J.C. *J. Vac. Sci. B.* **21**, 521 (2003).

110. Kahn, A., Hoch, N., Gao, W. *J. Polym. Sci. B.* **41**, 2529 (2003).
111. Knupfer, M., Priser, H. *Phys. Sol. (A)*. **201**, 1055 (2004).
112. Hwang, J., Wan, A., Kahn, A. *Mat. Sci. Eng. R.* **64**, 1 (2009).
113. Schottky, W. *Physik. Z.* **75**, 872 (1914).
114. Davids, P.S., Campbell, I.H., Smith, D.L. *J. Appl. Phys.* **82**, 6319 (1997).
115. Scott, J.C., Malliaras, G.G. *Chem. Phys. Lett.* **299**, 115 (1999).
116. Emtage, P.R., O'Dwyer, J.J. *Phys. Rev. Lett.* **16**, 356 (1966).
117. Selberherr, S. *Analysis and Simulation of Semiconductor Devices*. Springer, 1984.
118. Markovich, P.A., Ringhofer, C.A., Schmeiser, C. *Semiconductor Equations*. Springer-Verlag, 1990.
119. Ruhstaller, B., Beierlein, T., Riel, H., Karg, S., Scott, J.S., Riess, W. *IEEE J. Sel. Top. Quant.* **9**, 723 (2003).
120. Crone, B.K., Davids, P.S., Campbell, I.H., Smith, D.L. *J. Appl. Phys.* **87**, 1974 (2000).
121. Mott, N.F., Gurney, R.W. *Electronic Processes in Ionic Crystals*. New York: Oxford University Press, 1940.
122. Rose, A. *Phys. Rev.* **103**, 1648 (1956).
123. Lampert, M.A. *Phys. Rev.* **103**, 165248 (1956).
124. Helfrich, W., Schneider, W.G. *Phys. Rev. Lett.* **14**, 229 (1965).
125. Mori, T., et. al. *Appl. Surf. Sci.* **212-213**, 458 (2003).
126. Langmuir, I. *Phys. Rev.* **21**, 419 (1921).
127. Stallinga, P. *Adv. Mater.* **23**, 3356 (2011).
128. Li, L., Kosina, H. *Adv. Polym. Sci.* **223**, 301 (2010).
129. Braun, D., Heeger, A.J., Kroemer, H. *J. Elec. Mater.* **20**, 945 (1991).
130. Braun, D., Heeger, A.J., Kroemer, H. *Appl. Phys. Lett.* **58**, 1982 (1991).
131. Parker, I.D. *J. Appl. Phys.* **75**, 1659 (1994).
132. Heeger, A.J., Parker, I.D., Yang, Y. *Synth. Met.* **67**, 23 (1994).
133. Wolf, U., Arkhipov, V.I., Bäessler, H. *Phys. Rev. B.* **59**, 7507 (1999).
134. Arkhipov, V.I., Wolf, U., Bäessler, H. *Phys. Rev. B.* **59**, 7514 (1999).
135. Barth, S., Wolf, U., Bäessler, H. *Phys. Rev. B.* **60**, 8791 (1999).
136. Arkhipov, V.I., von Seggern, H., Emelianova, E.V. *Appl. Phys. Lett.* **83**, 5074 (2003).
137. Baldo, M.A., Forrest, S.R. *Phys. Rev. B.* **64**, 085201 (2001).
138. Limketkai, B.N., Baldo, M.A. *Phys. Rev. B.* **71**, 085207 (2005).
139. Braun, D. *J. Polym. Sci. Pol. Phys.* **41**, 2622 (2003).
140. Fina, M., Mao, S.S. *J. Appl. Phys.* **112**, 024512 (2012).
141. Zhu, L., Peng, J., Cao, Y., Roncali, J., *Chem. Soc. Rev.* **40**, 3509 (2011).
142. Duan, L., Hou, L., Lee, T.-W., Qiao, J., Zhang, D., Dong, G., Wang, J., Qiu, Y. *J. Mater. Chem.* **20**, 6392 (2010).

143. Liu, D., Fina, M., Chen, X., Liu, G., Johnson, S., Mao, S.S. *Appl. Phys. Lett.* **91**, 093514 (2007).
144. Fina, M., Liu, D., Ren, L., Mao, S.S. *Appl. Phys. A-Mater.* **105**, 323 (2011).
145. Guo, L.J. *Adv. Mater.* **19**, 495 (2007).
146. Walker, A.B., Kambili, A., Martin, S.J. *J. Phys.: Condens. Matter.* **14**, 9825 (2007).
147. Xie, Z.T., Ding, B.F., Gao, X.D., You, Z.Y., Zhang, W.H., Ding, X.M., Hou, X.Y. *J. Appl. Phys.* **105**, 106105 (2009).
148. Le, Q.T., Nüesch, Rothberg, L.J., Forsythe, E.W., Gao, Y. *Appl. Phys. Lett.* **75**, 1357 (1999).
149. Shi, S., Ma, D. *Semicond. Sci. Technol.* **20**, 1213 (2005).
150. van der Holst, J.J.M., Uijtewaal, M.A., Ramachandhran, B., Coehoorn, R., Bobbert, P.A., de Wijs, G.A., de Groot, R.A. *Phys. Rev. B.* **79**, 085203 (2009).
151. Torpey, P.A. *J. Appl. Phys.* **56**, 2284 (1984).
152. Li, Z., Meng, H. (eds.) *Organic Light-Emitting Diodes and Devices*. Taylor & Francis, Inc. (2007).
153. LeVeque, R.J. *Finite Difference Methods for Ordinary and Partial Differential Equations*. Philadelphia: SIAM. (2007).
154. Franz, A.F., Franz, G.A., Selberherr, S., Ringhofer, C., Markowich, P. *IEEE T. Electron Dev.* **30**, 1070 (1983).
155. Forrest, S.R., Bradley, D.D.C., Thompson, M.E. *Adv. Mater.* **15**, 1043 (2003).
156. Greenham, N.C., Friend, R.H., Bradley, D.D.C. *Adv. Mater.* **6**, 491 (1994).
157. "Luminosity Efficiency." Luminosity Functions. [Online] Available: <http://www.cvrl.org/lumindex.htm>
158. Vos, J.J. *Color. Res. Appl.* **3**, 125 (1978).
159. Taflove, A., Hagness, S.C. *Computational Electrodynamics*. 3rd Ed. Norwood, MA: Artech House. (2005).
160. Jin, J.-M. *The Finite Element Method in Electromagnetics*. New York: John Wiley. (2002).
161. Lee, Changhee. OLED Presentation 3 (January 2005). [Online] Available: <http://www.coema.org.cn/bbs/UploadFile/2010-6/20106131637410686.pdf>
162. Matlab® (v. 7.10.0), The MathWorks Inc., 2010.
163. FDTD Solutions® (v. 8.0), Lumerical Inc., 2012.
164. COMSOL Multiphysics® (v. 3.4), COMSOL AB, 2007.
165. Tien, C.-L., Majumdar, A., Gerner, F.A. (eds). *Microscale Energy Transport*. Washington, D.C.: Taylor and Francis. (1998).
166. Novotny, L., Hecht, B. *Principles of Nano-Optics*. New York: Cambridge University Press. (2006).
167. Yee, K. *IEEE T. Antenn. Propag.* **14**, 302.
168. "FDTD Solutions Knowledge Base Incoherent unpolarized dipole." Lumerical.com [Online] Available: http://docs.lumerical.com/en/fdtd/user_guide_fDTD_coherence_isotropic.html

169. Synowicki, R.A. *Thin Solid Films*. **313-314**, 394 (1998).
170. Dang, S. *J. Phys. D: Appl. Phys.* **41**, 125101 (2008).
171. Palik, E.D. *Handbook of Optical Constants* (3rd Ed.). San Diego: Academic Press, 1998.
172. Simmons, J.G. *Phys. Rev. Lett.* **15**, 967 (1965).
173. Wasey, J.A.E. and Barnes, W.L. *J. Mod. Optics*. **47**, 725 (2000).
174. Brüttling, W., Adachi (eds.) *Physics of Organic Semiconductors*. New 2nd Ed. New York: Wiley 2012.
175. Song, M.H., Kabra, D., Wenger, B., Friend, R.H., Snaith, H.J. *Adv. Funct. Mater.* **19**, 2130 (2009).

Appendix A. Metal-Organic Injection Equations

The Scott-Malliaras charge injection equation is the most pertinent equation mechanism for treating charge injection into an amorphous semiconductor. Therefore, this appendix will serve to better describe the derivations and ideas included in the model.

A.1. Richardson-Schottky Theory

The theory of Richardson-Schottky was historically derived for cathode emission into free space. A semi-classical result was revised by Schottky, e.g. Ref. [55], to include assumptions that a carrier jumps into a continuum of electronic states. The RS injection equations are given below:

$$J_{RS} = \frac{4\pi q m^* (kT)^2}{h^3} \exp\left(-\frac{\Phi_B - \Delta\phi}{kT}\right) \quad \text{A.1}$$

$$\Delta\phi = \sqrt{\frac{q^3 E}{\varepsilon}} \quad \text{A.2}$$

where J_{RS} is the Richardson-Schottky injection current density, m^* is the effective mass of the injected charge species, q is the fundamental charge, k is Boltzmann's Constant, T is temperature, h is Planck's Constant, Φ_B is the barrier height of the injected charge species, $\Delta\phi$ is the Schottky Barrier Lowering (due to applied field), E is the magnitude of the local electric field and ε is the material permittivity.

A.2. Simmons Theory

It was later noted by Simmons [172] that in the case that a small mean free path exists (which is common to organic semiconductors), hot electron energy is not conserved but, instead, its momentum is lost due to lattice collisions. In this case, the injection equation is governed by the drift current and is written below:

$$J(x) = qn(x)\mu E(x) \quad \text{A.3}$$

Simmons then analyzed the drift equation current at the injecting interface using the computed carrier concentration from the classical integral density of state and Fermi distribution function. The integration yielded the surface carrier concentration, n_S , which was found to be:

$$n_S = 2 \left(\frac{2\pi m k T}{h^2}\right)^{3/2} \exp\left(-\frac{\Phi_B - \Delta\phi}{kT}\right) \quad \text{A.4}$$

Substitution of Equation A.4 into A.3 yielded the relationship shown below:

$$J_S = 2q \left(\frac{2\pi m k T}{h^2}\right) \mu E_S \exp\left(-\frac{\Phi_B - \Delta\phi}{kT}\right) \quad \text{A.5}$$

where J_S is the Simmons current injection equation, E_S is the magnitude of the surface electric field and μ is the material mobility.

An important conclusion was that while the traditional RS injection form resembles the Simmons injection equation (Equation A.5), functionally the injection rates differ by a prefactor which will limit the injection into a material with a small mean free path. The injection current prefactors established by the Simmons injection equation (Equation A.5) are related to the product of mobility and electric field versus the Richardson constant. This physical difference in the mechanisms is displayed in [Figure 3.9](#).

A.3. Emtage-O'Dwyer Theory

Extending on Simmon's article, Emtage and O'Dwyer (EO) questioned the relevance of RS injection mechanism for general, low mobility semiconductors/insulators, pointing out that if the surface carrier density becomes large, increased back-diffusion to the electrode will occur. EO then performed a number of scaling analyses to justify the theory of Simmons and the regimes in which the Simmons theory was applicable. Analytical methods were used to show that space-charge limited effects can be neglected in the injection region. Also the relative importance of the diffusion-to-drift currents was analyzed by considering the injecting carrier attraction to the image potential:

$$\phi(x) = \phi_0 - qEx - \Delta\phi \quad \text{A.6}$$

Further, a criterion for assuming diffusion-limited injection effects was found to be the ratio of the RS term to the diffusion-injection equation as:

$$\mu \left[\frac{\text{cm}^2}{\text{V}\cdot\text{s}} \right] \cdot E \left[\frac{\text{V}}{\text{cm}} \right] < 5 \cdot 10^6 \quad \text{A.7}$$

which is satisfied for common organic semiconducting materials in OLED devices which have $\mu \sim 10^{-3}$ - 10^{-6} $\text{cm}^2/\text{V}\cdot\text{s}$ and $E \sim 1$ MV/cm .

A.4. Scott-Malliaras Theory

Building on the previous work by EO, which described the appropriate transport mechanism as diffusion limited, this work extends EO theory to better address interface recombination and the probability of a carrier of diffusing out of the interfacial region (see [Figure 3.9](#) for physical mechanism). Again, Scott-Malliaras (SM) work begins with the contradiction to classical RS theory; that is, RS theory was built on the assumption that carriers are injected into extended states of the semiconductor with the primary discrepancy being that in low mobility amorphous organic materials the carrier propagation takes place between localized (hopping) transport. Further, SM theory also disputes the Davids phenomenological interfacial recombination rate [114], as it lacks the ability to correctly account for the electronic structure (image potential) at the M-O interface. In this work, surface recombination is taken as a field-enhanced diffusion (Langevin) process, whereby thermal energy must be surpassed to render carriers free of image potential effects. However, in general cases, the hopping distance to surpass enter the bulk region is ~ 5 - 10 intermolecular distances. This, of course, due to the small mean free path of organic materials, means that several hopping events will occur before

a carrier can escape the interfacial region. An interfacial recombination rate is then expressed as the drift equation:

$$J_{rec} = n_{int}q\mu E(x_{int}) \quad \text{A.8}$$

and the analogous surface recombination velocity is written as:

$$S = \frac{J_{rec}}{qn_{int}} \quad \text{A.9}$$

which is a function of the surface electric field. Moreover, a detailed balance is next placed on the carrier injection at the interface, i.e. in the zero-field case no net current flows past the interface. The result is a low mobility effective Richardson constant, A^* , which has the following form:

$$A^* = 16\pi\epsilon k^2 N_0 \mu / q^2 \quad \text{A.10}$$

it is interesting to note that this equation bears no quantum mechanical terms, which appear in the semi-classical RS theory from the material DOS. In most cases, the new effective constant is several (3-4) orders of magnitude lower than the RS effective constant.

Appendix B. Semiconductor Equations - Numerical Solution

Common discretization schemes for the semiconductor equations utilize finite differences equations [117]. This appendix will serve to elucidate the numerical solution approach taken to solve the OLED system of equations. The general outline for numerical solution follows from Refs. 93 and 117.

B.1. Decoupled Quasi-linear Poisson

The Poisson equation relates electric potential variation with charge as shown below:

$$\nabla \cdot (\varepsilon \nabla \phi) = -q(p - n + N_A - N_D) \quad \text{B.1}$$

where ε is the general tensor total permittivity. For organic materials in the following discussion, the permittivity will be assumed to be isotropic and have a relative permittivity equal to 3. The total permittivity is then found as:

$$\varepsilon = 3\varepsilon_0 \quad \text{B.2}$$

where, in Equation B.1, q is the fundamental charge (1.6×10^{-19} C). It is also assumed that there are no dopants present in the organic films ($N_A = N_D = 0$). Following from the above assumptions, Equation B.1 is reduced to the following form:

$$\nabla^2 \phi = -\frac{q}{\varepsilon}(p - n) \quad \text{B.3}$$

The reworked Poisson equation in Equation B.3 is an elliptical differential equation. However, since this equation is coupled to the charge carrier densities it becomes non-linear in the presence of heavy space charge and will exhibit strong coupling with the drift-diffusion equations. Conversely, for low carrier concentrations, the equations may be decoupled and the Gummel iteration scheme may be performed [82], the potential system update for the Gummel scheme will now be discussed. Here, the first step is to describe the carrier concentrations in terms of the electric potential and their respective quasi-Fermi potentials. These relationships are shown in Equations B.4 and B.5 for electrons and holes, respectively. Note that these relationships employ Maxwell-Boltzmann statistics rather than Fermi-Dirac statistics since the carrier concentrations are non-degenerate.

$$n = N \exp\left(\frac{E_{LUMO}}{kT} + \frac{\phi - \phi_n}{V_T}\right) \quad \text{B.4}$$

$$p = N \exp\left(-\frac{E_{HOMO}}{kT} + \frac{\phi_p - \phi}{V_T}\right) \quad \text{B.5}$$

where N is the density of states (DOS) located in the respective carrier energy levels of the organic semiconductor. This is usually taken to be $\sim 10^{26} \text{ m}^{-3}$ for small molecules and $\sim 10^{27} \text{ m}^{-3}$ for polymers and independent of carrier type [114]. The values of E_{HOMO} and E_{LUMO} are

constants related to the material-specific electron affinity and ionization potential values of each material, respectively.

The solution technique begins with an initial state equivalent to an electric potential described below:

$$\phi = \frac{1}{q}(\Phi_C - \Phi_A) \frac{x}{L} \quad \text{B.6}$$

where Φ_C and Φ_A describe the work functions of the cathode and anode material respectively, x is the system position (with cathode at $x = 0$ and anode at $x = L$) and L is the total device thickness. Note the potential is Φ_C is relative to the cathode work function, Φ_C . In other words, potential is zero at the cathode.

Under the above set of circumstances according to the basic drift-diffusion equations, the individual carrier current densities are identically zero, i.e. $J_n = J_p = J = 0$. This is a result of a positionally-invariant Fermi level, i.e. $E_F = F_N = F_p = \text{const}$, where $F_{N(p)}$ are quasi-Fermi energy levels. This position of the Fermi level will further be used as a relative gauge for all other energy levels. Note as a result of the description of cathode at $x = 0$ this means that all future energy levels will be relative to the work function of the cathode.

Equation B.3 is next rewritten to include carrier concentration relationships:

$$\nabla^2 \phi = -\frac{q}{\varepsilon} \left[N \exp\left(-\frac{E_{HOMO}}{kT} + \frac{\phi_p - \phi}{V_T}\right) - N \exp\left(\frac{E_{LUMO}}{kT} + \frac{\phi - \phi_n}{kT}\right) \right] \quad \text{B.7}$$

A small perturbation expansion of ϕ is then made as shown below:

$$\phi^{k+1} = \phi^k + \delta\phi \quad \text{B.8}$$

where the superscripts k and $k + 1$ are used here to represent either time steps or iteration steps. In conjunction with Equation B.7 this expansion leads to the following relation:

$$\begin{aligned} \nabla^2(\phi + \delta\phi) = & -\frac{q}{\varepsilon} N \left[\exp\left(-\frac{E_{HOMO}}{kT} + \frac{\phi_p - (\phi + \delta\phi)}{V_T}\right) \right. \\ & \left. - \exp\left(\frac{E_{LUMO}}{kT} + \frac{(\phi + \delta\phi) - \phi_n}{V_T}\right) \right] \end{aligned} \quad \text{B.9}$$

Rewrite Equation B.9 as:

$$\begin{aligned} \nabla^2(\phi + \delta\phi) = & -\frac{q}{\varepsilon} N \left[\exp\left(-\frac{E_{HOMO}}{kT} + \frac{\phi_p - \phi}{V_T}\right) \exp\left(-\frac{\delta\phi}{V_T}\right) \right. \\ & \left. - \exp\left(\frac{E_{LUMO}}{kT} + \frac{\phi - \phi_n}{V_T}\right) \exp\left(\frac{\delta\phi}{V_T}\right) \right] \end{aligned} \quad \text{B.10}$$

Recognizing that the terms in the brackets on the right are actually just expansions on the current carrier concentrations, Equation B.10 becomes:

$$\nabla^2(\phi + \delta\phi) = -\frac{q}{\varepsilon} \left[p^k \exp\left(-\frac{\delta\phi}{V_T}\right) - n^k \exp\left(\frac{\delta\phi}{V_T}\right) \right] \quad \text{B.11}$$

After separating the Laplacian operations on left-hand side above (for the case of small $\delta\phi$), the equation becomes:

$$\nabla^2(\phi) + \nabla^2(\delta\phi) = -\frac{q}{\varepsilon} \left[p^k \exp\left(-\frac{\delta\phi}{V_T}\right) - n^k \exp\left(\frac{\delta\phi}{V_T}\right) \right] \quad \text{B.12}$$

For small $\delta\phi$ above, Taylor expansion of the terms on the right hand side are:

$$\exp\left(-\frac{\delta\phi}{V_T}\right) \approx 1 - \frac{\delta\phi}{V_T} \quad \text{B.13}$$

$$\exp\left(\frac{\delta\phi}{V_T}\right) \approx 1 + \frac{\delta\phi}{V_T} \quad \text{B.14}$$

Incorporating Equations B.13 and B.14 into Equation B.12 gives:

$$\nabla^2(\phi) + \nabla^2(\delta\phi) = -\frac{q}{\varepsilon} \left[p^k \left(1 - \frac{\delta\phi}{V_T}\right) - n^k \left(1 + \frac{\delta\phi}{V_T}\right) \right] \quad \text{B.15}$$

Next, Equation B.15 is separated so that all variables related to the independent potential update variable, $\delta\phi$, are on the left-hand side of the equation and all dependent variables are on the right-hand side, leads to the following equation:

$$\nabla^2(\delta\phi) - \frac{q}{\varepsilon} \frac{\delta\phi}{V_T} (p^k + n^k) = -\nabla^2(\phi) - \frac{q}{\varepsilon} (p^k - n^k) \quad \text{B.16}$$

Using generalized-position finite differences to approximate the Laplacians above yields the following difference equation:

$$\frac{2}{\Delta x_i + \Delta x_{i+1}} \left[\frac{\delta\phi_{i+1} - \delta\phi_i}{\Delta x_{i+1}} - \frac{\delta\phi_i - \delta\phi_{i-1}}{\Delta x_i} \right] - (\delta\phi_i) \frac{q}{\varepsilon} \frac{1}{V_T} (p^k + n^k) \quad \text{B.17}$$

$$= \frac{2}{\Delta x_i + \Delta x_{i+1}} \left[\frac{\phi_{i+1} - \phi_i}{\Delta x_{i+1}} - \frac{\phi_i - \phi_{i-1}}{\Delta x_i} \right] - \frac{q}{\varepsilon} (p^k - n^k)$$

where Equation B.17 represents an implementable equation describing a linearized update on ϕ . A summary of the system of difference equations is given below in [Table B.1](#).

Table B.1: Summary of linearized Poisson equation implementation

$$\delta\phi_{i+1}: \frac{2}{\Delta x_i + \Delta x_{i+1}} \cdot \frac{1}{\Delta x_{i+1}}$$

$$\delta\phi_i: \frac{-2}{\Delta x_i + \Delta x_{i+1}} \left[\frac{1}{\Delta x_{i+1}} + \frac{1}{\Delta x_i} \right] - \frac{q}{\varepsilon V_T} (p^k + n^k)$$

$$\delta\phi_{i+1}: \frac{2}{\Delta x_i + \Delta x_{i+1}} \cdot \frac{1}{\Delta x_{i+1}}$$

$$RHS: \frac{-2}{\Delta x_i + \Delta x_{i+1}} \left[\frac{\phi_{i+1} - \phi_i}{\Delta x_{i+1}} - \frac{\phi_i - \phi_{i-1}}{\Delta x_i} \right] - \frac{q}{\varepsilon V_T} (p^k - n^k)$$

Boundary condition handling of the Poisson equation is achieved by controlling the potential difference applied across the device. The potential ramp is applied to the anode side ([Figure 4.1](#)). A constant potential of 0V is maintained at the structured cathode side. Therefore, no update is required on the left node (or, rather, $\delta\phi_{x=0} = 0$). However, an update is required for all other positions, as follows:

$$\phi^{k+1}(x) = [\phi^{k+1}(x=L) - \phi^k(x=L)] \left(\frac{x}{L} \right) \quad \text{B.18}$$

After an update is made on all potentials, the anode potential is fixed and the anode potential equation can be restated as $\delta\phi_{x=L} = 0$. Further, this procedure does require user-defined control of the function: $\phi(x=L, t)$. The voltage ramp is used to guide the system to the correct solution. (Non-linear systems require careful considerations as non-linear solvers may find a false residual-minimizing solution.) When an applied voltage is reached where the information is to be captured, the voltage ramp is stopped and the time continues to be stepped until a spatially constant total current is reached. This condition is used to describe the convergence of the drift-diffusion system of equations.

Table B.2: Summary of linearized Poisson equation implementation

$$\delta\phi^{k+1}(x): [\phi^{k+1}(x=L) - \phi^k(x=L)] \left(\frac{x}{L}\right)$$

$$\delta\phi_{x=0} = 0$$

$$\delta\phi_{x=L} = 0$$

The equations summarized in [Table B.2](#) are a decoupled quasi-linear Poisson update step.

B.2. Continuity equations

The drift-diffusion equations are restated below:

$$J_n = q\mu_n \left(-n \frac{\partial\phi}{\partial x} + V_T \frac{\partial n}{\partial x} \right) \quad \text{B.19}$$

$$J_p = q\mu_p \left(-p \frac{\partial\phi}{\partial x} + V_T \frac{\partial p}{\partial x} \right) \quad \text{B.20}$$

where, it should be noted that the values for carrier mobility, $\mu_{n(p)}$, are found using the Pool-Frankel (PF) mobility relation, shown below:

$$\mu_{n(p)} = \mu_{n(p),0} \exp \left(\sqrt{\frac{\|E\|}{E_{n(p),0}}} \right) \quad \text{B.21}$$

where, $\mu_{n(p),0}$ is the zero-field mobility for the corresponding carrier type, $\|E\|$ is the positional magnitude of the vector electric field and $E_{n(p),0}$ is the zero-field base carrier electric field parameter [114].

The landmark paper by Scharfetter and Gummel (SG) [83] determined that the standard finite difference scheme miscalculates the current densities shown in Equations B.19 and B.20. Their method allows for stabilized current density that is more appropriately takes a linearly varying electric potential into account (whereas standard differences neglect the electric potential variation over the element [117]). As follows the SG spatial discretization scheme is shown below:

$$J_{n,i+\frac{1}{2}} = q\mu_{n,i+\frac{1}{2}}V_T \left(\frac{1}{\Delta x_i}\right) \left[B \left(\frac{\phi_{i+1} - \phi_i}{V_T}\right) \cdot n_{i+1} - B \left(\frac{\phi_i - \phi_{i+1}}{V_T}\right) \cdot n_i \right] \quad \text{B.22}$$

$$J_{p,i+\frac{1}{2}} = q\mu_{p,i+\frac{1}{2}}V_T \left(\frac{1}{\Delta x_i}\right) \left[B\left(\frac{\phi_{i+1} - \phi_i}{V_T}\right) \cdot p_{i+1} - B\left(\frac{\phi_i - \phi_{i+1}}{V_T}\right) \cdot p_i \right] \quad \text{B.23}$$

where, the function above, B , is referred to as the Bernoulli function and is described as:

$$B(x) \equiv \frac{x}{\exp(x) + 1} \quad \text{B.24}$$

and, above the assumption has been made that the Einstein relationship (shown below) is valid.

$$\frac{kT}{q} = V_T = \frac{D_{n(p)}}{\mu_{n(p)}} \quad \text{B.25}$$

which has been shown to be valid in organic materials to within reasonable accuracy provided the carrier concentrations do not exceed $\sim 10^{17-18} \text{ cm}^{-3}$. This condition is valid except in close proximity to the injection and interfacial regions.

B.2.1. Decoupled Drift-Diffusion Equations

Following the introduction of the SG discretization scheme it can be readily applied to, e.g. the electron drift-diffusion equation, shown below:

$$\frac{\partial n}{\partial t} - \frac{1}{q} \frac{\partial J_n}{\partial x} = -R \quad \text{B.26}$$

here, R is the recombination rate term associated with a Langevin-type electron-hole capture process and is shown to be:

$$R = \frac{q}{\varepsilon} \max(\mu_n, \mu_p) np \quad \text{B.27}$$

A fully-implicit, backward Euler is used since the system of equations is, in general, stiff. Higher order methods such as BDF (backward differentiation formula) may be used to improve stability and accuracy. The backward Euler time-derivative approximation is shown below:

$$\frac{\partial n}{\partial t} \approx \frac{n^{k+1} - n^k}{\Delta t} \quad \text{B.28}$$

The electron drift-diffusion equation is then written as shown below:

$$\begin{aligned}
& \frac{n^{k+1} - n^k}{\Delta t} - \frac{2}{\Delta x_i + \Delta x_{i-1}} \left\{ \mu_{n,i+\frac{1}{2}}^{k+1,p}(E) \cdot V_T \right. \\
& \quad \cdot \left(\frac{1}{\Delta x_i} \right) \left[B \left(\frac{\phi_{i+1} - \phi_i}{V_T} \right) n_{i+1}^{k+1} - B \left(\frac{\phi_i - \phi_{i+1}}{V_T} \right) n_i^{k+1} \right] - \mu_{n,i-\frac{1}{2}}^{k+1,p} \cdot V_T \\
& \quad \cdot \left(\frac{1}{\Delta x_{i-1}} \right) \left[B \left(\frac{\phi_i - \phi_{i-1}}{V_T} \right) n_i^{k+1} - B \left(\frac{\phi_{i-1} - \phi_i}{V_T} \right) n_{i-1}^{k+1} \right] \left. \right\} \\
& = -\frac{q}{\varepsilon} \max(\mu_n, \mu_p) \cdot n_i^{k+1,p} \cdot p_i^{k+1,p}
\end{aligned} \tag{B.29}$$

where Δt and Δx represent discretized time and space elements, respectively. In the above equation, it should be noted that step “ $k+1,p$ ” refers to the previous iteration step, i.e. “ $k+1$ ” refers to the iteration step that is currently being solved for and “ k ” refers to the previously solved time step. Next, a small perturbation step to the above equation is utilized by replacing n^{k+1} with $n^{k+1} + \delta n$. Equation B.29 is then recast as follows:

$$\begin{aligned}
& \frac{(n_i^{k+1,p} + \delta n_i) - n_i^k}{\Delta t} \\
& \quad - \frac{2}{\Delta x_i + \Delta x_{i-1}} \left\{ \mu_{n,i+\frac{1}{2}}^{k+1,p}(E) \cdot V_T \right. \\
& \quad \cdot \left(\frac{1}{\Delta x_i} \right) \left[B \left(\frac{\phi_{i+1} - \phi_i}{V_T} \right) (n_{i+1}^{k+1,p} + \delta n_{i+1}) - B \left(\frac{\phi_i - \phi_{i+1}}{V_T} \right) (n_i^{k+1,p} \right. \\
& \quad \left. \left. + \delta n_i) \right] - \mu_{n,i-\frac{1}{2}}^{k+1,p} \cdot V_T \right. \\
& \quad \cdot \left(\frac{1}{\Delta x_{i-1}} \right) \left[B \left(\frac{\phi_i - \phi_{i-1}}{V_T} \right) (n_i^{k+1,p} + \delta n_i) \right. \\
& \quad \left. \left. - B \left(\frac{\phi_{i-1} - \phi_i}{V_T} \right) (n_{i-1}^{k+1,p} + \delta n_{i-1}) \right] \right\} \\
& = -\frac{q}{\varepsilon} \max(\mu_n, \mu_p) \cdot n_i^{k+1,p} \cdot p_i^{k+1,p}
\end{aligned} \tag{B.30}$$

Next, all perturbation values are moved to left-hand side, and all constant terms are moved to the right-hand side yielding the implementable forms of the equations described below in [Table B.3](#).

Table B.3: Summary of electron drift-diffusion equation

$$\begin{aligned}
 \delta n_{i+1}: & \frac{-2}{\Delta x_i + \Delta x_{i-1}} \frac{1}{\Delta x_i} \mu_{n,i+\frac{1}{2}}^{k+1,p} \left(E_{i+\frac{1}{2}} \right) V_T B \left(\frac{\phi_{i+1} - \phi_i}{V_T} \right) \\
 \delta n_i: & \frac{1}{\Delta t} + \frac{2}{\Delta x_i + \Delta x_{i-1}} \left\{ \mu_{n,i+\frac{1}{2}}^{k+1,p} \left(E_{i+\frac{1}{2}} \right) V_T \left(\frac{1}{\Delta x_i} \right) \left[B \left(\frac{\phi_{i+1} - \phi_i}{V_T} \right) \delta n_{i+1} \right. \right. \\
 & \left. \left. + \mu_{n,i-\frac{1}{2}}^{k+1,p} \left(E_{i-\frac{1}{2}} \right) V_T \left(\frac{1}{\Delta x_{i-1}} \right) B \left(\frac{\phi_i - \phi_{i-1}}{V_T} \right) \right] \right\} \\
 \delta n_{i-1}: & \frac{-2}{\Delta x_i + \Delta x_{i-1}} \frac{1}{\Delta x_{i-1}} \mu_{n,i-\frac{1}{2}}^{k+1,p} \left(E_{i-\frac{1}{2}} \right) V_T B \left(\frac{\phi_i - \phi_{i-1}}{V_T} \right) \\
 RHS: & - \left(\frac{n_i^{k+1,p} - n_i^k}{\Delta t} \right) \\
 & - \frac{2}{\Delta x_i + \Delta x_{i-1}} \left\{ 2 \mu_{i+\frac{1}{2}}^{k+1,p} V_T \frac{1}{\Delta x_i} \left[B \left(\frac{\phi_{i+1} - \phi_i}{V_T} \right) n_{i+1}^{k+1,p} \right. \right. \\
 & \left. \left. - B \left(\frac{\phi_i - \phi_{i+1}}{V_T} \right) n_i^{k+1,p} \right] \right. \\
 & \left. - 2 \mu_{i-\frac{1}{2}}^{k+1,p} V_T \frac{1}{\Delta x_{i-1}} \left[B \left(\frac{\phi_i - \phi_{i-1}}{V_T} \right) n_i^{k+1,p} \right. \right. \\
 & \left. \left. - B \left(\frac{\phi_{i-1} - \phi_i}{V_T} \right) n_{i-1}^{k+1,p} \right] \right\} - \frac{q}{\varepsilon} \max(\mu_n, \mu_p) p_i^{k+1,p} n_i^{k+1,p}
 \end{aligned}$$

B.2.2. Boundary conditions on electron system

The effect of an injection controlled boundary condition on the electron drift-diffusion equation is now discussed. When the contact is injecting, anode holes and cathode electrons under forward bias, the surface carrier concentrations can be directly evaluated from Equation 3.33. The value of the carrier concentration can be found directly from the previous time step and then converged when solving the full system of equations. For the non-injecting contacts, the carrier current density assumed not to change at the corresponding electrode.

Appendix C. Experimental Setup

A considerable amount of time was spent designing and setting up efficient device fabrication and testing strategies. Beginning with producing consistent and high efficiency baseline devices, great effort was made to perform quick, easy and accurate experimentation. In particular, graphical user interfaces (GUIs) were developed in the Matlab [162] programming language to automate the material deposition, device testing and data collection. This section will give a brief overview of the specific measurement setups used and developed during the course of this work.

C.1. Mechanical System

All deposition and characterization were performed in a glove box in Lawrence Berkeley National Laboratory (LBNL) room 70-226. Figure C.1 illustrates the major components of the system. The system consists of four pumps. Three of the pumps including one roughing pump (1402N, Welch), turbomolecular pump (TPU-050, Pfeiffer-Balzars) and cryopump (Cryo-Torr8, CTI cryogenics) were aimed at conditioning a low pressure environment to carry out ballistic (or scatter-free) thermal evaporation deposition. This deposition regime facilitates directional material deposition. The pumps required manual power up. The turbomolecular pump ultimate pressure was found to be $\sim 10^{-5}$ torr. The cryopump ultimate pressure was $\sim 10^{-6}$ torr. The non-dimensional parameter which compares the length scale of evaporative flux transport to the length scale of average scattering distance is the Knudsen number, Kn , which is defined as follows:

$$Kn = \frac{\lambda}{L} \quad \text{C.1}$$

where L is the characteristic length of travel, in the case of the deposition chamber it is the length from the source boat to where the material is deposited at the top of the chamber (~ 30 cm) and λ is the scattering mean free path defined as:

$$\lambda = \frac{kT}{\sqrt{2}\pi\sigma^2p} \quad \text{C.2}$$

where σ is the deposited particle diameter and p is the deposition pressure. The result is that when the chamber pressure is below $\sim 10^{-6}$ torr ($\sim 10^{-9}$ atm), Kn approaches unity and the deposition is considered ballistic. This effect is important for achieving continuous, pinhole-free films.

The final roughing pump was used to maintain vacuum on the transfer tube line, which simultaneously is used to maintain constant pressure in the glove box by relieving overpressure and is used to pump out unwanted air/water when moving in/out materials to the glove box.

The atmosphere quality was continuously monitored using an O_2 sensor. The O_2 stat was maintained at/below 0.5 ppm O_2 throughout the duration of experimentation. On occasion, the atmosphere required regeneration. This was carried out using a mixture gas N_2/H_2 that when heated with the desiccant dissociates contained O_2 .

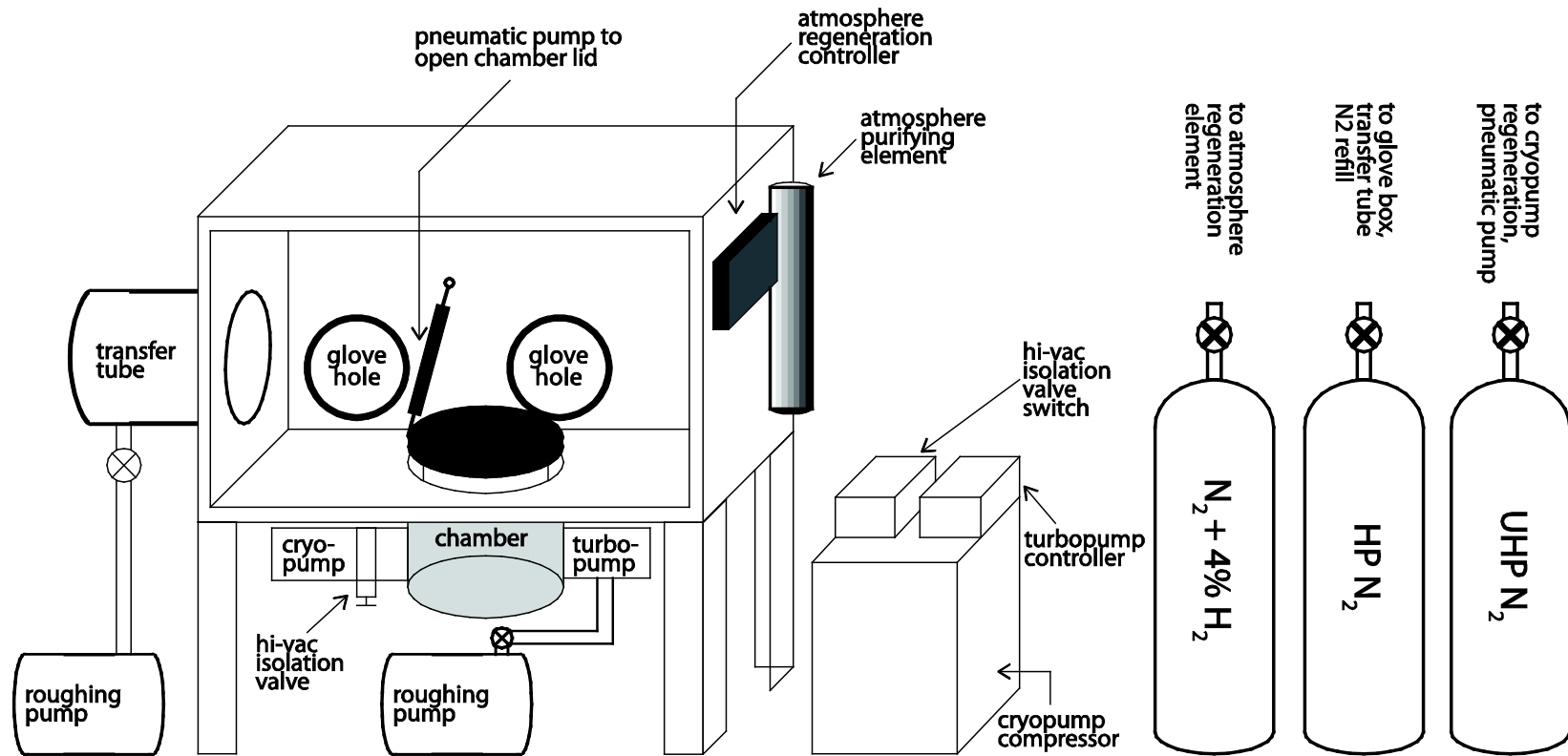


Figure C.1: Depiction of glove box deposition setup.

C.2. Device Fabrication Procedure

C.2.1. Pattern Process Layout

Throughout the course of this work, two different device layouts were used. In principle, several objectives should be considered when designing the device process layout. It was found that fabrication complications can arise with the ability to produce repeatable device areas and the ability to establish easy electrical contacts. These concerns were taken into account when designing the device layout.

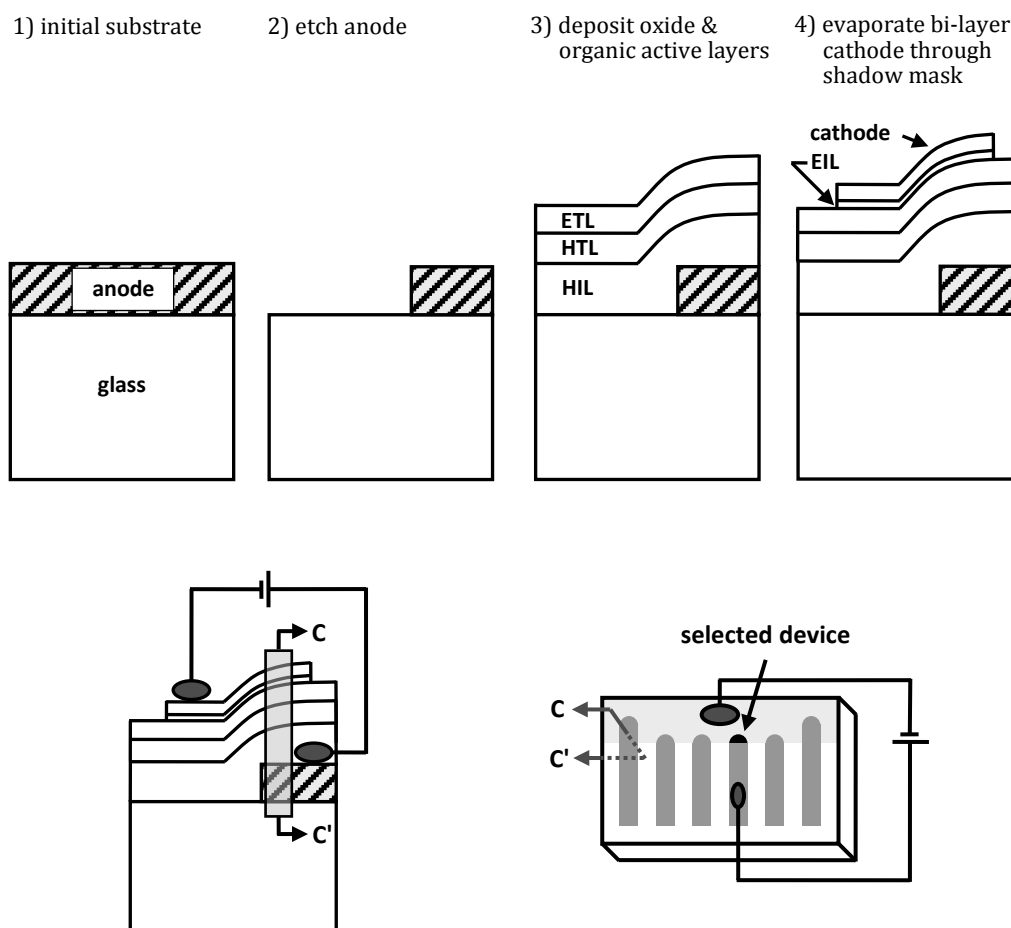


Figure C.2: Process layout #1. Top: Numbered procedure for making OLED devices. Bottom: Connection schematic for OLED.

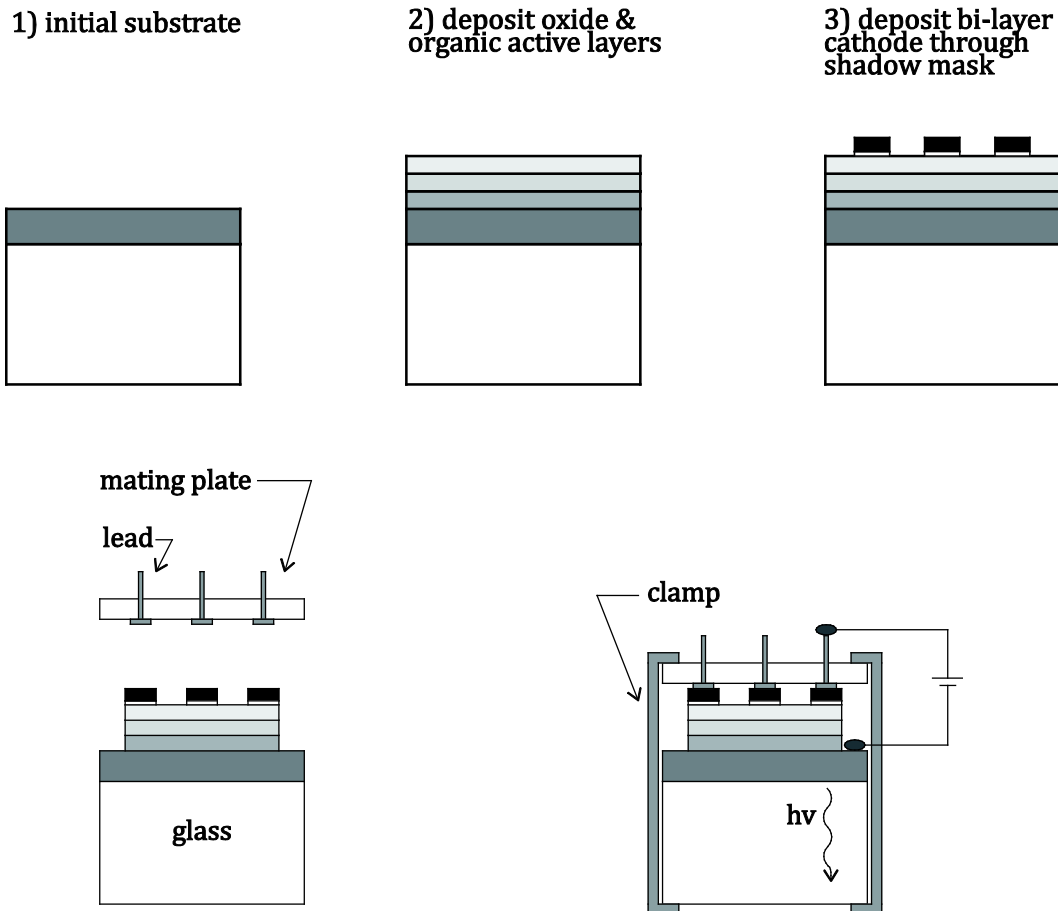


Figure C.3: Process layout #2. Top: Numbered procedure for making OLED devices. Bottom: Connection schematic for process layout.

ITO-coated-glass slides were purchased. The thickness of the ITO was found to be roughly 150nm. These substrates were the starting point for all light-emitting devices. In order to improve the sample size of the experimental devices, several devices were produced from each slide (in Figure C.2, 4 devices per slide; in Figure C.3, 9 devices per slide). It proved convenient to produce small-area devices (area less than 10mm^2). However, this requires the ability to pattern both/either the anode and/or the cathode electrode. In the case of pattern layout #1 (Figure C.2), both the anode and cathode were patterned. In the case of pattern layout #2 (Figure C.3), only the cathode was patterned.

C.2.2. Patterning ITO

For process layout #1, ITO was patterned using scotch tape to cover areas where the ITO was to remain. A small amount of zinc powder was then sprinkled on to the slides. An acidic solution of 30mL concentrated HCl and 120mL water was then poured on top of the slides in a small 8inch-by-4inch pan. After several minutes, the ITO layer would become visibly brown and was carefully removed from the acid bath and placed into a water beaker to stop the etching process. Each slide was individually removed from the beaker and a paper towel was used to scrub off residual ITO film. The scotch tape was slowly peeled off of the slide to reveal a

pattered ITO film. However, it was later found that the overlay between the cathode and anode varied by a non-negligible amount and, therefore, process layout #2 became the experiment of choice.

C.2.3. Cleaning Substrates

The development of the glass-cleaning technique in many cases varies largely from group to group within literature. Ultimately, the differences in device preparation within literature are largely based on the dangers associated with using each chemical in the cleaning process. Many groups use very caustic baths to clean (remove organic contaminants) the glass slides. In this work, moderate chemicals were used.

To begin with a roughly 30cm x 60cm sheet of ITO-coated glass is cut down using a glass scribe into 1" x 2" slides for layout #1 and 1"x1" slides for layout #2. A number of the slides typically around 20 are then cleaned while the remaining slides are temporarily stored for usage at a later time. The slides to be cleaned are stored in a caustic basic bath containing potassium hydroxide, ethanol and water. It is shown that the basic nature of the solution has the ability to break down inorganics on the surface of the slides. The slides are carefully transported into a 5 gallon bucket containing the caustic solution. The bucket contains a small slide holder held within a 500mL glass short beaker. The slides are kept in the solution for at least one night.

When the slides are ready to be used, the slides are carefully removed from the caustic solution and moved to a similar plastic holder where distilled water is added and used to remove residual solution off of the slides. The slides are then scrubbed using a cotton ball and Cleanix® cleaning solution to remove residual surface particulates. Next, the slides are ultrasonicated for 15 minutes each in the following progression of solvents: deionized water, acetone, ethanol and water. This step serves to remove any organics from the surface of the glass. Following these steps, the slides are moved using plastic tweezers from the holder and blow dried using air to remove residual water.

C.2.4. Patterning Aluminum

For both process layouts, the cathode was patterned. The cathode may be patterned in simpler fashion than ITO; however, there is a tradeoff that the cathode is more challenging to contact to without etching the ITO. That is, it was found that making good contacts with layout #1 was easier than layout #2. Cathode patterning was carried out by machining several cathode masks. In this case, it was required to use conductive paste to produce an electrical contact at the surface.

C.3. Thermal Evaporation Deposition

A number of films were deposited for the baseline devices. These materials include NPB, BCP, Alq3, FlrPic, LiF and Al (for traditional bottom-emitting devices). MoO3 was substituted as a hole-injecting layer for top-emitting devices. Due to the simplicity of the experimental setup available in LBL room 70-226 (manual power supply and quartz crystal monitor without shutter) and manual vacuum pump operation, considerable time was initially spent manually adjusting the power supply to deposit films. The time per film was typically to the tune of 40-60 minutes to get initial deposition and then another 40 minutes to complete deposition at ~0.1-0.5A/s. As a result it was decided to attempt to automate the system's operation using a control system methodology.

Thermal evaporation deposition was carried out in this work took place using a high power density, power supply (EMS 10-500, TDK-Lambda). A shutter was not used during deposition; therefore, the applied voltage on the power supply was ramped very gradually until deposition began. A quartz crystal monitor (XTM/2, Inficon) using a 6 MHz quartz crystal sensor was used to accurately monitor the progress of the deposition. A schematic of the system is shown in [Figure C.4](#) below. The materials were loaded into crucibles inside of thermal boats. Aluminum was evaporated from tungsten coil (R.D. Mathis Corp.).

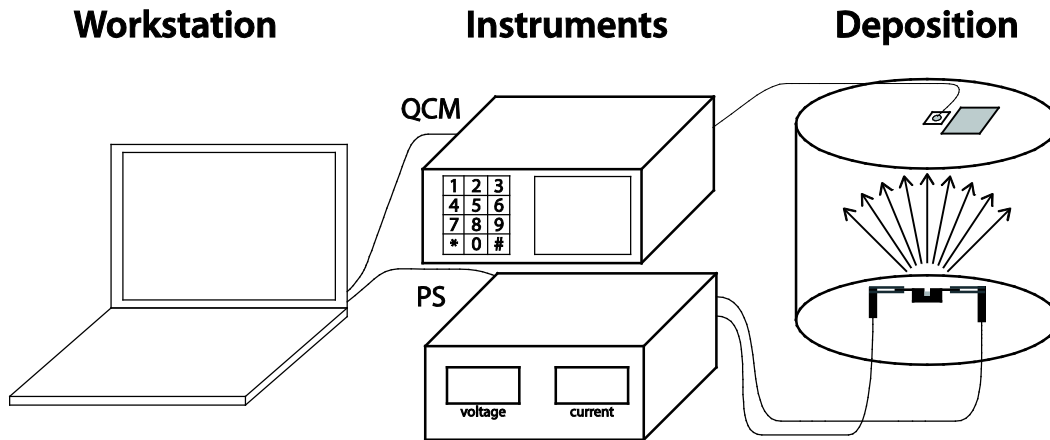


Figure C.4: Automated deposition setup. Workstation is connected via serial port to the quartz crystal monitor (QCM) and deposition power supply (PF). The instruments then control deposition power supply and record the deposition rate from the QCM.

C.4. Device Characterization

Automation of the L-J-V (luminance-current density-voltage) and spectrum was developed to facilitate device testing. The measurement instruments used in this experiment included a sourcemeter (Keithley, 2420 Sourcemeter), luminance gun (LS-110, Minolta) and CCD spectrometer (USB2000, Ocean Optics). The characterization setup is depicted below in [Figure C.5](#).

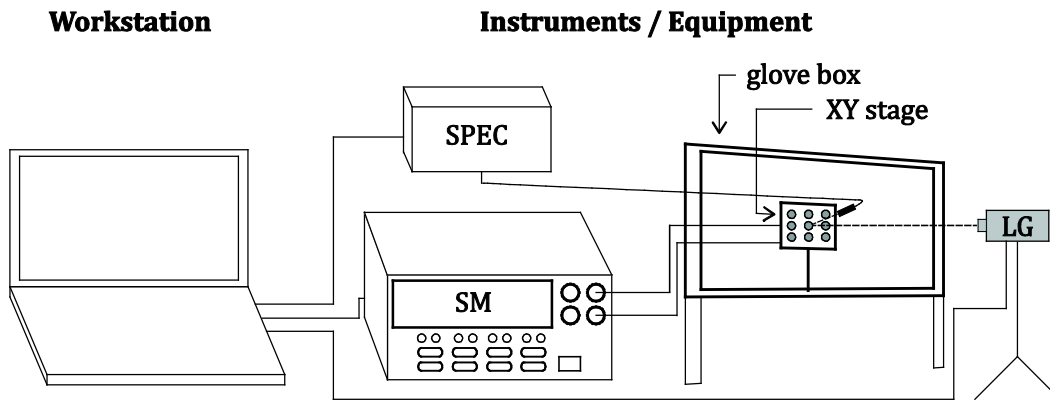


Figure C.5: Automated device characterization setup for L-J-V measurement and spectrometry of luminance. Programmatic integration of sourcemeter (SM), luminance gun (LG) and spectrometer (spec). A stage can be moved to test different devices on each slide.